

# On the Energy Dissipation of Charge Density Wave Systems and Topological Insulator Surfaces

INAUGURALDISSERTATION

ZUR

Erlangung der Würde eines Doktors der Philosophie

vorgelegt der

Philosophisch-Naturwissenschaftlichen Fakultät

der Universität Basel

VON

Dilek Yildiz

aus Türkei

Basel, 2019

Originaldokument gespeichert auf dem Dokumentserver der Universität Basel

[edoc.unibas.ch](http://edoc.unibas.ch)

Genehmigt von der Philosophisch-Naturwissenschaftlichen Fakultät  
auf Antrag von:

Prof. Dr. Ernst Meyer  
Prof. Dr. Martino Poggio

Basel, 16. Oktober 2018

Prof. Dr. Martin Spiess, Dekan

*“Experimentation is the least arrogant method of gaining knowledge. The experimenter humbly asks a question of nature.”*

Isaac Asimov

In the loving memory of my dad!

---

## Abstract

**D**ISSIPATION mechanisms in a broad spectrum of physical systems and media attracted great interest among fundamental scientific and applied communities. Understanding the origin of various energy dissipation (non-contact friction) mechanism is still a wide-open problem. The frictional nature of layered systems, such as those hosting charge density wave (CDW) and topologically protected surface state, awaits to be investigated. Regarding CDW, I investigated non-contact energy dissipation on 1T-TaS<sub>2</sub> surface. I studied the origin of dissipation on two phases of CDW and the effect of Mott insulating state on dissipated power. The low-temperature experimental results indicate that on a strongly pinned commensurate CDW phase, Joule dissipation is the main dissipation mechanism. The character of dissipation changes at room temperature and for nearly commensurate CDW phase. There the fluctuation driven dissipation is the main dissipation channel. The room temperature spectroscopy performed on the nearly commensurate phase of charge density wave indicates that the source of the fluctuating force and dissipation is the stochastic motion of weakly pinned charge density waves. Next, I studied the electronic nature of Bi<sub>2</sub>Te<sub>3</sub> surface and energy dissipation on this topologically protected surface. I observed the suppression of the common Joule type losses due to a topologically protected surface state, which prevents electron scattering into the bulk states. It was found that dissipated power is related to the presence of image potential states that are found in the gap between the tip and the sample. The study shows that the damping coefficient increases due to charge fluctuation in the system when image potential states get populated via a single or few-electron tunneling process. Furthermore, the application of magnetic fields leads to the breaking of the topologically protected surface state and the rise of the Joule dissipation. Last, I report on the observation of dissipation peaks at selected voltage-dependent tip-surface distances on the oxygen-deficient strontium titanate (SrTiO<sub>3</sub>) surface. The experiment was performed at low temperatures ( $T = 5K$ ). The observed dissipation peaks are attributed to tip-induced charge state transitions in quantum-dot-like entities formed by a 2D system of single oxygen vacancies present at the SrTiO<sub>3</sub> surface.



---

# Contents

<b>Abstract</b>	<b>v</b>
<b>Introduction</b>	<b>1</b>
<b>1 Theory</b>	<b>5</b>
1.1 Forces measured by AFM . . . . .	6
1.1.1 Electrostatic interaction . . . . .	6
1.1.2 van der Waals interaction . . . . .	7
1.1.3 Chemical interaction -Leonard Jones potential . . . . .	8
1.2 Mechanisms of Energy Dissipation . . . . .	9
1.2.1 Joule-dissipation mechanism . . . . .	9
1.2.2 Dissipation due to charge fluctuation . . . . .	11
1.2.3 van der Waals friction mechanism . . . . .	11
1.2.4 Phononic energy dissipation . . . . .	12
<b>2 Experimental techniques</b>	<b>13</b>
2.1 Pendulum Geometry AFM (p-AFM) . . . . .	14
2.2 Cantilever dynamics in non-contact friction measurements . . . . .	14
2.2.1 Minimum detectable force and dissipation . . . . .	16
2.2.2 Advanced technology geometry Cantilever (ATEC) . . . . .	17
2.2.3 Cantilever and calibration . . . . .	19
2.3 Scanning Tunneling Microscope (STM) . . . . .	20
2.4 Combined p-AFM/STM . . . . .	24
2.4.1 Probes . . . . .	25
2.5 Sample preparation . . . . .	26
<b>3 van der Waals layered materials - HOPG</b>	<b>29</b>
3.1 Structural properties . . . . .	30
3.2 pendulum AFM study on HOPG at 77K . . . . .	30
3.3 Summary . . . . .	32

## Contents

---

<b>4</b>	<b>Transition-Metal Dichalcogenide - 1T-TaS<sub>2</sub></b>	<b>33</b>
4.1	Crystal structure . . . . .	33
4.2	Charge Density Wave and Mott Phase transition . . . . .	34
4.3	Study on the electronic properties of 1T-TaS <sub>2</sub> . . . . .	36
4.4	Study on energy dissipation mechanisms on 1T-TaS <sub>2</sub> . . . . .	37
4.5	Summary . . . . .	43
<b>5</b>	<b>Topological Insulator Surface - Bi<sub>2</sub>Te<sub>3</sub></b>	<b>45</b>
5.1	Crystal structure and topologically protected surface state . . . . .	46
5.2	STM and STS study on the electronic properties of Bi <sub>2</sub> Te <sub>3</sub> . . . . .	47
5.3	STM study on the IPS on Bi <sub>2</sub> Te <sub>3</sub> with an oscillating tip . . . . .	48
5.4	pAFM study on the energy dissipation mechanisms on Bi <sub>2</sub> Te <sub>3</sub> . . . . .	51
5.5	Energy dissipation on Bi <sub>2</sub> Te <sub>3</sub> under external magnetic field . . . . .	53
5.6	Discussion . . . . .	53
5.7	Summary . . . . .	54
<b>6</b>	<b>2DEG system - Sr<sub>2</sub>TiO<sub>3</sub></b>	<b>59</b>
6.1	Strontium titanite (STO) . . . . .	59
6.2	STM Results . . . . .	60
6.3	Local and non-local dissipation . . . . .	62
6.4	Discussion . . . . .	64
	<b>Bibliography</b>	<b>71</b>
	<b>Acknowledgements</b>	<b>81</b>
	<b>List of publications &amp; communications</b>	<b>85</b>
	<b>Curriculum Vitae</b>	<b>89</b>



---

## Introduction

**F**RICTION and energy dissipation is one of the old problems humankind has encountered and played with. The friction force, in the textbooks, is defined as the force keeping an object from sliding on another object. It could simply be the reason why wheels were invented in the first place since dragging a big heavy object is not easy. The problem of friction and related dissipative phenomena is not only the concern of big objects, but it is also interesting at the small scale.

After scanning probe microscopy was introduced, it was possible to study the friction at the atomic scale [1, 2]. Today the dissipation is measured even when there is no contact between the objects [3]. Understanding the force interactions and energy exchange between macroscopic bodies have importance in many aspects of physics. It is particularly critical to understand and eventually control the carrier dynamics in materials that are used for advanced technological applications. Step by step, we learn more on different properties of materials: like electrical or thermal conductivity, robustness or reactivity of surfaces to be able to make more advanced products. As a simple example, if excellent electrical conduction is demanded, we use metals, but we might also use ceramics when we need to control the size and shape of the material with voltage. We chose the material according to our needs. In this thesis, I will approach to the scientific problem of energy dissipation in layered materials and study frictional phenomena to develop a better understanding of the possible mechanisms that drive the energy dissipation in those materials. The focus of this thesis is; what is the effect of electronic structure/nature of the layered materials on dissipated energy and what is the nature of energy dissipation? Answering this question will give us an idea not only on the dissipation mechanism but we will also learn more about the electron and phonon dynamics on the surfaces of the materials.

Dissipation spectroscopy is successful in probing different frictional phenomena over structural or electronic phase transition [4, 5]. Energy dissipation is effected by the electron and phonon dynamics in the crystals/surfaces during phase transition [6, 7]. On the other hand, the Joule power dissipation of a metallic surface is known to depend on material conductivity. Fluctuating electromagnetic fields are present in

## Introduction

---

every physical system at a finite temperature. The fluctuating field, in turn, might increase the dissipated energy of the oscillating cantilever. However, it is not an easy task to separate different coupling forces acting between the tip and the sample, as well as to precisely determine the exact dissipative mechanism that occurs in the sample. One of the reasons is that the coupling mechanisms are usually more complex than the theory anticipates. Another critical point is that often more than one coupling force is involved. Pendulum AFM is useful to determine the dominant mechanism because of its high force sensitivity and non-contact and non-invasive mode of operation.

In this thesis, I studied the energy loss over temperature-driven electronic and structural phase transitions. Consequently, the effect of electron dynamics was studied. I will also address the problem of electronic structure and its influence on Joule type of dissipation. For that reason, an important part of my work was devoted to the development of STM in combination with AFM. The van der Waals crystals are distinctive for their frictional behavior, which is, of course, easy to oversee in scaled-up measurements. At the nanoscale, different aspects of physics can be found in van der Waals layered materials depending on parameters like temperature, electric or magnetic field, and pressure. Such rich systems are of my interest in order to understand the dissipation mechanisms on layered surfaces.

In the following chapter 3, an introduction to non-contact dissipation is made. The section provides the general theoretical background of the force interactions between an oscillating tip and the sample. Forces that can be measured in our system and origins of related non-contact dissipation are also discussed. This chapter is the base of the discussions on the findings in this thesis.

Following the theoretical background introduction, experimental techniques are discussed in chapter 4. It starts with the introduction of the experimental setup called pendulum AFM. The section explains the force and dissipation measurements that are performed with a cantilever oscillating like a tiny pendulum over the surface. The cantilever probe and its force sensitivity are described here. A considerable amount of time of this study is also dedicated to the development and optimization of scanning tunneling microscopy (STM). Some STM and STS data are presented to show the improvement in the system and the importance of tip quality. An introduction to combined, simultaneous AFM/STM measurements are made.

The next four chapters are dedicated to the results obtained on studied samples, and they are analysed depending on the physical phenomena that have an impact on measured energy dissipation. Highly oriented pyrolytic graphite (HOPG) is the first sample that is mentioned in this thesis. The sample description and the experimental results are stated in chapter 5. HOPG is a van der Waals material with a relatively simple structure that is an excellent example to demonstrate the lack of Joule dissipation. Such a result is explained as due to the long electron mean free path and the lack of electron scattering. In the following chapters, we see that this is not the case for all van der Waals layered materials due to interactions complexity that is related to crystallographic and electronic structure.

After HOPG, another van der Waals material, TaS<sub>2</sub> is studied. Experimental results are discussed in chapter 6. Similarly to HOPG, the bulk crystal consists of the stacked layers coupled by van der Waals interaction. However, it is quite different from

HOPG regarding the crystal structure that has a significant effect on the electronic and frictional properties of the sample. TaS<sub>2</sub> is metal dichalcogenide, meaning that a single layer of the crystal is composed of one transition metal atom (Ta) in between two chalcogen atoms (S) that are covalently bonded. The sample possesses an interesting property called charge density wave (CDW) over a wide range of temperatures. CDW is the result of electron-phonon coupling that is very weak in HOPG. TaS<sub>2</sub> goes under structural transition and holds different charge density waves at different temperatures. At room temperature, the nearly commensurate charge density waves (NCCDW) is present that transforms into commensurate charge density waves (CCDW) for sample cooled down below 183 K. This structural change triggers metal-insulator transition upon further cooling down to even lower temperatures. At a low temperature, the system is more ordered, electron-electron coupling starts to increase, and thus, the Mott insulating phase is observed. The sample is studied at different temperatures to see the effect of different CDW phases and Mott insulating phase on dissipation. On TaS<sub>2</sub> surface, we observe the impact of electron localization onto the energy dissipation, which manifests itself as an enhancement of Joule dissipation. On the other hand, on a less ordered CDW phase, we observe van der Waals type of energy loss, due to the fluctuating electromagnetic field.

In chapter 7, the topological insulator (TI) surface of Bi<sub>2</sub>Te<sub>3</sub> is discussed. Bi<sub>2</sub>Te<sub>3</sub> is also layered material with a van der Waals interaction between the layers. However, it has completely different electronic properties than the previously mentioned samples. In this chapter, image potential states (IPS) are measured by STS, and energy dissipation in the presence of them is studied. IPS are unoccupied states that are bound with a Coulomb like potential above the sample. When the state gets occupied, dissipation in the system increases due to charge fluctuation. In the chapter, I present STM, AFM, and combined AFM/STM experimental results. The sample is a semiconductor with a small band gap, and electron scattering in this sample is suggested to be very low comparing to the ordinary metals owing to the topologically protected surface state. Thus the Joule type of dissipation is suppressed, which allows studying the dissipation originating from IPS.

The last sample that is discussed in this thesis is Sr<sub>2</sub>TiO<sub>3</sub>. It is not a layered structure but still is an interest because it may hold two-dimensional electron gas (2DEG) on its surface. Depending on density, oxygen vacancies may lead to the electronic 2DEG formation. It is found that the oxygen vacancies may act as quantum dots and can be charged-discharged when an oscillating tip tunes the chemical potential of the underlying surface. These events give rise to dissipation, and the mechanism is discussed in more detail in chapter 8.

Chapter 9 sums up the thesis by giving a general conclusion and a short outlook for future experiments.



WE intuitively know that the objects are moved from their original positions to a specific direction when they are pushed or pulled. We hardly think that this is a result of the force applied by our hands. This type of force is called contact forces and acts perpendicularly to the surface of the object. As a result, the object is moved in the direction of the applied force. On a cold day, without thinking, we rub our hands to each other to warm up. If we ask where the heats come from, the answer a physicist would give is the friction forces. Friction forces differ than the normal forces as they act parallel to the surface of the object, and a certain amount of energy is lost.

Three laws of contact friction are the following;

*1- Amontons' first law: The force of friction is directly proportional to the applied load*

*2- Amontons' second law: The force of friction is independent of the contact area*

*3- Coulomb's law of friction: Kinetic energy is independent of the sliding velocity*

Although contact friction has been studied extensively, it is still an interest of fundamental and applied research. Contact aging, superlubricity, field controlled friction are the current state of the art of contact friction. On the other hand, contact between the objects is not needed for interaction. Two separate objects can have interaction, and force can exert on these objects. These forces called as non-contact forces. Gravitational force is one of the examples of the non-contact forces. Earth gravitational force acts on our coffee cup and makes it fell on the floor.

In this chapter, we will describe the theoretical concepts in the field of non-contact friction that can be investigated experimentally using scanning probe microscopy (SPM). First, we will introduce the forces present between two macroscopic objects and within the working range of pendulum AFM and STM. These forces are relevant to the interactions of two macroscopic objects separated 0.5 - 30 nm from each other and maintain the coupling between those objects. In this work, we are interested in

macroscopic objects such as the cantilever with a sharp, conducting, and rigid tip at the end of it and the sample with a flat surface is our concern.

After that, mechanisms of energy exchange between an oscillating tip and the surface in a non-contact regime will be introduced. Although we are discussing energy transferred between objects that don't have a contact, we will see that the dissipative dynamics of the surface and also the bulk properties of the objects can be learned from dissipated energy. Using this information, we will explore the dissipation mechanisms of the surface due to the dynamics of the electronic nature of surfaces. We will begin with an example of a dissipation-less system and discuss the necessary ingredients to dissipate energy in the sample.

### 1.1 Forces measured by AFM

We can determine the acting forces between the objects that are separated by a vacuum gap [8]. The total force acting on an object is the sum of the electrostatic, van der Waals, chemical, and Pauli-repulsion force [9]. The contribution of these forces to the total force is not equal since their strength and interaction length are not the same. One has to determine the dominant force by studying the distance dependence of the frequency shift [3].

$$F_{total} = F_{el} + F_{vdW} + F_{chem} + F_{Pauli} \quad (1.1)$$

Except of Pauli-repulsion and chemical forces present at very short separation distances the mentioned forces are attractive.

#### 1.1.1 Electrostatic interaction

*Elektron* means amber in Greek, and word electric is derived from that. Around 600 B. C., they discovered that rubbing amber with a ball of wool makes amber attracts some objects. Today, we know the reason is that the amber is *electrically charged*. Objects can be positively or negatively charged. While the objects charged with the same sign repel each other, objects that are charged with opposite sign attract each other. Here electrostatic interaction that we discuss is the interaction between electrons that are at rest. Interaction range can be up to micrometer distance depending on the electron density of charged objects [10].

Two electrons can sense each other even if they are separated hundreds of nanometers since electrostatic interactions are long-ranged. When two-sphere are charged with the same polarity, the electrostatic interactions are repulsive. In the AFM configuration, however, the charged AFM tip creates an image charge of the opposite sign in the nearby surface, and thus the interaction force is always attractive. An illustrative presentation of the magnitude and long-range character of this force:

$$F_{Coulomb}(\vec{r}) = \frac{1}{4\pi\epsilon_0} \frac{Q_1 Q_2}{r^2} \quad (1.2)$$

where  $\epsilon_0$  is the permittivity of vacuum,  $Q_1$  and  $Q_2$  are the charges in unit volume and  $\vec{r}$  is the distance between them. In the case of AFM, there may be static charges present on the tip or locally on the surface. Although the forces between the tip and the sample in such cases may be high and affect the measurements, static charges can be reduced by annealing the cantilever or by coating the tip apex with a metal.

When two metal surfaces are brought closer together, and a bias applied between them, they form a capacitor. The attractive force between them can be calculated as the following  $\vec{F}_{capacitor} = \frac{\epsilon_0}{2} \frac{A \cdot U^2}{\vec{r}^2}$ , using the area of the capacitor  $A$ , the distance between them  $\vec{r}$  and the applied bias  $U$ . However, this relation is only valid for plate capacitors, and we need to take the conical shape of the tip into account. Calculating the distance dependence of the force for an AFM tip is more complicated than the plate capacitor due to the long-range electrostatic forces and the stray fields of the conical tip. For the tip-sample distances  $z$  larger than the tip radius  $R$ , an approximation can be made by considering AFM tip as a sphere attached to the cone (Hudlet). The force between a sphere and a plane for  $z \gg R$ :

$$F_{sphere}(z) = -\pi\epsilon_0 \frac{R^2}{z^2} U^2 \quad (1.3)$$

Now using the opening angle  $\Psi$  and tip height  $h$ , expression is closer to the real tip case. The total electrostatic force for AFM tip:

$$F_{el.total}(z) = -\pi\epsilon_0 U^2 \left[ \frac{R^2}{z(z+R)} + c^2 \left( \ln\left(\frac{z+R}{H}\right) - 1 + \frac{R/\sin(\phi_0)}{z+R} \right) \right] \quad (1.4)$$

where  $c^2 = \frac{1}{[\ln \tan(\Psi_0/2)]}$ . If tip sample distance  $z \ll R$ , force dependence becomes  $\pi\epsilon_0 R/z$ . At these distances force is dominated by the contribution of the tip apex.

So far we considered the materials without their work function  $\Phi$ . If the objects are made from different materials, the difference in their work function also affects the force between them. The difference is called as contact potential difference (CPD)  $U_{CPD}$ .

$$U_{CPD} = \Phi_1 - \Phi_2 \quad (1.5)$$

We reduce the equation above by combining tip dependence with the capacitance gradient. Finally, we get the electrostatic force after we introduce the  $U_{CPD}$  into the simplified equation.

$$F_{el.}(z) = -\pi\epsilon_0 \left| \frac{dC}{dz} \right| (U - U_{CPD}^2) \quad (1.6)$$

Here we should note that the minimum force between the tip and the sample is when CPD is compensated. The equation above expresses the CPD compensated case.

### 1.1.2 van der Waals interaction

Here we will consider the interaction between the dipole of neutral particles as a result of quantum mechanical or electrical fluctuations. Although expectation value

of finding a dipole of a neutral particle vanishes, an electric dipole  $d_1$  can be created due to quantum mechanical or electrical fluctuations. During the process, electric field rises and induces a polarization  $\alpha_2/\bar{r}^3$  on another neutral particle. The interaction length of the polarization is  $1/\bar{r}^3$ . Dipole  $d_2$  is created as a result of this polarization that induces a polarization on  $\alpha_1/\bar{r}^3$ . In another words, increase in fluctuation gives a rise to van der Waals interaction. We can write the interaction between two dipoles:

$$V_{vdW}(\vec{r}) = -\frac{d_1 d_2}{\bar{r}^3} = -\frac{\alpha_1 \alpha_2}{\bar{r}^6} \quad (1.7)$$

However, applying this approach for the macroscopic objects is not so realistic as we need to consider the interaction of all particles. This is not possible due to the rapid decay of polarization by a third particle. The potential is not easy to write for large objects using this approach that creates significant problems for theoretical calculations. Nevertheless, the contribution of van der Waals interaction may be substantial in some systems. At this point, we can make an empirical approach, we can write a potential for the cantilever.

Here we will use empirically described potential with a distance dependence  $V_{vdW}(\vec{r}) = 1/\bar{r}^9$  [9]. Force can be derived using the potential:

$$F(\vec{r}) = -\frac{dV(\vec{r})}{d\vec{r}} \rightarrow F_{vdW}(\vec{r}) = -\frac{HR}{2\bar{r}^2} \quad (1.8)$$

Force is specified by using H, the Hamaker constant, as a fitting parameter to describe the complex interaction with the radius of the tip R.

### 1.1.3 Chemical interaction -Lennard Jones potential

We will also mention interatomic interactions between neutral atoms and molecules using Lennard-Jones potential. It is an essential concept because it offers an understanding of how atoms make a solid.

Atoms are kept together with an attractive potential scaling with  $1/\bar{r}^6$ . The origin of this attractive potential is the van der Waals interactions that we mentioned in the previous section. Induced dipoles due to the fluctuating field of the noble gases create an attractive potential. So atoms attract each other when they are far from each other. On the other hand, if there would be an only attractive force, the atoms would collapse. Pauli repulsion, scales with  $1/\bar{r}^{12}$ , keeps their cores from collapsing when the distance between them is short.

Minimum energy configuration of infinitely many atoms is hexagonal closed packed structure in Lennard-Jones potential. It also explains the dispersion relation of gases and interactions of neutral molecules. Lennard-Jones is the potential generalized form of the interactions of atoms both at long and short separation distances.

$$V_{LJ}(\vec{r}) = -\frac{A}{\bar{r}^6} + \frac{B}{\bar{r}^{12}} \quad (1.9)$$

Here A and B are the positive constants that contains properties of the material. More general form of the equation including  $\epsilon$  and  $\sigma$  is:



$$V_{LJ}(\vec{r}) = 4\epsilon\left[\left(\frac{\sigma}{r}\right)^{12} - \left(\frac{\sigma}{r}\right)^6\right] \quad (1.10)$$

where  $\sigma = (B/a)^{1/6}$ ,  $\epsilon = A^2/4B$ . In the following, Lennard-Jones force is derived from the potential:

$$F_{LJ}(\vec{r}) = \frac{24\epsilon}{\sigma}\left[\left(\frac{2\sigma}{r}\right)^{13} - \left(\frac{\sigma}{r}\right)^7\right] \quad (1.11)$$

The Lennard-Jones interaction force and the van der Waals forces show themselves in the force-distance spectroscopy measurements in AFM. It is used to define the attractive and repulsive regime and give a good insight on the tip-sample interaction at the atomic level.

We discussed the nature of the potentials and related forces that are encountered in AFM studies. The forces that are mentioned above can be considered as conservative. This is only true for closed systems in which the energy is not lost to outside of the system, and any energy exchange is reversible within the system. However, nature is full of open systems, and energy is almost always exchanged between those systems. It is continuously transferred to another form and eventually, it dissipates.

## 1.2 Mechanisms of Energy Dissipation

Non-contact energy dissipation can be measured experimentally in the form of energy exchange between two macroscopic objects. To understand the non-contact friction; one question we could ask would be "How and under which conditions is the energy transferred from one object to another?". If we talk about the most general case, interactions between the objects that are not in contact are mediated by electromagnetic field and energy is carried between two objects accordingly [6]. However, we can study dissipation mechanisms in more detail, depending on where the transferred energy dissipates once after it is transferred to the object.

We will discuss three primary dissipation mechanisms in this thesis, namely the Joule-dissipation mechanism, fluctuation-dissipation (van der Waals friction), and phononic friction. These dissipation mechanisms may exist in bulk or on the surface of the crystal. A structural or electronic phase of the crystal, phase transitions or excitation of the states may have a strong influence on the energy dissipation mechanisms [4, 11, 5, 6]. This thesis covers the energy dissipation due to electronic and structural phase transition and the impact of electronic structure on the energy dissipation.

### 1.2.1 Joule-dissipation mechanism

We know by experience that if we pass a current through a wire with a finite resistance, the wire heats up. Ohm's law states that the dissipated power  $P$  in the unit of Watt can be expressed as  $P = R * I^2$ , where  $R$  is the resistance, and  $I$  is the current. Here electrical current causes heat dissipation - the process also known as Joule heating.

In the example of pendulum AFM, the tip is brought close to the sample surface. The charge at the end of the tip creates an image charge inside the crystal. When the

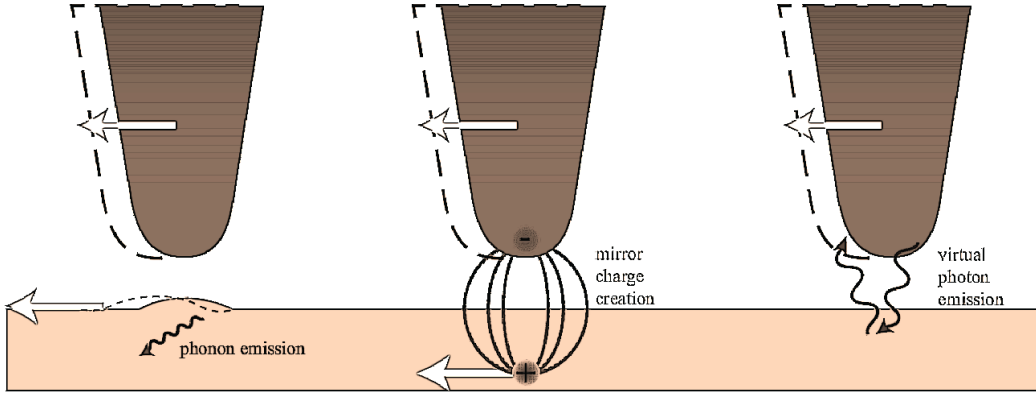


**Figure 1.1:** Schematic representation of three main non-contact dissipation mechanisms are phononic (left), Joule dissipation (middle), and van der Waals friction (right) between the moving tip and the sample are shown. Phononic friction occurs for small tip-sample distances if tip or surface are elastically deformed, and energy is lost due to phonon excitation. Joule dissipation is due to long-range Coulomb interaction, and energy loss occurs due to the creation of translational currents in the crystal via image charge. Van der Waals friction is the energy loss mechanism due to fluctuating dipoles. Energy loss is observed due to so-called virtual photons. A virtual photon from the tip is emitted due to dipole fluctuation and is absorbed by the sample. Re-emitted photon is Doppler shifted when it is absorbed by the tip, which is the reason for van der Waals friction. In other words, van der Waals dissipation occurs when the oscillating tip experiences different electromagnetic "environment" every oscillating cycle.

tip oscillates in a lateral direction to the surface, the image charge follows the same movement. However, image charge is in a different medium than the actual charge on the tip; its translational current experiences friction proportional to the resistance of the crystal. While being a coupled system, energy losses are compensated by an energy transfer from tip to the image charge. This mechanism is the non-contact version of Joule heating. Since the interaction between the tip and the surface is Coulomb interaction, the dissipation depends on tip-sample distance  $d$  and follows  $\frac{1}{d^2}$  dependence. The interaction length can be up to  $\mu\text{m}$ .

We can derive the Joule losses using an oscillating capacitor approach for the oscillating cantilever and the surface. We can replace the current in a wire with a displacement current  $D$  that varies in time due to oscillating tip. For an applied bias  $U$ ,  $D$  can be written as the following;

$$D(t) = \frac{\partial C}{\partial t} U = \frac{\partial C}{\partial z} \frac{\partial z}{\partial t} U \quad (1.12)$$

where  $C$  is the capacitance that varies due to tip oscillation and  $z$  is the distance between the tip and the sample. Due to oscillations of cantilever  $\ddot{z}(t) = A_i w_i \sin(w_i t)$ . Inserting resistance of the tip and sample  $R_{ts}$ ,  $\ddot{z}(t)$  and  $D(t)$  to the Ohm's power relation we find the Joule losses.

$$P_{Joule} = TD^2(t) = R_{ts} \frac{\partial C^2}{\partial t} U^2 A_i^2 w_i^2 \sin^2(w_i t) \quad (1.13)$$

Then the average dissipated power  $\langle P_{Joule} \rangle$  for one oscillation cycle is found as

$$\langle P_{Joule} \rangle = \int_0^{2\pi/w} P_{Joule} dt = \pi R_{ts} \frac{\partial C^2}{\partial t} U^2 A_i^2 w_i^2 \sin^2(w_i t) \quad (1.14)$$

Using the parameters for our system

$$\langle P_{Joule} \rangle \approx 10^{-24} \text{Watt/cycle} \approx 10^{-5} \text{ev/cycle} \quad (1.15)$$

### 1.2.2 Dissipation due to charge fluctuation

The fluctuating charge driven dissipation is a strongly temperature dependent phenomena because temperature excites the particles and fluctuation increases, as well as disorder in the systems. Although at a finite temperature charges always fluctuate, dissipation due to charge fluctuation is not easy to measure since dissipation mechanism is usually dominated by other mechanisms for example Joule dissipation mechanism. [12, 6]. Fluctuation of single particles (atoms, electrons, dipoles) increases depending on given energy as expected from fluctuation-dissipation theorem:

$$\Gamma(z) = \frac{1}{k_B T} \int_0^\infty \langle \vec{F}_{fl}(z, 0) \vec{F}_{z,t} \rangle dt \quad (1.16)$$

Here the thermal fluctuating force  $\vec{F}_{fl}(z, t)$  is averaged over time at a certain distance  $z$ . When the force is averaged spatially, we get:

$$F_i = \int \sigma_{ik} dS_k \quad (1.17)$$

where  $\sigma_{ik}$  is the stress tensor of the sample.

$$\sigma_{ik} = \frac{1}{4\pi} [E_i E_k + B_i B_k - \frac{1}{2} \delta_{ik} (E^2 + B^2)] \quad (1.18)$$

Here E and B are electric and magnetic fields respectively. Calculating this force in this general form has an advantage for the possibility of extending it to a more complex geometries. The theory explaining the fluctuation-dissipation approaches to the problem as stochastic event.

### 1.2.3 van der Waals friction mechanism

A distinct case of fluctuation driven dissipation is van der Waals friction occurring when fluctuating dipoles causes the attractive interaction force. Within the oscillating reference frame, the virtual photons, which are the results of dielectric fluctuations, experience momentum transfer. Thus considerable energy transfer between tip and sample occurs. The typical distance dependence of van der Waals dissipation is of  $\Gamma \propto d^{-3/2}$ .

High force and energy sensitivity are needed to measure van der Waals friction. Measuring van der Waals friction is hard to even with a sensitive cantilever since other dissipation mechanisms usually contributing to total dissipation more. However, if the correct physical system is found, it can be measured using the pendulum system as the sensitivity of it is in the order of  $\Gamma_{min} \approx 10^{-10} kg/s$ .

### 1.2.4 Phononic energy dissipation

Pendulum AFM can induce both electronic and phononic excitations while oscillating the cantilever near a substrate. Regarding the phononic mechanism, the tip oscillates in very close proximity of the surface couples to the topmost atoms owing to short-range chemical and van der Waals interactions. The in-plane motion of the cantilever tip induces a time-dependent stress field acting on the surface, which in turn produces longitudinal acoustic waves. Surface phonon excitation costs energy, which is next measured as damping of the cantilever oscillations. For a spherical tip oscillating laterally at a fixed frequency above an elastic surface, the friction coefficient depends on the force like  $\Gamma_{ph} \propto F^2(d)$ , where  $F(d)$  is the static force resulting from the interaction between the tip and the surface. According to the Lifshitz theory, the elastic stress caused by van der Waals interaction leads to a static force  $F(d) \propto d^{-2}$ , so that the phonon friction coefficient  $\Gamma_{ph}$  is expected to vary as  $d^{-4}$ .

## Experimental techniques

**I**N this chapter, I will explain the experimental setup, namely pendulum AFM, and discuss the techniques used for performing the experimental work that is covered in this thesis. We will also discuss the modifications made on the home built pendulum system to perform scanning tunneling microscopy (STM) and spectroscopy (STS) measurements.

Pendulum AFM is a home built atomic force microscopy operating in the ultra-high vacuum chamber [13]. The system can operate at room temperature (300 K), liquid nitrogen temperature (77 K) and liquid helium (5 K) temperature. An external magnetic field up to  $\pm 7$ T can be applied perpendicular to the sample surface.

Details of operating modes of the pendulum system will be given in the following sections.

Figure 2.1 shows the 3-dimensional drawing of the pendulum system and the photo of the scanning probe microscope head.

Preparing the experimental setup and characterizing the tools take more time than the actual measurement itself. Before we run the experiment, we first create an environment where the implementation of STM was a big part. The preparation includes the sample to be measured, the proper probe to measure in AFM and STM configuration that the carried measurement would be affected by the environment as small as possible. Then there is the characterization of the probe, which is one the drawback of probe microscopy and measuring in real space. If the probe is not well characterized, then the measurement itself would not be useful. For that reason, preparation and calibration of the cantilever play an essential role in the measurements. In this chapter, we discuss the cantilever preparation for specific measurements. First of all, to be able to measure such small forces, the system has to operate under ultra-high vacuum (UHV) conditions. This is crucial for two things; one is to have a clean environment such that the sample surface is not covered with adsorbate and the tip is clean as well, the second one is that the particles in the environment must be insignificant amount that the energy loss of the cantilever due to collision with the gas is negligible. Gas particles in the environment affect the quality factor of the cantilever negatively if the pressure is above  $10^{-6}$  mbar. Below that pressure, the reduction of the sensor quality

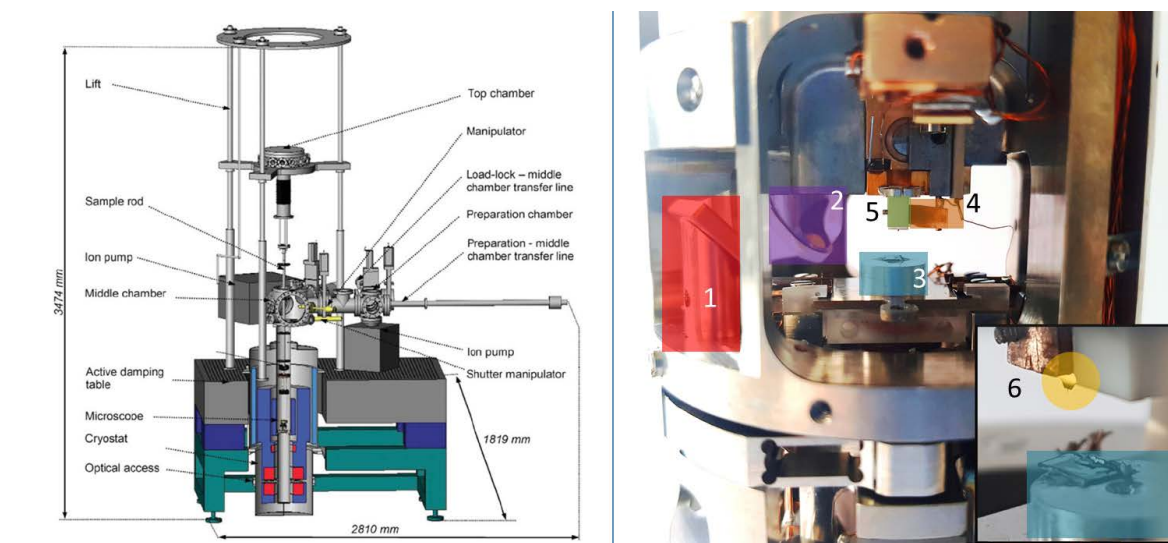


**Figure 2.1:** Schematic drawing showing the pendulum AFM ultra-high-vacuum system as well as the microscope head. The numbers stand for: 1 and 2 - set of mirrors for laser beam deflection alignment, 3 - sample, 4 - STM contact, 5 - cantilever with a cantilever holder, 6 - tip and sample at the far approach.

factor is negligible.

## 2.1 Pendulum Geometry AFM (p-AFM)

Pendulum geometry AFM takes advantage of oscillating the tip in a direction parallel to the surface, and the perpendicular force gradient does not change drastically during one oscillation cycle. The measured force is averaged over several oscillation cycles and the lateral distance covered by tip oscillation. Since conservative forces are perpendicular to the surface and force gradient can be considered as constant, the dissipative forces are proportional to the viscous drag of the cantilever. Thus dissipative forces are favoured in pendulum geometry AFM measurements. However, the poor lateral resolution is a drawback of the method due to lateral averaging.

## 2.2 Cantilever dynamics in non-contact friction measurements

Dissipation spectroscopy similarly to any spectroscopic techniques relies on perturbation of the initial state and the detection of the perturbed final state. Due to the non-invasive character of the method and small perturbation introduced by the tip, many measured phenomena can be described within linear response theory. However, the initial and final states are not the same in general:

$$E_i \neq E_f \quad (2.1)$$

## 2.2. Cantilever dynamics in non-contact friction measurements

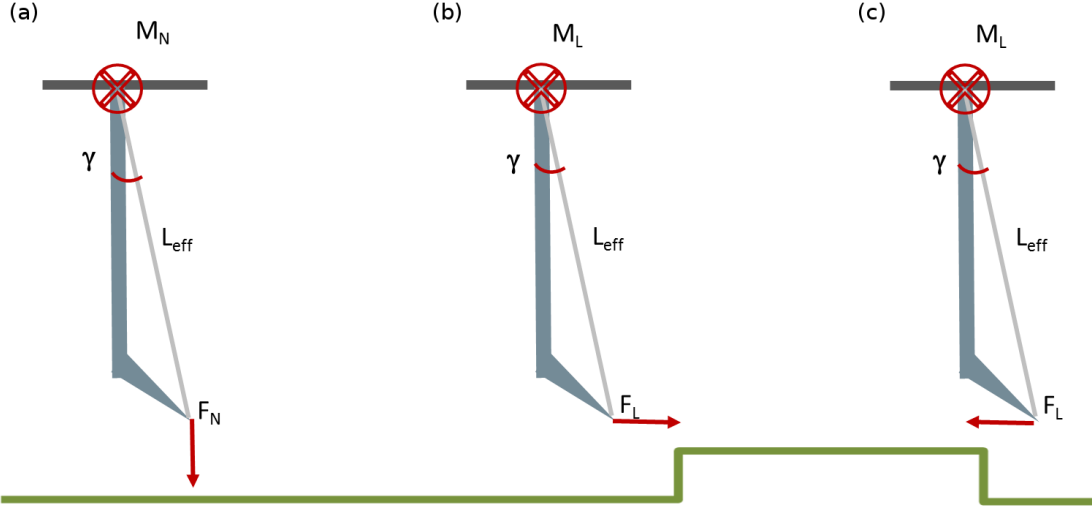


**Figure 2.2:** Forces acting on the advanced tip of the cantilever suspended in pendulum geometry. On (a) the attractive forces stiffen the cantilever causing its oscillation frequency to rise. In the presence of surface step the lateral forces soften (b)/stiffer(c) the cantilever thus making its frequency decrease/increase.

The sensing mechanism in our system of mechanical oscillator bases on dissipative force response to an interaction between the oscillator and the surface and the tip introduced perturbation. A cantilever oscillates like a tiny pendulum. Therefore, minimum detectable force and dissipated energy (power) are limited by the sensitivity of the cantilever, which is determined by its physical/mechanical properties. Also, the energy that can be stored in the oscillator decays over time. Generally, it doesn't matter how good material quality of mechanical oscillators are, they are not dissipationless. External force drives the mechanical oscillator to keep the oscillation amplitude constant. If the driving force stops, the oscillation amplitude decays in time due to internal losses. In our case, the motion of the cantilever was controlled with a Phase Lock Loop (PLL) electronics provided by Nanonis. The idea behind the PLL is to create a replica of oscillation signal that is later put back with an adjusted phase to excite the sensor in a maximum efficient way.

There are defects in the bulk of every material; these defects cause dissipation. The cantilever is made of highly doped Si when the cantilever oscillates defects in Si cause resistive switching. Resistive switching introduces stochastic fluctuation that dissipates energy. We can characterize the cantilever as a damped harmonic oscillator by using the linear simple pendulum approach.

Equation of motion for the cantilever can be written as:

$$m_{eff} \frac{d^2 x(t)}{dt^2} + \Gamma \frac{dx(t)}{dt} + m_{eff} \omega_0^2 x(t) = f_{ext}(t) + F(x(t)) \quad (2.2)$$

Here  $f_{ext}(t)$  is the driving force acting on the cantilever to compensate the energy

## Chapter 2. Experimental techniques

---

losses and keep the oscillation amplitude constant. In this equation  $m_{eff}$  effective mass,  $\Gamma$  damping coefficient,  $F(x(t))$  tip-sample interaction force, and frequency of the oscillator is  $\omega_0$ . We are interested in the damping coefficient, which using Stokes relation, defines the frictional force. Introducing the velocity of the harmonic oscillator  $v$  friction force can be written as;

$$F_{friction} = -\Gamma v \quad (2.3)$$

Here we can write the damping coefficient of  $\Gamma$  in more detail as all dissipation channels contribute to total energy loss. In the following equation,  $N$  indicates the  $N^{th}$  dissipation channel.

$$\Gamma = \sum_1^N \Gamma = \Gamma_1 + \Gamma_2 + \Gamma_3 + \dots + \Gamma_N \quad (2.4)$$

There might be many dissipation channels in one system. We will start to derive the internal losses of the cantilever because the internal loss of the cantilever is always present during the measurements. Dissipation below this value is not measurable as the signal is lost in the background of the internal dissipation signal. To determine the cantilever internal losses, I measure the time scale of the decay of the cantilever without having any interaction with the surface. The decay time of the oscillation amplitude of the cantilever after the driving force is stopped is measured, and the quality factor is derived using this information. Quality factor  $Q$ , along with spring constant  $k$ , and oscillation frequency  $\omega_0$  determine the friction coefficient of the free cantilever.

$$Q = \frac{\tau \omega_0}{2} \quad (2.5)$$

$$\Gamma_0 = \frac{k}{\omega_0 Q} \quad (2.6)$$

### 2.2.1 Minimum detectable force and dissipation

In analogy the minimum detectable force can be determined which for the extreme case of ultra-soft cantilevers ( $k \approx \mu N/m$ ) is as low as  $aN/\sqrt{Hz}$ :

$$F_{min} = \sqrt{\frac{2k_B T k_i}{\pi f_i Q_i}} \quad (2.7)$$

Similarly the dissipated power of the free sensor (index 0 refers to the free cantilever) is calculated:

$$P_0 = \frac{\pi k_i A_i^2}{e Q_i} \quad (2.8)$$

By means of measuring the distance  $d$  dependent excitation voltage we can determine the dissipated power in case of tip sample interaction, as follows:



$$P_i(d) = P_0 \left( \frac{A_{exc_i}(d)}{A_{exc_i,0}} - \frac{f_i(d)}{f_{i,0}} \right) \quad (2.9)$$

$$\Gamma_i(d) = P_i(d) \frac{e}{2\pi^2 A_i^2 f_i} - \Gamma_{i,0} \quad (2.10)$$

### 2.2.2 Advanced technology geometry Cantilever (ATEC)

In this section, we will discuss the force sensing mechanism in pendulum geometry AFM. We will introduce the asymmetric tip ATEC-NC cantilevers and find the relation between lateral and normal force components acting on the oscillating tip. Here we use the linear harmonic oscillator approximation for the pendulum system. To be able to make such an approximation, cantilever movement should be small enough so that  $\sin(\alpha) \approx 0$ . In this particular work, we considered  $\alpha \leq 3^\circ$ .

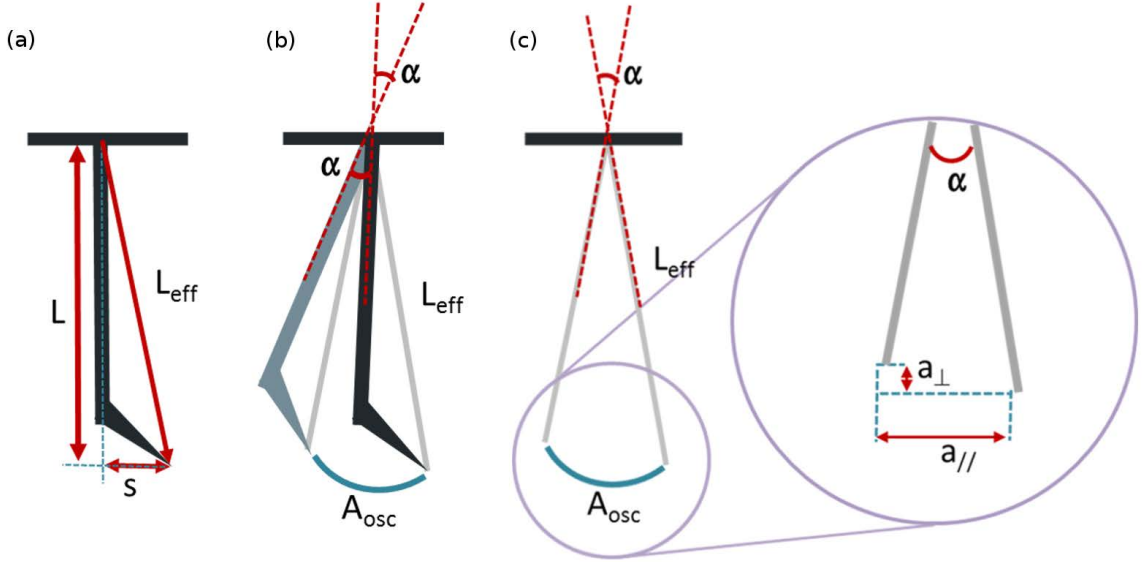


**Figure 2.3:** The advanced tip geometry causes the non-negligible perpendicular amplitude of the laterally oscillating sensor as described in the text. (a) cantilever geometry, (b) - oscillating advanced tip cantilever and (c) - a schematic drawing for calculation of perpendicular amplitude.

Equation of motion for an oscillating beam that is driven with a frequency modulated signal can be written as the following,

$$m_{eff} \ddot{z}(t) = -kz(t) + F(z(t)) \quad (2.11)$$

where  $m_{eff}$  is effective mass,  $k$  is spring constant,

$$F_N = kd_t$$

$$L_{eff} = \sqrt{L^2 + d^2} + Ld$$

## Chapter 2. Experimental techniques

---

$$F_N \cdot L_{eff} \cdot \sin(\alpha) = F_L \cdot L_{eff} \cdot \cos(\pi/2 + \alpha)$$

$$A_{osc} = L_{eff} \cdot \alpha$$

$$a_{\perp} = L_{eff}(1 - \cos(\alpha))$$

Although the frequency shift is proportional to the force, it is not easy to distinguish lateral and normal components of the force acting on the cantilever because of the asymmetric geometry of the cantilever. One can use the static bending of the cantilever to determine the normal forces act on the tip. Lateral movement of the cantilever is measured from the PSD and movement perpendicular to surface can be calculated using the above equation. We will use frequency shift for determining the distance and bias dependence of the forces present between the tip and the sample. To discuss the normal forces, let's consider the static bending of the cantilever. When  $\alpha = 0$  the system can be considered as pendulum when  $\alpha = 90$  it operated as in the normal geometry. For the large deflection angles at the close approach, the normal forces might be higher due to induced perturbation and the system might become not stable because of the of operation out of the linear regime. The phenomenologically found value are: for the soft (long) cantilever

$$\alpha = 1.87^{\circ}$$

and for the stiff (short) cantilever

$$\alpha = 3^{\circ}$$

. The relation between normal and lateral components of the force can be calculated as the following:

$$F_N = F_L \cdot 0.0524 \tag{2.12}$$

If cantilever with the same spring constant is used, smaller forces (both conservative and dissipative) comparing to conventional AFM can be measured with pendulum AFM because of the asymmetry of the cantilever (tip).

Cantilever is oscillated using an excitation signal at a central frequency, and the optical detection method is used for detecting beam deflection. An infrared laser is used for that purpose; infrared laser was focused on the cantilever and reflected light is measured on the photosensitive diode (PSD) using low noise current-voltage converter (IV-converter). PSD has four cells, which allow us to distinguish between the vertical and horizontal deflection of the cantilever. Vertical deflection is a measure of static forces acting between the tip and the sample. Static force can be calculated by using the spring constant of the cantilever and displacement of the cantilever due to static bending in perpendicular direction.

$$F_N = k d_z \tag{2.13}$$

## 2.2. Cantilever dynamics in non-contact friction measurements

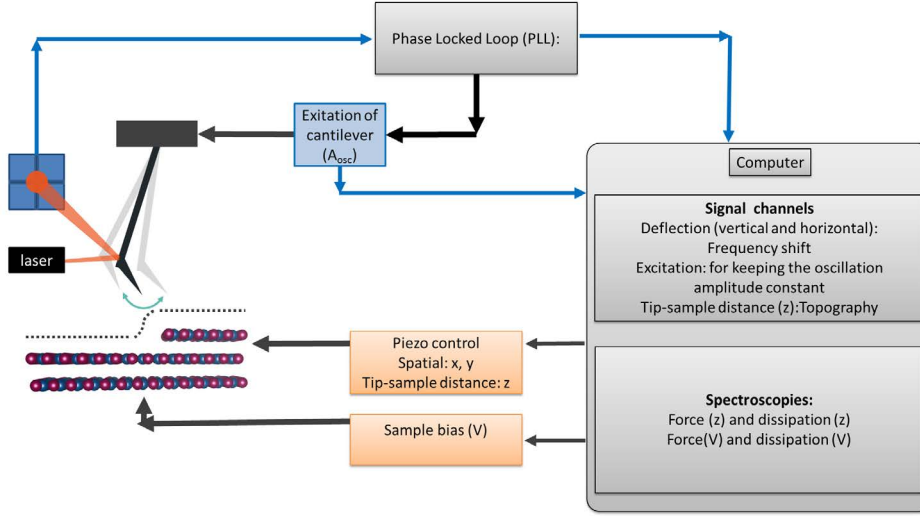


**Figure 2.4:** A schematics of AFM experiment. The bending of the cantilever and the oscillation amplitude are measured with an optical detection mechanism. Excitation signal is adjusted with the help of PLL in order to keep the oscillation amplitude constant.

### 2.2.3 Cantilever and calibration

Ability to use very soft (sensitive) cantilevers without snapping into the contact with the sample is the strength of pendulum AFM. However, traditional cantilevers known from conventional AFM can not be used in this system due to the tip geometry. We are using the optical detection to measure the beam deflection, and the real amplitude of the oscillating cantilever may change depending on the mechanical properties of the cantilever, and measured amplitude depends on the exact position of the laser spot on the cantilever bar [14–16]. For calibrating the amplitude, we are using an amplitude dependence of phase noise of an oscillating beam.

If an external sinusoidal signal does not drive the cantilever, there are still thermally induced random forces exciting the cantilever. The amplitude of the cantilever due to thermally induced forces is setting a limit for the minimum oscillation amplitude and lateral resolution that can be measured. Thermal noise can be reduced by cooling the cantilever to lower temperatures. We are limited to the liquid helium temperature in the pendulum system. When the cantilever is driven with a sinusoidal signal, a fluctuating signal still present on the periodically driven harmonic oscillator. Phase noise of the cantilever has information on the internal friction of the cantilever. For the semiconducting sensor, it is the resistive switching that causes the internal friction of the oscillating beam. So, the phase noise, which is measured by PLL depends on the oscillation amplitude of the harmonic oscillator. If the spring constant, the shape of the cantilever and the temperature is known, one can calibrate the oscillation amplitude by using the following relation.

$$x(t) = x_0 \sin(w_0 t) + A(t) \sin[w_0 t + \phi] \quad (2.14)$$

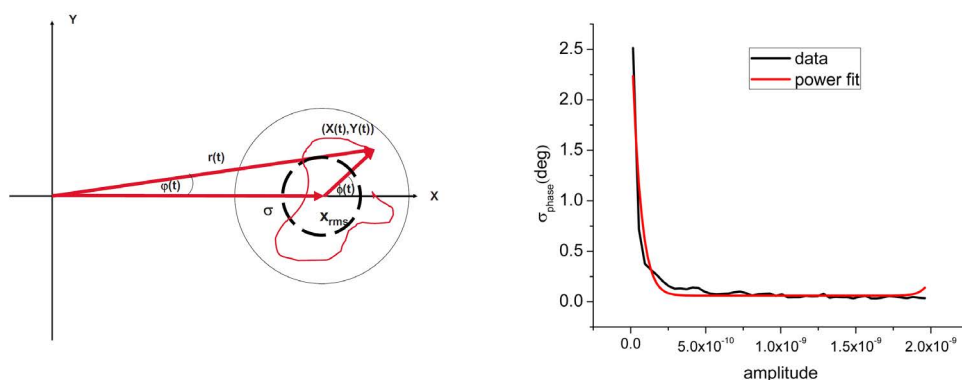


**Figure 2.5:** A phase noise measurement depending on amplitude. For large oscillation amplitudes (moving toward larger values of  $x$ -axis) the random walk of the phase as measured by the lockin decreases. Image on the right shows the measurement curve with a power fit. [15]

$$\sigma_{\varphi} = \frac{a\sigma}{x_{rms}}, \quad a = 42.131 \quad (2.15)$$

As the oscillation amplitude decreases its phase noise  $\sigma_{\varphi}$  should increase proportionately following the proportionality constant  $a$ . Therefore, by measuring the phase noise for different driving amplitudes, we can calibrate the amplitude of the sensor.

Force and dissipation both depend on the distance and applied bias. Both have rich information for determining the interaction force and dissipation mechanisms. However, defining the tip-sample distance is not accessible only by AFM. Although AFM attractive and repulsive regimes can be determined very precisely, the real tip-sample distance may not be measured with high precision depending on the material quality of the tip or sample. For instance, uncompensated charges in the tip cause static bending of the cantilever, and high forces are measured even at greater distances preventing the tip-sample close approach. A more precise technique for defining the tip-sample distance (or the sample surface) is scanning tunneling microscopy (STM).

STM feedback operates based on quantum tunneling phenomena, and tip-sample distance is typically smaller than 1nm. Tip sample distance can be considered around 0.5 nm when tunneling junction is stable with a metallic tip.

### 2.3 Scanning Tunneling Microscope (STM)

Scanning tunneling microscopy is the grandfather of force microscopy and still being developed to study the electronic properties of surfaces in real space (STM). STM is a technique based on the quantum tunneling phenomenon. Electrons are not allowed to be in a potential barrier, but Schrodinger equation has a solution for electrons on both sides of the barrier if the potential barrier is thin enough (figure 2.6). This implies that

## 2.3. Scanning Tunneling Microscope (STM)

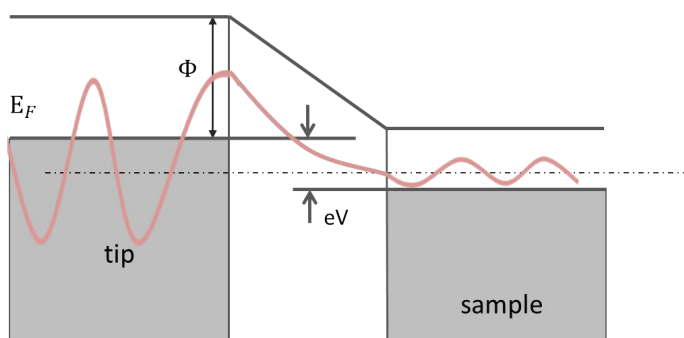


**Figure 2.6:** Schematic drawing to describe the tunneling barrier and quantum tunneling mechanisms in STM. While it is forbidden for an electron exist in the gap it can tunnel through the barrier if it has enough energy.

electrons can tunnel through the barrier. STM has the advantage of using current as feedback, can operate at typically smaller distances than non-contact AFM. In typical STM studies, metallic wires with atomically sharp end are used to achieve atomic resolution. The material of the tip is important, and materials like tungsten, gold, PtIr which are metallic and have continuous density of states are chosen for LDOS (or DOS) measurements. By choosing these kinds of materials, one can be sure to measure the DOS of the surface, not the tip. Our interest is towards the use of cantilever for combined STM/STS studies.

Scanning tunneling microscope (STM), is a member of a scanning probe microscope family that is used to investigate conductive and semiconducting samples with an atomic resolution. It is based on the quantum tunneling phenomenon, which explains electron passing through a barrier. In the case of STM, electrons tunnel between an atomically sharp tip and a conductive/semiconducting sample. Bias is applied between the tip and the sample to measure a net tunneling current [17, 18]

Representative image of quantum tunneling from sample to tip is shown above.  $\phi$  is the work function of the sample. Region 2 represents the potential barrier (and in the case of the STM, it is the gap between the tip and the sample). To make a microscope using the tunneling phenomena tip mentioned above is scanned over the sample surface while the tunneling current kept constant between the tip and the sample. Hence, this mode is called the constant current mode. While tunneling current is used as a feedback parameter, tip-sample distance should be less than 1nm. During the scan, the STM tip follows the morphological and electronic structure of the surface simultaneously. Another operation mode of STM is the constant height mode where the tip-sample distance is kept constant. In this mode, the tunneling current changes due to the electronic and morphological structure of the surface and the measured tunneling current is used to generate a topographic map of the surface. STM tip can be moved with a sub-angstrom resolution by using piezoelectric materials. The resolution is in the picometers in the z-direction. Since currents that are measured in STM studies are in the pico ampere range, I/V (current to voltage) converter with  $10^8$  to  $10^{10}$  gain is used. By using an I/V converter, the tunneling current is converted into voltage depending on the gain factor of the I/V converter. The preferred position

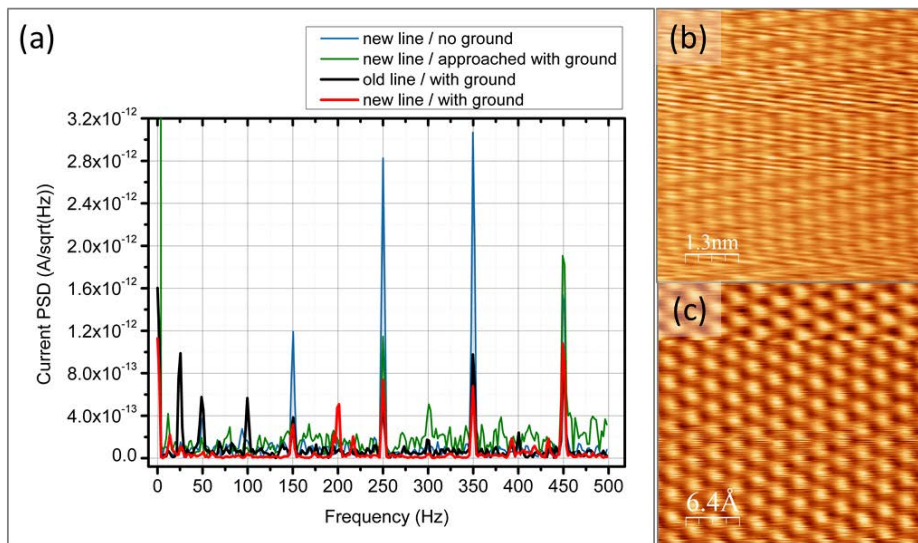


**Figure 2.7:** (a) Power spectrum density (PSD) of the current signal depending on the frequency for comparing noise levels. While noise is the highest when there is no ground, 50 Hz noise is significantly reduced with the new current line. STM data on HOPG surface with atomic resolution before (b) and after (c) changing the cables.

of the I/V converter is almost immediate after the tip-sample junction.

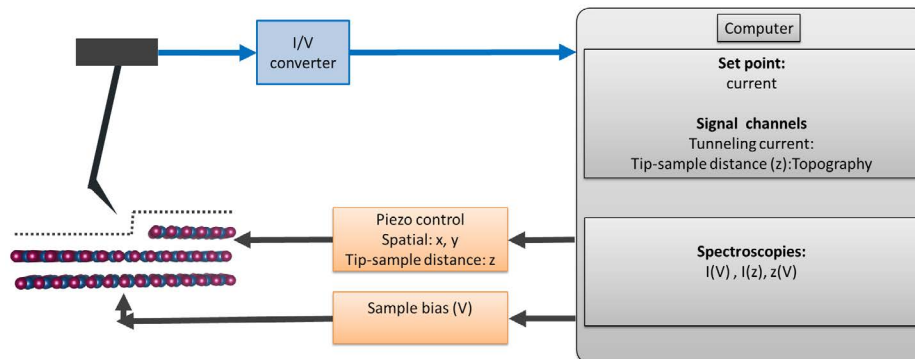


**Figure 2.8:** A scheme is showing STM at operation. The bias voltage is applied to the sample while the tip is grounded. The sample has approached the tip until tunneling current is measured. The tunneling current is measured via I/V converter and used as a feedback to control the tip-sample distance.

STM cables in the system were changed to shielded coax cables to achieve a better signal to noise ratio. The tunneling current is used as a feedback signal for performing STM and STS. Typical tunneling current at maximum in the range of low nA, a signal is difficult to transfer over long distances because it can be disturbed by external signals. Initially the STM was tip biased, and tunneling current was read from the tip as well, and later on, for convenience, the operation has been changed to sample biased configuration while the tunneling current was read out from the tip. Carrying

### 2.3. Scanning Tunneling Microscope (STM)

tunneling current and bias through separate wires reduces the noise substantially in the current signal. Tunneling current signal has to be carried for 2m before it is converted to a voltage by an amplifier which makes it more vulnerable to all types of noises around. After introducing new cables for current and bias, signal to noise ratio was tested by using mechanically cut PtIr STM tips. The tests were done for the open circuit of tunneling current (without surface) and closed circuit of tunneling current (with sample).

STM was tested with Pt/Ir tip. I found that the best I/V converter is Variable Gain Low Noise Current Amplifier DLPCA-200 from Femto. I tested the electronic noise and found the best grounding configuration for reducing the noise. I tested cantilevers and found that bests are Pt or gold-coated ATEC-NC for combined STM/AFM experiments.

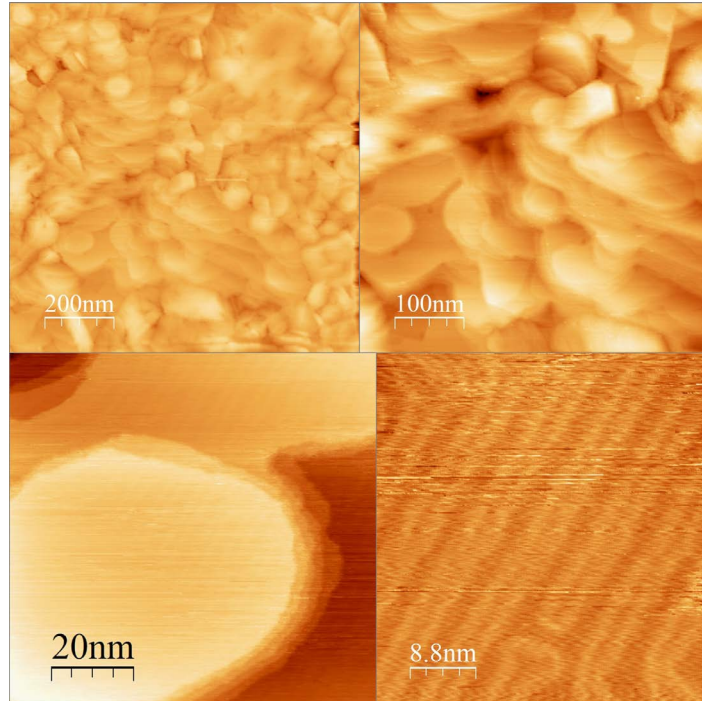


**Figure 2.9:** STM data on poly-crystalline Au surface with Au(111) facets taken by using platinum coated cantilever ATEC-NCPt. STM data show different scan ranges. Herringbone structure is shown in the image on bottom-right. Tunneling parameters,  $I_t=500$  pA,  $V_b=1.2$ V.

Poly-crystalline Au surface with Au(111) facet was used as a test sample for STM. We preferred it because Au is a metal and its surface is soft. The surface is easy to scan in STM mode and it is not likely to damage Au (or Pt) coated Si tip on such surface. Herringbone structure on Au (111) was successfully measured in STM mode using ATEC-Pt cantilever.

Nc-AFM operated at least couple of nm away from STM operation distances. The tip-sample distance is mediated by a measured force and it is possible to scan the surface for a long period of time without manipulating or damaging the surface. Tapping

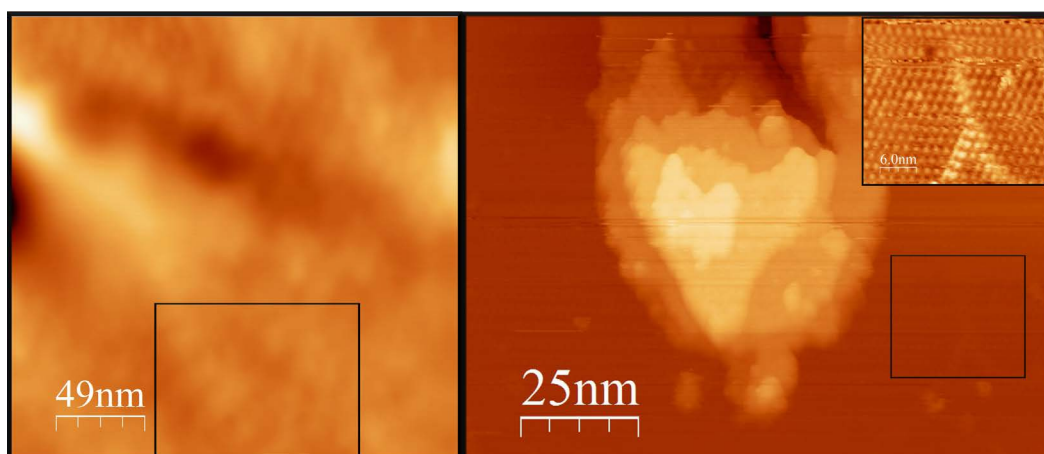


**Figure 2.10:**  $TaS_2$  surface scanned by using tapping mode (left) and STM mode (right). Oscillation amplitude of free cantilever 500pm, 400pm on the surface. Tapping mode image shows less features on the same area. STM image shows more details. Inset image is the zoom in that is marked in STM data. Tunneling parameters,  $I_t=64$  pA,  $V_b=1$  V.

mode is also useful in pendulum geometry AFM in order to scan the surface at close tip-sample distances in AFM mode. However, force signal is gathered as an averaged signal over many oscillation cycle. In pendulum AFM, the cantilever is oscillated in lateral and reduces the lateral resolution depending on oscillation amplitude. Considering the size of typical atomic lattices are in hundreds of pm ranges and typical oscillation amplitude for a stiff cantilever is minimum 300pm, it is not very likely to achieve the atomic resolution. We can solve this problem by operating the system in STM mode. STM data shows atomic structure details because the feedback signal is the tunneling current and the tip does not oscillate in the lateral direction. Moreover, the tip scans the surface at smaller tip-sample distances and gives higher spatial resolution as compared to AFM mode of operation.

## 2.4 Combined p-AFM/STM

We succeeded to perform spectroscopy measurements with the pendulum system using an STM feedback with an oscillating tip with a relatively stiff cantilever ( $k \geq 40$ N/m) with metal (Au) coating. While tip-sample distance is regulated by tunneling current, we achieved stable tunnel junction with small lateral oscillation of the tip. Operating AFM feedback with such small amplitude is not possible because the change in force is not high enough to be used as a feedback signal. However, once a stable feedback mechanism can be achieved using tunneling current as a feedback signal, a change in the excitation signal is within the measurement range. We typically used oscillation amplitude  $A_{osc} \leq 70$  pm to avoid disturbance in the feedback line. Larger oscillations introduce high translational currents that cause instability in the feedback. The combined AFM/STM operation was important to define the tip-sample distance since



STM operates typically at much closer distances as compared to AFM. The typical range of operation is at  $\leq 1$ nm tip-sample distance.

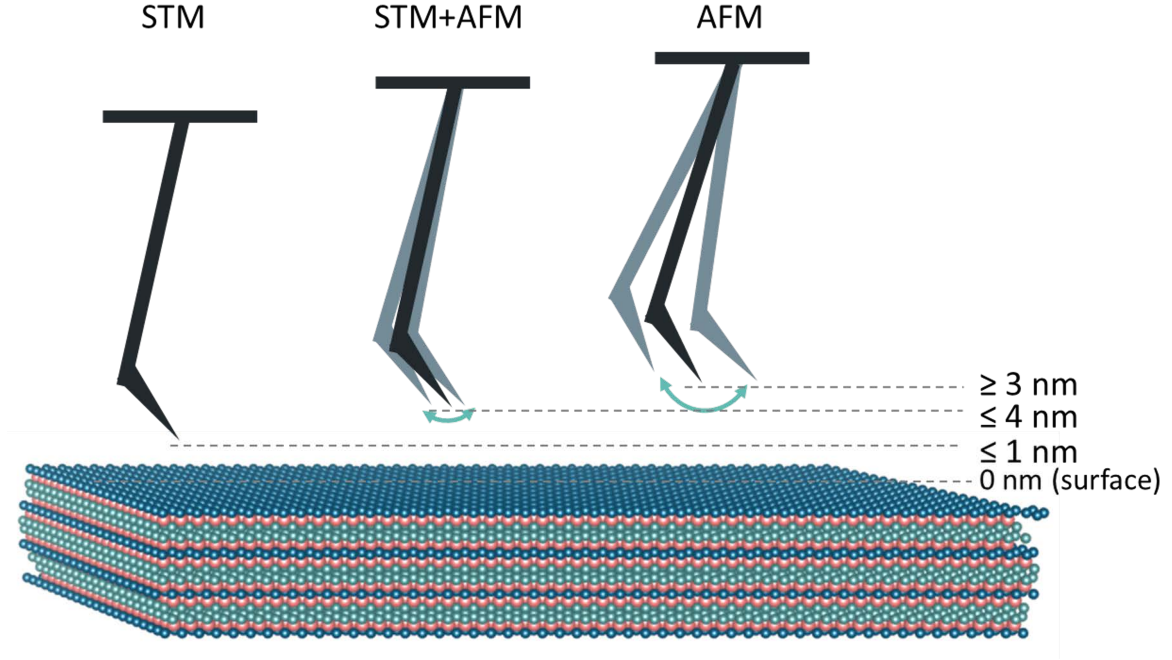


**Figure 2.11:** Schematic drawing showing the working distances in STM, AFM and simultaneous STM/AFM measurement modes. STM has the shortest working distance, tip-sample distance can be determined better in this mode.

### 2.4.1 Probes

Pt90/Ir10 alloys are rigid and can be prepared by mechanical cutting. Tips made of PtIr wires are good to perform stable STM measurements, but one cannot measure forces with them, as they are rigid wires and static forces cannot be measured due to lack of bending. In most of the measurements we used gold-coated Advanced Technology Cantilever for non-contact measurements (ATEC-NCAu cantilever) with a nominal spring constant  $k \approx 50$  N/m except the measurements on Au(111), HOPG and room temperature measurements on 1T-TaS<sub>2</sub>.

ATEC-NCAu is a multipurpose cantilever with a metallic tip and high-quality factor (measured up to 25000). If mounted sufficiently good, up to  $10^{-15}$  N/ $\sqrt{Hz}$  force sensitivity can be achieved. Metallic tip enables to perform STM, STS, and AFM measurements consequently without a need to change the probe. Moreover, simultaneous AFM/STM measurements can be done. Regular/ordinary STM tips that are metallic and rigid wires were not used in combined STM/pAFM studies. The experiments were carried out with the flexible STM tip. We gain information about the forces by monitoring the static bending of these flexible probes. The scanning tip was metallic (gold coated) and free from uncompensated charges in order to perform proper STS measurements and to avoid static bending of the cantilever caused by

electrostatic interaction. The same is valid to our AFM measurements, although AFM nominal working distance is further away from the surface as compared to STM.

Static forces were measured using the vertical deflection signal. Data shows that if the tip is not metallic, forces are in the nN range while it is in the pN range if the tip is metallic. The amount of the uncompensated charges at the end of the semiconducting tip might be the reason of huge forces that are measured with a non-metallic tip. Since the tip has a significant role in understating the measured phenomena in SPM, testing and calibrating the tip the correct way are also very important. Force measurements shows the importance of the tip material and quality to perform simultaneous STM/AFM measurements. It also explains why sometimes tip-sample distance is not defined very well using only force-distance curves. If the soft cantilever has a semiconducting tip, the forces would be measurable while the tip still far away. Since the cantilver is soft, the sample wouldn't be harmed but the cantilever would bend. While the tip is brought closer to the sample surface, the bending may be too much to operate the oscillated cantilever in the linear regime. As a result it wouldn't be possible to operate the pendulum AFM in close proximity of the surface. If the tip is metallic (free from uncompansated charges), it is possible to operate the system in STM mode and one can determine the tip-sample distance based on the operation distance of STM and than measure the forces at those distance. This would help to determine the boundaries of the measurement.

In simultaneous measurements, we used STM feedback and measured z-V by applying  $A = 30pm$  lateral oscillation to the tip. At the very close distance of STM operation, much smaller amplitudes compared to regular AFM measurements have to be applied. So, the modulation currents due to the oscillation of the cantilever are negligible, and do not contribute to the STM feedback. In this mode, tunneling current were gathered together with dissipation signals simultaneously as well as force information.

## 2.5 Sample preparation

Pure crystals are used in this study. For the layered samples, we cleaved the topmost layers using sticky tape and immediately introduced the crystal into the load lock. Some samples were heated to check the effect of air exposure to the samples, but we didn't see a strong influence of cleaving them in air. We also annealed some of the HOPG and  $Bi_2Te_3$  samples up to  $110\text{ C}^\circ$  and didn't see much of an effect in our regular STS and dissipation measurements.  $SrTiO_3$  sample was prepared in the preparation chamber by flashing-annealing cycles (Details are given in the chapter ).

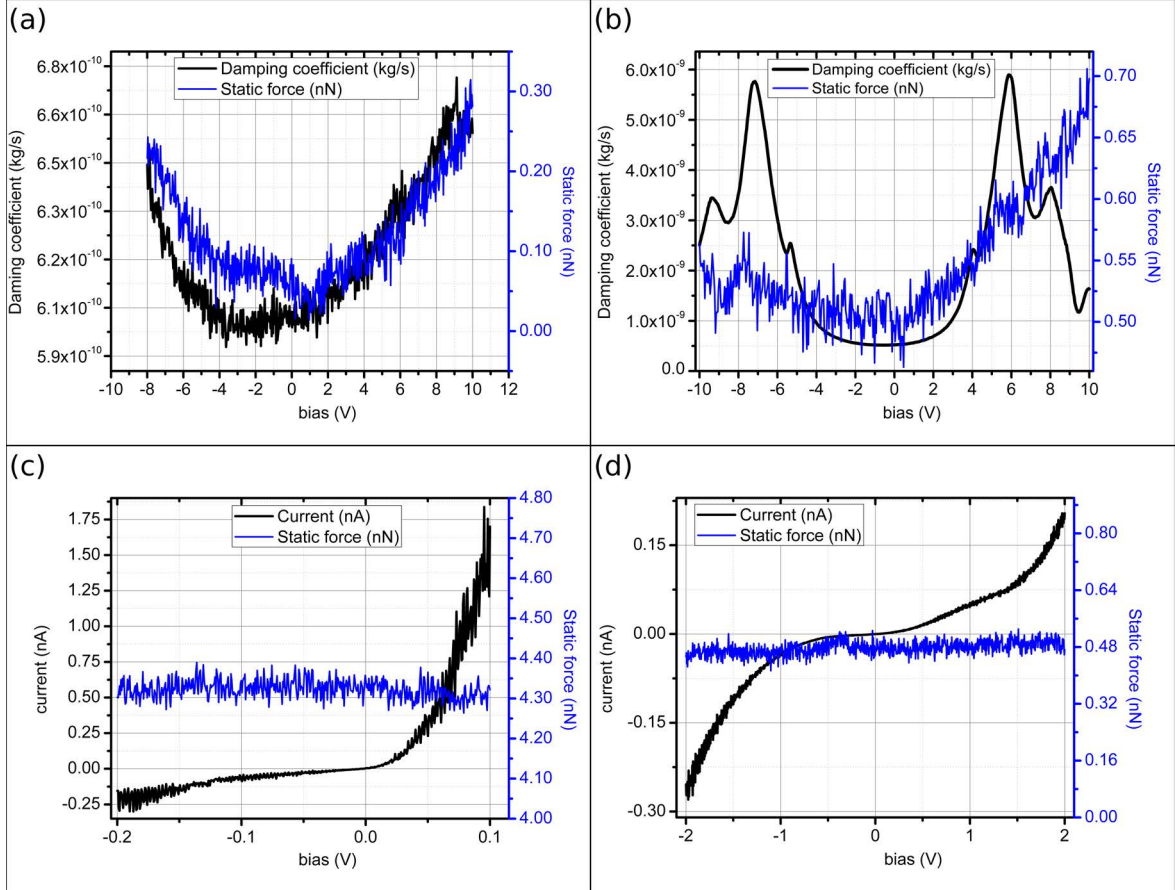


**Figure 2.12:** Spectroscopies showing the difference of a good (metallic) and bad (uncompensated charges). Data taken in (a), (c) with a bad and (b), (d) with a good tip. (a) and (b) showing the vertical deflection during the bias spectroscopy measured simultaneously with dissipation signal on  $\text{Bi}_2\text{Te}_3$  surface. tip sample distance is 40 nm in (a) and 5 nm in (b). Amount of static force measured is in the same range for the two spectra but the amount is huge for 40 nm distance. Tip-sample distances in (c) and (d) are less than 1 nm as both  $I(V)$  spectra are measured in STS mode. While  $I(V)$  curves are not similar, (d) is the expected curve on  $\text{Bi}_2\text{Te}_3$  surface. Following this, static force shown in (c) is an order of magnitude larger than in (d).



## van der Waals layered materials - HOPG

**G**RAPHITE is known as one of the best solid lubricants for industrial applications because of the lack of friction between its layers. Graphite crystal is composed of AB stacked graphene layers. As a two dimensional zero bandgap semiconductor, graphene attracted scientists a decade ago. Scientists who succeeded to isolate graphene were awarded Nobel prize, and it is still a popular material today in nanoscience and technology [19]. Being one atom thick, electron-phonon coupling in graphene is not so strong and leads to a long mean free path of electrons as long as there are no defects or edges. Long mean free path means that Joule type of dissipation is expected to be negligible or lack in graphene. Although electrons in graphene are highly mobile, the dissipationless conduction is only valid for a perfect crystal. Any defect in graphene may act as a scattering center for the energetic electrons and causes an energy loss. Single-atom defects, grain boundaries, or edges can be considered as defects. A recent study shows that defects at the edges of the graphene device act as scattering centers and dissipates via heat. Dissipation is very low on the not defected area [11, 20].

One of the main challenges for making graphene devices is the substrates used for support graphene. Substrates have a strong influence on the electronic and structural properties of graphene that makes it not easy to prepare a perfect graphene device. Metal substrates dope the graphene and semiconductor substrates make charge puddles.

Graphite is a known crystal, but it also holds interesting physics; superlubricity, van hove singularities were reported on graphene/graphite systems. Highly oriented pyrolytic graphite (HOPG) has fewer defects comparing to graphene due to the production process. However, the topmost layers can be rotated due to the weak interaction between them. Super periodic structures called as moire patterns form on the rotated layer on graphite. Moire patterns were reported to have different conductivity than HOPG [21]. Recently, Mott insulating behavior and the superconducting transition was reported for special rotation angles on twisted bilayer graphene.

### 3.1 Structural properties

Carbon atoms in the graphene layer are strongly bonded in a hexagonal lattice, and there is only weak van der Waals interaction between the layers so that the layers can be cleaved easily. Different than other derivatives of van der Waals layered materials, graphene doesn't have covalent bonds, only carbon-carbon (C-C) bonds in the layer and empty  $p_z$  orbitals. On the left image in Figure 3.1, AB stacked graphene layers, HOPG, is shown. STM image showing the triangular atomic resolution on HOPG using a Pt/Ir STM tip at 77K. AFM image on the right is showing the large area scan at 77 K on HOPG.

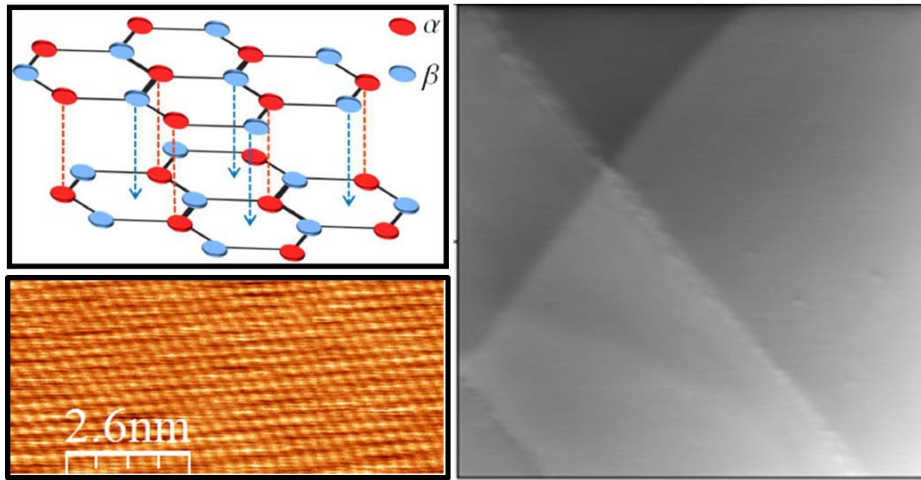


**Figure 3.1:** *The schematics of HOPG structure and STM image showing the atomic resolution on HOPG (left). Large scale AFM topography image shows a clean HOPG surface with some steps and terraces on the right.*

### 3.2 pendulum AFM study on HOPG at 77K

Force-distance spectroscopy was performed on a clean terrace on the HOPG surface (shown in Figure 3.1) by pendulum AFM with ATEC-CONT cantilever (force constant: 0.2 N/m). Force- distance curves are shown in Figure 3.2 show the lack of the long-range electrostatic dissipation on HOPG. In Figure 3.2 distance dependence of the frequency shift changes with an applied bias voltage, and it starts to shift visibly when the tip-sample distance is around 14 nm. However, dissipation curves with 0 (black) and 5 V (red) applied bias only show rise when the tip-sample distance is less than 1 nm.

Dissipation map showing the distance and bias dependence of the force and the dissipation is similar to force-distance curves. Although the force map indicates the existence of electrostatic force, it does not influence the dissipation. Simultaneously measured dissipation doesn't show any dependence on the applied voltage and the

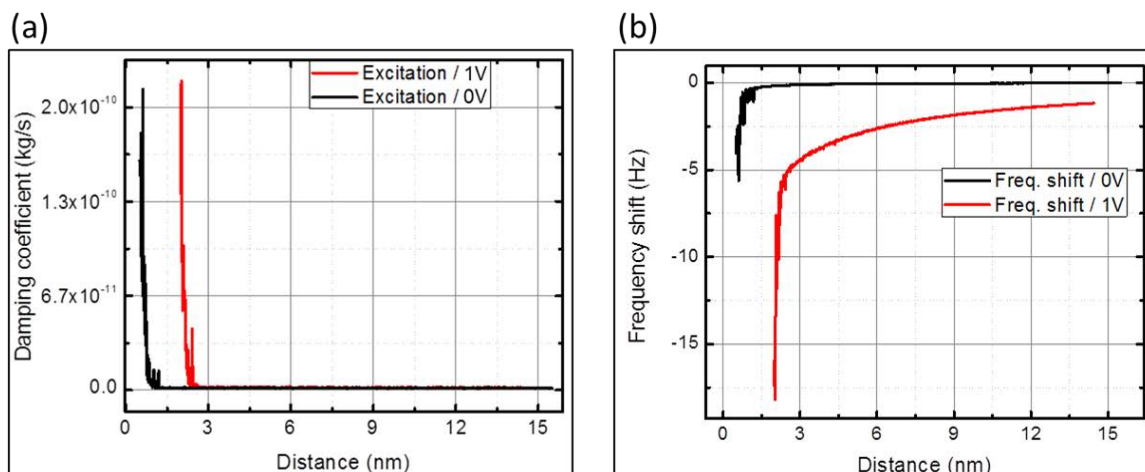


**Figure 3.2:** Force distance curves for 0 V and 1 V applied bias voltage. While force-distance curve changes with an applied bias voltage, dissipation behavior stays the same.

distance. Only when the tip-sample distance is less than 1 nm, then dissipation rises, which can be regarded as a phononic type of dissipation at this interaction range.

While electrostatic interaction can be measured between an oscillating tip and HOPG surface as it is visible in a force signal, dissipation due to this interaction is below  $10^{-11}$  kg/s. The spectroscopy is performed far from other scattering centers like step edges or defects.

Although electrostatic dissipation was not observed on HOPG, it is expected to see a rise in the Joule dissipation or van der Waals friction close to the edges of the terraces or on several moiré/HOPG systems. The lack of long-range Joule type of dissipation is natural when we take into account the long mean free path of electrons in graphitic surfaces due to the weak electron-phonon coupling and thus lack of electron scattering.

The experiments on HOPG were done when STM and the tips for STM were not optimized. Suggested experiments with an optimized setup would be to study the electronic structure of HOPG and repeat the force measurements close to the step edges or on moiré structures where electron localization or stronger interlayer coupling presents. Combining the STM study with dissipation spectroscopy would open up a possibility to investigate unconventional superconductivity on moire systems. Electron-phonon interaction is crucial for conventional superconductivity, but moire patterns show unconventional superconductivity upon Mott insulating state for some rotation angles that is a result of Coulomb interaction rather than electron-phonon coupling. One can study the effect of electron-phonon coupling via moire patterns with different rotation angles as Coulomb interaction can be tuned by the change of the rotation angle of the graphene layers [11]. —

I have also performed  $z(V)$  spectroscopy and could measure image potential states with a metallic cantilever in STM mode [22]. However, I couldn't perform  $z(V)$  spec-

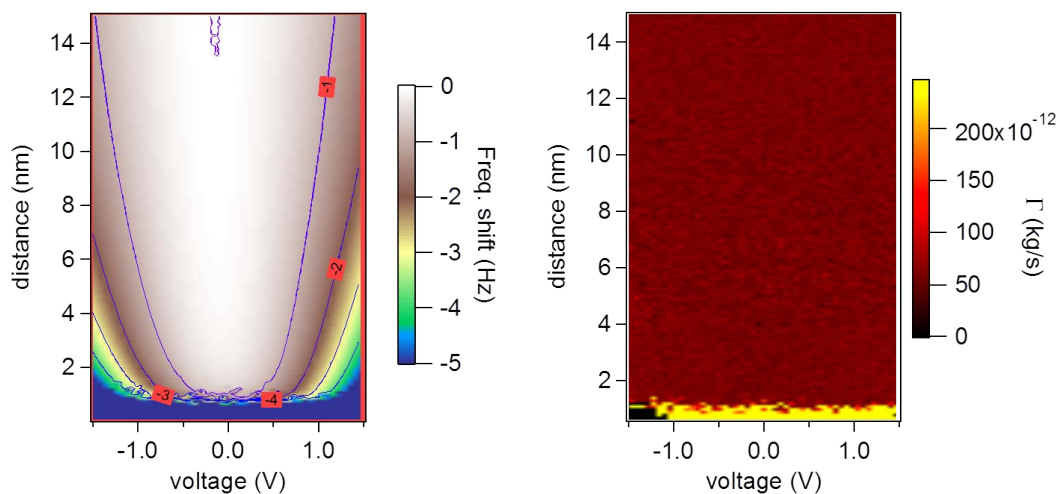


**Figure 3.3:** HOPG force-maps. On the left force map is shown and on the right is the energy dissipation. Both are represented as follows: on x-axis mutual tip-sample voltage is shown, while the y-axis stands for tip-sample distance.

troscopy with an oscillating tip. The layers possible were moved with an applied force by an oscillating tip as a result of the weak interaction between the layers that shows the effect of superlubricity on HOPG.

### 3.3 Summary

Here results on HOPG give a straightforward explanation to the lack of electrostatic friction. For that reason, it is considered as the reference sample for other layered materials in this study. In the next two chapters, we will see that other layered materials are not as straightforward. We will discuss the determining factors for energy dissipation and its strong dependence on the structural and electronic properties.



## Transition-Metal Dichalcogenide - 1T-TaS<sub>2</sub>

**T**RANSITION Metal Dichalcogenides (TMDC) are of great interest to scientist because they hold a platform to explore conventional and unconventional electronics simply by thinning the layered crystals. They are studied for a long time for their phase transitions and understanding the nature of charge density waves. However, as most of the crystal system, they are rediscovered for their topological behaviors and unusual superconductivity is driven by phase transition. 1T-TaS<sub>2</sub> is a peculiar one as it has a rich phase diagram for CDW and also goes under Mott transition at low temperatures. It is our interest to understand the frictional nature of 1T-TaS<sub>2</sub> due to electronic and structural phase transition driven by temperature change.

### 4.1 Crystal structure

Van der Waals layered materials are similar to graphite with a weak van der Waals interaction between the layers except individual layers are not single atom thick. Layers can be cleaved with sticky tape and top of the surface would be terminated with S atoms.

In a layer, Ta atom is surrounded with three-coordinate sulfide atoms that are covalently bonded to Ta. TaS<sub>2</sub> is found in the different structural phases leading to considerable differences in their electronic and structural formation. The most known polytopes are 1T-TaS<sub>2</sub> and 2H-TaS<sub>2</sub>. Single-layer 2H-TaS<sub>2</sub> has a triangular lattice where Ta atom is at the center, and S atoms are positioned in a triangular lattice as its upper and lower neighbors. This type of stacking is called ABA-stacking, and inversion symmetry is broken in such structure. However, in 1T-TaS<sub>2</sub> Ta atoms are surrounded by S atoms forming a quasi/nearly octahedron, preserving an inversion symmetry with ABC-stacking. Crystal structure and unit cell of 1T-TaS<sub>2</sub> are shown in Figure 4.1. The lattice constant of the crystal in the normal direction (*c*-axis) is 585 pm and 338 pm in the layer. While 2H-TaS<sub>2</sub> is superconducting at low temperature, 1T-TaS<sub>2</sub> becomes an insulator. Although phase transitions in both systems are quite

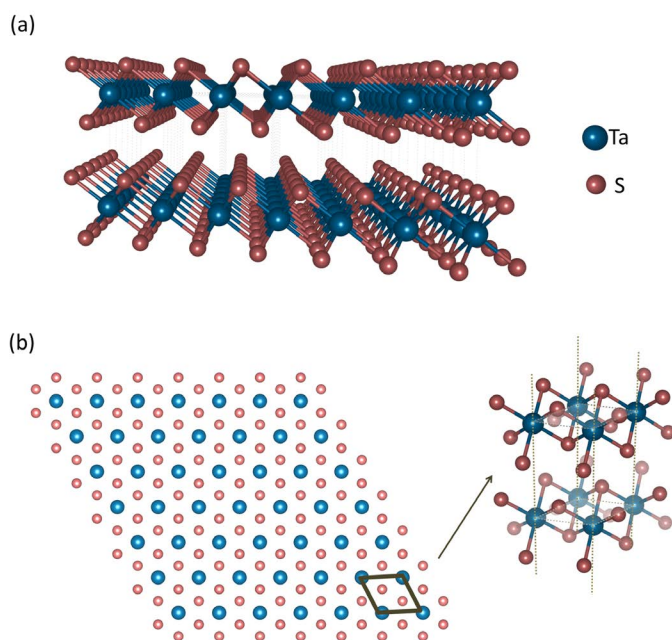


**Figure 4.1:** *1T-TaS<sub>2</sub> crystal has van der Waals interaction between the layers (see text for details).*

intriguing, in the scope of this thesis, we will focus on 1T-TaS<sub>2</sub>.

## 4.2 Charge Density Wave and Mott Phase transition

Disorder in physical systems increases with temperature. When the systems are cooled down, weak interactions in the system become more important. Peierls suggested that a one-dimensional metallic electronic system coupled to the crystal lattice (electron-phonon coupling) cannot be stable at low temperatures due to electron-phonon interaction. Periodic lattice distortions give rise to a collective mode known as charge density waves (CDW). Dispersion relation of charge density of the new phase differs from the metal [23–26]. Position-dependent modified charge density of the system can be expressed with the following relation with a wave vector of electron-hole pairs  $q = 2k_F$  and electron density  $\rho_0$ .

$$\rho(x) = \rho_0 + \rho_1 \cos(2k_F x + \phi) \quad (4.1)$$

Different phases of 1T-TaS<sub>2</sub> are accessible upon heating or cooling the sample. Above 543 K the system is in a phase so-called normal phase (N) as metal and may transform into 2H-TaS<sub>2</sub>. When it is cooled down, several phases appear; incommensurate (I) phase between 543 K and 351 K, nearly commensurate (N) between 351 K and 183 K and finally it transforms to commensurate phase with  $C\sqrt{13} \times \sqrt{13} - R13.9^\circ$  super-periodic structure. When it is heated up from the C phase, the 1T triclinic incommensurate (I) phase appears between 223 K and 283 K in addition to other phases existing on cooling. In the CCDW phase, 13 Ta atoms form David star where they

## 4.2. Charge Density Wave and Mott Phase transition

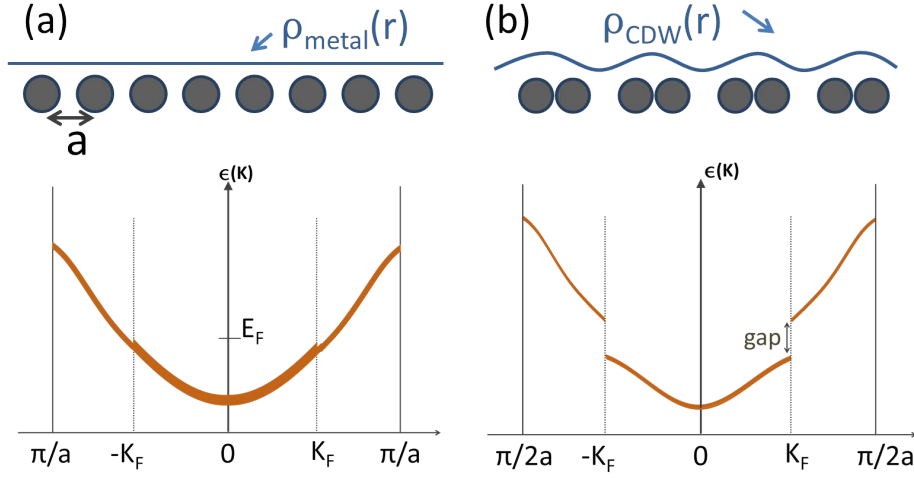


**Figure 4.2:** A model showing distortion in 1D atomic chain, CDW formation and band gap opening. a) 1D atomic chain is in order and stable in absence of electron phonon coupling, showing an ordinary metal structure. (b) When the lattice is distorted, CDW are formed and band gap opens.

have a triangular symmetry. One Ta atom is at the center of the star, and 12 Ta atoms slightly come closer to the central atom.

1T-TaSe<sub>2</sub>, structurally similar crystal to 1T-TaS<sub>2</sub>, goes under incommensurate to nearly commensurate phase transition at 523 K on cooling with a jump in resistivity but the metallic state is still preserved, and resistivity goes down following the decrease in temperature immediately after the jump [28]. The resistivity of 1T-TaS<sub>2</sub> also shows a jump following the transition from I to NC phase, however, it makes a second jump at 183 K while cooling due to the transition to commensurate phase [29, 30]. Periodicity of CCDW matches with the lattice of the crystal so that the CDW is supposed to be pinned stronger than in higher temperatures. Since high temperature induces disorder making the collective excitation more possible at higher temperatures, CDW has weaker pinning at high temperatures. At incommensurate phases, conduction can occur due to sliding of the CDW or through boundaries.

It can be seen in figure 4.3 that resistivity is three orders of magnitude higher incommensurate phase than in nearly commensurate phase. There is more to understand about the drastic change in resistivity in 1T-TaS<sub>2</sub>. As 1T-TaSe<sub>2</sub> stays as a metal at low temperatures and 1T-TaS<sub>2</sub> becomes insulator; the behavior of 1T-TaS<sub>2</sub> cannot be explained only by the structural phase transition in the crystal. CDW transitions are due to electron-phonon coupling that introduce CCDW with  $\sqrt{13} \times \sqrt{13}$  structure. Metals with half-filled d orbital may exhibit metal-insulator transition at low temperatures due to strong electron correlation, which is explained by Mott. Hence, it is called a Mott transition. Mott transition in 1T-TaS<sub>2</sub>-2 has been proposed by Tosatti and Fazekas [29] as an explanation of the drastic change in resistivity. However, the CDW formation is due to electron-phonon coupling, and superlattice formation creates a necessary environment for electron-electron coupling resulting in the Mott transition.

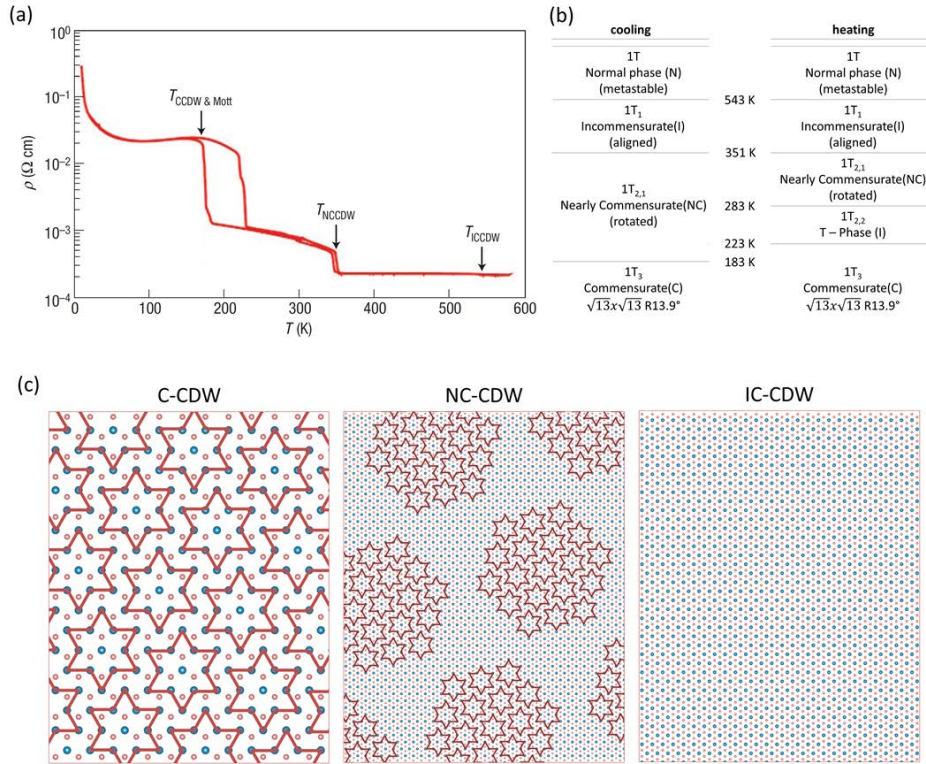


**Figure 4.3:** (a) Change in  $\rho_{\perp}$  for 1T-TaS<sub>2</sub> depending on temperature. Sharp changes in resistance happen at phase transition temperatures, and hysteresis around 200 K presents between heating and cooling. [27] 1T-TaS<sub>2</sub> crystal. (b) Temperatures where phase transitions occur and different CDW phases. (c) Models are showing three types of CDW phases that are measured on 1T-TaS<sub>2</sub>. In the CCDW phase, so-called David star is formed by 13 Ta atoms.

CCDW state exists without needing the presence of Mott state, rather the presence of CCDW generates the conditions for Mott transition to happen. Thus, 1T-TaS<sub>2</sub> goes under structural, Peierls transition and electronic, Mott transition simultaneously, and both of them trigger metal-insulator transition. The Mott gap is reported to be around 400 meV; the CDW gap is almost two times larger than that and equal 700 meV [31, 32].

In the next two sections, I will show experimental results on the electronic and frictional responses of 1T-TaS<sub>2</sub> studied with STM and pendulum AFM, respectively. The first question we would ask whether strongly pinned CCDW and the Mott gap is the reason for high Joule dissipation at low temperatures.

### 4.3 Study on the electronic properties of 1T-TaS<sub>2</sub>

Electron-electron and electron-phonon coupling have a great impact on the complex structural and electronic properties of the sample. Both electron-phonon and electron-

## 4.4. Study on energy dissipation mechanisms on 1T-TaS<sub>2</sub>

electron interaction contribute to the observed CDW. The sample was studied by STM using a metallic cantilever at T=77K. An atomic-level resolution was achieved, and Scanning Tunneling Spectroscopy (STS) was performed at temperatures T=77 K and T=5K. STM and STS measurements were performed with Au coated tip with ATEC geometry cantilever and with spring constant k=40 N/m. The STM was measured in constant current mode.

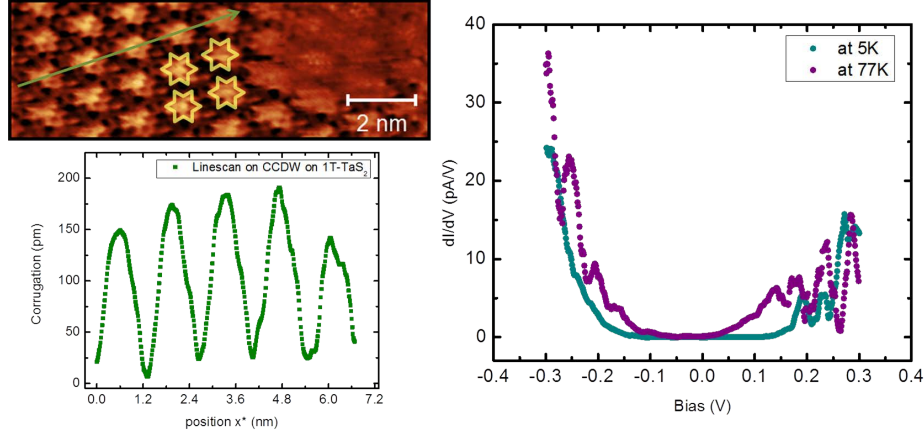


**Figure 4.4:** STM data shows atomic level resolution on CCDW on 1T-TaS<sub>2</sub> with David star formation at 77 K. 1.28 nm periodicity can be measured on the line scan along the superlattice(left). Tunneling parameters for STM data:  $I_t=400$  pA ,  $V_b=1$  V. Differential conductance at 5K is compared to differential conductance at 77 K.

David star formation was marked with yellow stars on STM data shown in figure 4.4. The line scan over the superlattice is also shown. The period of the superlattice is measured to be equal to 1.28 nm, where the theoretical value is 1.2 nm. The corrugation of David star is equal to  $150 \pm 10$  pm. Relatively huge corrugation is due to the protrusion of Ta atom at the center of David star, which is a result of surrounding Ta atoms coming closer to the center.

STS was performed on the same area, and the  $dI/dV$  (V) curve has been numerically derived from the measured  $I(V)$  curve. Differential conductance ( $dI/dV(V)$ ) at 77 K and 5 K are compared in figure 4.4. Mott gap has been measured 350 mV at 77 K, which is slightly smaller than the values reported before. However, the band gap I measured at 5 K is more close to the values already reported. The first impression STS data gives is that the band gap becomes wider at 5K due to the Mott insulating state.

## 4.4 Study on energy dissipation mechanisms on 1T-TaS<sub>2</sub>

### 4.4.0.1 Dissipation measurements at 5 K

Next force-distance spectroscopies were performed at 5K with relatively stiff and metallic cantilever (ATEC-NCAu) with a spring constant of k=52N/m and central

frequency  $f_0 \approx 250\text{kHz}$ . Oscillation amplitude  $A_{osc} \approx 3\text{nm}$  is used. Acquired force and dissipation data are averaged over several atomic sites due to relatively high oscillation amplitude, yet it can be considered as local.

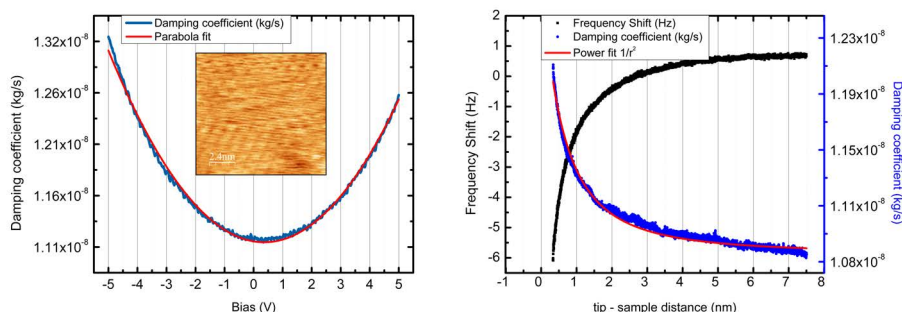


**Figure 4.5:** (Left) Damping coefficient depending on applied bias was taken on an area shown in STM data at 5K (inset). (right) Force and dissipation spectra on 1T-TaS<sub>2</sub> depending on the tip-sample distance at  $T=5\text{K}$ . 50 mV was applied between the tip and the sample to compensate contact potential difference. Inset data shows the STM image of 1T-TaS<sub>2</sub> surface at 5K with an atomic resolution and CDW.  $I_t=1.6\text{nA}$ ,  $V_b=30\text{mV}$ ,  $k=40\text{N/m}$ , amplitude  $A_{osc}=3\text{nm}$ , and  $f_0=256\text{kHz}$ .

I studied the energy dissipation on 1T-TaS<sub>2</sub> at 5K when the charge density wave is incommensurate phase together with the Mott insulating phase. The dissipation spectra (damping coefficient) shows a parabolic dependence on the applied bias. This parabolic behavior is attributed to the electrostatic interaction and Joule dissipation, between the cantilever and the surface. The STM data is shown in the inset with atomic resolution, but CCDW is not as pronounced as it is at 77K. Sample resistance at 5K is two orders of magnitude higher at 5K comparing to the resistance at 77K due to Mott insulating transition. The frequency shift and dissipation curves plotted in figure 4.5 shows the distance dependence of force and dissipation. The spectroscopy was performed by applying 50mV between the tip and the sample to compensate contact potential difference (CPD). Although CPD reduces the electrostatic interaction to a minimum by compensating the additional field due to work function difference of the materials, dissipation still shows a strong dependence on tip-sample distance. The curve was power fitted, and  $1/r^2$  dependence was found. Such dependence is the signature of pure electrostatic friction that can be measured on bulk structures.

After single spectroscopies, force and dissipation spectroscopy versus both bias and distance were performed. Figure 4.6 left (left) shows the frequency shift ( $\Delta f$ ) depending on applied bias and tip-sample distance. Although due to complicity we didn't calculate the force quantitatively using frequency shift data, we can say that the frequency shift is proportional to the force, meaning that the higher frequency shift corresponds to a higher force. The map shows that the force has a strong dependence on both bias and distance. The dissipation map is shown in the right of figure 4.6, and the dependence of dissipation on bias and distance is strong. That is also valid for  $\Delta f$

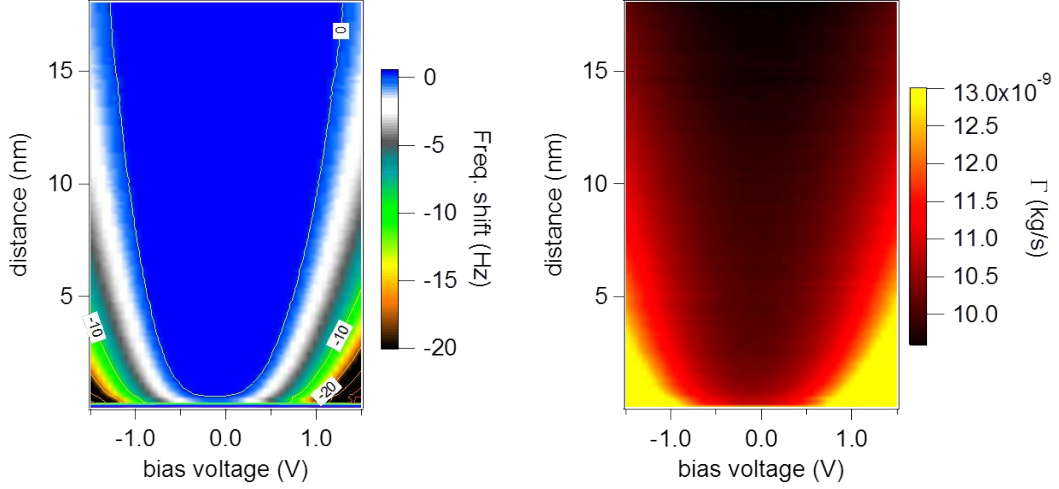


**Figure 4.6:** The  $\Delta f$  (force) map is shown on the left side. Map shows the dependence of the force to the applied bias and the distance between tip and the sample. Negative shift in the frequency means higher forces. Dissipation map measured simultaneously with force map is shown on the right side. Higher damping coefficient means higher dissipated energy. The spectra is taken by using gold coated ATEC geometry cantilever (ATEC-NCAu). Parameters:  $f_0=256\text{kHz}$ ,  $k=52\text{N/m}$ ,  $A_{osc}=3.3\text{nm}$ .

map. The damping coefficient is a measure of dissipation, and the minimum damping coefficient on this phase was  $1 \cdot 10^{-9}\text{kg/s}$ . If we calculate the power dissipation using the oscillation amplitude  $A_{osc}$  and the central frequency  $f_0$  of the cantilever we find the power dissipation in the order of few eV/cycle. In dissipation measurements typically meV/cycle power dissipation is measured for single/few electron charging-discharging events [33].

Considering this the dissipated power on this CCDW together with Mott insulating phase is humongous, however, understandable. Dissipation spectra strongly indicate that the primary dissipation mechanism is Joule dissipation, and it is proportional to the sample resistance. At low temperatures, the system tends to be more stable, and that is what's happening to 1T-TaS<sub>2</sub>. At  $T=5\text{K}$ , the CDW on the sample is strongly pinned as compared to pinning at higher temperatures. When the system is cooled down to 5K, CCDW triggers Mott insulating transition, which introduces higher resistance and leads to higher Joule dissipation.

#### 4.4.0.2 Dissipation study at room temperature

To compare the effect of different CDW phases on energy dissipation, similar force and dissipation spectroscopy were performed on the sample surface at room temperature ( $T=300\text{K}$ ). In figure 4.7, force (left) and dissipation (right) maps are shown. While the frequency shift doesn't show any dependence on distance and bias, the dissipation map shows dependence to both of them.

Force and dissipation map on the surface shows dissipation without net normal force. This situation can be understood if one assumes that the dissipation mechanism

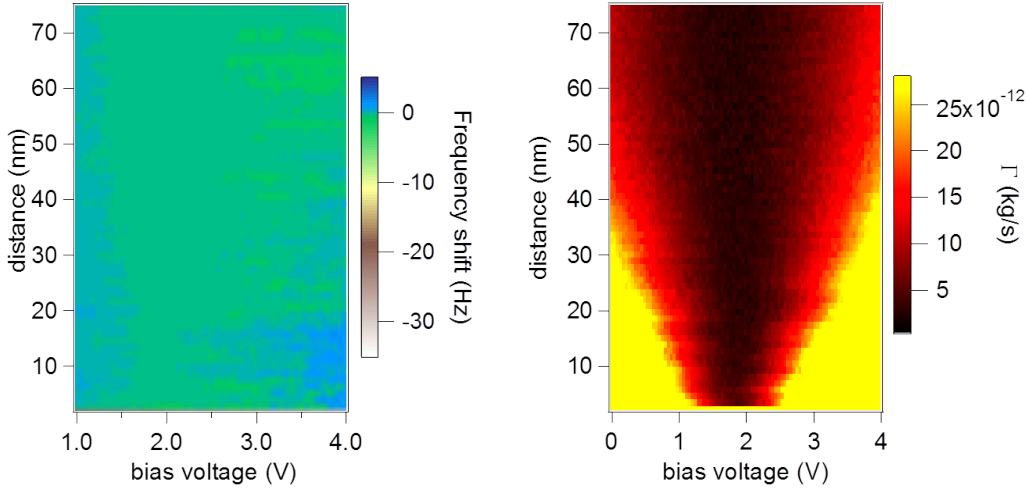


**Figure 4.7:** The  $\Delta f$  (force) map is shown on the left side. Dissipation map measured simultaneously with force map is shown on the right side. Higher damping coefficient means higher dissipated energy. While dissipation changes depending on distance and bias, force doesn't change. Parameters:  $f_0=12.225\text{kHz}$ ,  $k=0.12\text{N/m}$ ,  $A_{osc}=3\text{nm}$ .

is due to the fluctuation of the electromagnetic field. Averaged normal force can be zero while the system dissipates energy. The analog to what we measured on the NCCDW phase of 1T-TaS<sub>2</sub> is the Brownian particle. Single Brownian particle surrounded by other particles would be hit by those particles and possible be drifted from its original position when given enough time with the energy transferred to that particular particle from the surrounding particles. However, it wouldn't be possible to move it from its original position to the designated point because there is no net normal force acting on it. The direction of the forces is random, and the total force is zero because it is a vectorial quantity and they cancel out each other. The same thing applies here, considering the measurement of frequency shift. Normal forces contribute to the frequency shift, and if there are fluctuating forces present on the surface, the averaged net force measured by an oscillating tip may be zero, yet energy is dissipated.

Fluctuating forces and dissipation relation is given below by the fluctuation-dissipation theorem. Here  $\Gamma$  is the thermal average of the fluctuating force in the equilibrium state at fixed separation  $d$  between the tip and the sample.

$$\Gamma = \frac{1}{k_B T} \langle \mathbf{f}(t_0) \mathbf{f}(t_1) \rangle \quad (4.2)$$

In the geometry of pendulum AFM, we consider that the pendulum system operates in the linear regime which required a symmetry oscillation of the cantilever around the minimum. This symmetry oscillation may result with zero or very small net normal force if there is van der Waals interaction between the tip and the sample. However, one can favor the normal forces by using a larger oscillation amplitude thanks to the asymmetric shape of the cantilevers. If the oscillation amplitude is small, the oscillation would be symmetric. However for larger amplitudes due to tip asymmetry tip motion would be slightly favoured to one side thus making the sensor slightly sensitive to the



#### 4.4. Study on energy dissipation mechanisms on 1T-TaS<sub>2</sub>

normal force. Amplitude-dependent force distance spectroscopy was performed to try this idea.

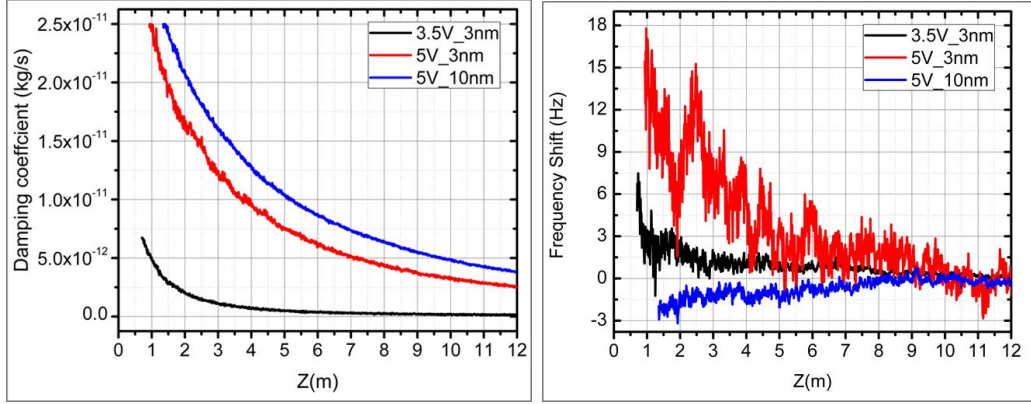


**Figure 4.8:** *Damping coefficient increases with an increasing amplitude or bias. Amplitude dependence of force curves show that if the amplitude is big enough, the averaged normal force can be different than zero so that negative frequency shift may be observed.*

In Figure 4.8, the force and dissipation distance curves are plotted for different amplitude and applied bias voltage. The black curve is with small oscillation amplitude  $A_{osc}=3\text{nm}$  and  $3.5\text{V}$ . It shows that the dissipation starts to rise for the tip-sample distance  $d \leq 6\text{nm}$ . On the other hand, force doesn't show a change till  $d=2\text{nm}$  and only shows a positive shift as it is in the repulsive regime in the Lennard-Jones potential without experiencing an attractive regime. The red curve obtained for bias voltage  $5\text{V}$  and  $A_{osc}=3\text{nm}$  is also consistent with the black curve. The dissipation starts to rise already at large distances, and force also follows that, but it doesn't show different behavior than the black curve. Force only rises due to the increased applied voltage. It needs to be mentioned that van der Waals interaction may be dependent on the applied voltage as the electric field is stronger for higher applied biases. Dissipation measured for larger oscillation amplitudes is slightly higher than the red one, but the force seems to be different. For the  $A_{osc}=10\text{nm}$ , frequency is slight shifts to a negative side. So far, the data in this figure are consistent within the measurement set, and  $10\text{nm}$  amplitude oscillation is needed to make the oscillation slightly asymmetric for the ATEC-CONT cantilevers. The presented data gives a strong hint that fluctuating random forces are the source of energy dissipation on 1T-TaS<sub>2</sub> surface at room temperature. To further examine this I performed the dynamic dissipation measurements by measuring the noise of the interacting force.

Origin of van der Waals friction was studied further by performing dynamic dissipation measurements. The power spectrum density (PSD) of the frequency shift is shown in Fig. 4.9. If there is an event that is triggered at a specific frequency (force), it shows itself as a peak in the graph. If only random forces are present, background noise is measured without any peak. Fluctuation itself is a source of the noise signal, and if there is a change in the environment or the behavior of it, the noise signal changes accordingly. The measurement was done to see the noise dependence measured on the

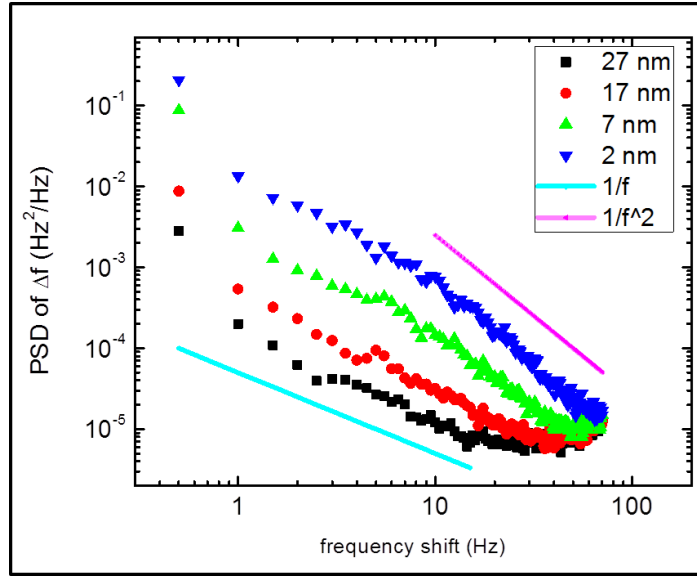


**Figure 4.9:** *Dynamic measurement shows that the fluctuating forces are the source of dissipation on 1T-TaS<sub>2</sub> surface. The character of the noise reflects a certain carrier dynamic on the surface. While the tip is positioned far from the surface the Power Spectrum Density of the  $\Delta f$  shows  $1/f^1$  dependence. The exponent 1 is characteristic for a semiconducting device, namely the cantilever. The noise behaviour changes to  $1/f^2$  when the tip-sample surface is reduced to a distance of 7 nm and exponent 2 is characteristic to the Brownian motion process.*

cantilever when it is far away from the surface and when it is interacting with the surface.

Figure 4.9 shows PSD curves for different tip-sample distances. Distance  $d$  is 27nm, 17nm, 7nm, and 2 nm, respectively. For  $d=27$ nm tip-sample interaction is negligible and the measured noise corresponds to the free oscillating cantilever and shows a  $1/f^1$  dependence. The exponent 1 is characteristic for many semiconducting devices. The cantilever is a highly doped Si cantilever that has uncompensated charges, deep trap states, etc. in the cantilever bulk. Oscillating the cantilever causes resistive switching of those charge centers and gives rise to  $1/f$  dependent noise. Similar behavior is seen for  $d=17$ . When  $d=7$  the curve starts to deviate from the  $1/f$  to  $1/f^2$ .  $1/f^2$  is more visible on the graph for  $d=2$ nm.

Dynamic measurement shows that the fluctuation-dissipation has a certain dynamic on the surface. As tip approaches to surface  $1/f$  noise starts to shift to  $1/f^2$  noise. Different from the free cantilever case, the exponent 2 is a signature of the Brownian motion process. The measurement strongly indicates that van der Waals friction is due to the random fluctuations of the weakly pinned charge density waves [34] at room temperature. Thus, weakly pinned CDW on the surface fluctuates collectively at finite temperature, generating fluctuation of the electric field. On the other hand, weakly pinned CDW are known to slide due to applied bias or pressure. In this case, there is no bias voltage applied, and the measurement was done in a non-contact regime, so the energy transferred to CDW is not enough to slide it but it is possible to disturb

CDW with an oscillating tip, and tip loses energy due to fluctuating electromagnetic field caused by wiggling motion of the CDW.

## 4.5 Summary

Experimental results show that energy dissipation mechanisms on 1T-TaS<sub>2</sub> strongly depend on the CDW phase. It is found that the Joule dissipation mechanism is the main dissipation channel on the CCDW at T=5K. The rise in Joule dissipation may be due to two reasons; one is the ordered strongly pinned CCDW, and the other one is the strong localization of electrons in the Mott state. At room temperature when the charge density wave is in a nearly commensurate phase, Joule dissipation is not enhanced due to the increased disorder in the system. There are three orders of magnitude difference between damping coefficients measured at 5K and room temperature. That is similar to the resistance change shown in Figure 4.3 (a). The damping coefficient on different phases on 1T-TaS<sub>2</sub> doesn't only show a difference in the magnitude, but the dissipation mechanisms are entirely different on two phases. Reduced Joule dissipation makes it possible to measure the van der Waals friction due to CDW fluctuations at room temperature so that van der Waals friction is the main dissipation mechanism at room temperature.

One can do further experiments on this particular system to study the transition to/from Mott insulating state by measuring dissipation while sweeping the temperature over the phase transition temperature. It is an electronic phase transition; therefore, it affects the sample resistance. Dissipation spectroscopy shows that the dissipation is high at the CCDW phase. However, it is not completely clear if it is due to CCDW or due to the Mott insulating phase. If one can make temperature-dependent experiments that trigger the system to get rid of Mott insulating state without disturbing the CCDW - dissipation measurements can be performed to see the contribution from Mott insulating state to dissipation. Such a study would help to develop a better understanding of the effect of electron-electron and electron-phonon coupling on energy dissipation. Sample can also be studied at CDW transition temperatures to see if the transitions are continuous or instant events.

In the next chapter, I will discuss the effect of electronic states on the dissipation on the topological insulator surface.



## Topological Insulator Surface - $\text{Bi}_2\text{Te}_3$

**B** $\text{i}_2\text{T}\text{e}_3$  has been studied for its thermoelectric properties and rediscovered as a topological insulator. Topological insulators (TI) attract great attention due to the potential use of the topologically protected surface electronic states in advanced communications and information processing systems, as well as in quantum computing [35]. A layered compound  $\text{Bi}_2\text{Te}_3$  is a model TI with prevented electron backscattering, long electron lifetimes [36–38] and reduced electrical resistance at low temperatures due to effect of weak anti-localization [39]. Although the electronic properties of topological insulators have been studied extensively, frictional response of their surfaces are yet to be reported. The impact of electronic structure and topologically protected surface states on the dissipative interaction between an oscillating tip and the sample is the scope of the present study.

Image potential states (IPS) on metallic surfaces [40–46] resembling Rydberg series were observed on several topological insulators [47–50], with the energy states lying slightly below the vacuum level. Angle-resolved two-photon photoemission (2PPE) studies of  $\text{Bi}_2\text{Te}_2\text{Se}$  surfaces reported on the first IPS to be at  $E = 4.5\text{eV}$  above Fermi level [49]. IPS are weakly coupled to the bulk in comparison to the other surface states. The lifetime of IPS on TI surfaces is in the order of fs, similarly to metallic surfaces [46]. Lifetime of the states are inversely proportional to the band gap in the surface projected band structure of the crystal. Lifetime of IPS on  $\text{Bi}_2\text{Te}_3$  is in the order of fs, comparable to the lifetime of IPS on metals, which is longer than expected considering its narrow bandgap [51]. In Scanning Tunneling Spectroscopy (STS), IPS are detected as Gundlach oscillations, which is a phenomenon of field emission resonance through IPS in the tip-sample gap [52]. The IPS are located a few nm away from the surface with increasing tendency for higher quantum numbers  $n$ . The wave functions of IPS were reported to be extended  $\sim 20\text{nm}$  away from the surface in two photon photoemission experiments [53]. Although, the presence of such IPS are well known, their impact on non-contact energy dissipation is not explored, so far.

Atomic force microscope (AFM) utilising a cantilever oscillating like a tiny pendulum over a surface is designed to measure extremely small non-contact energy dissipation and serve as an ultra-sensitive, non-invasive spectroscopy method [4, 5, 7]. It

has been shown that non-contact pendulum geometry AFM (pAFM) is sensitive to different types of energy loss mechanism in non-contact regime, where the oscillating probe is separated from the sample by a vacuum gap. In particular, phonon excitation [4], Joule ohmic dissipation [4]] or van der Waals dissipation [54, 6] were reported.

Here I performed Scanning Tunneling Spectroscopy (STS) with pAFM on a clean  $\text{Bi}_2\text{Te}_3$  surface. The measurement setup is described in Figure 1(a). Rydberg-like series of conductance maxima are observed by z-V spectroscopy, where the bias is swept with active feedback in constant current mode. These field emission resonances are very well resolved up to the fifth order [55]. Mechanical dissipation measurements by pAFM show increased energy losses at discrete separations and voltages up to distances of 14nm. Combined STM/pAFM measurements reveal that the Gundlach oscillations are accompanied by increased mechanical dissipation. Therefore, the enhanced dissipation losses at discrete separations and voltages is interpreted as related to charge fluctuations of the IPS. Tunneling processes lead to occupancy and de-occupancy of the IPS, which is detected by pAFM. If magnetic fields are applied, Joule-type dissipation rises, which is most probably related to the destruction of the topological protection, which opens the channel for scattering to bulk states giving rise to increased Joule dissipation as it is more common on ordinary metallic surfaces [4].

All experimental work discussed in this chapter were acquired by using ATEC-NCAu.

### 5.1 Crystal structure and topologically protected surface state

$\text{Bi}_2\text{Te}_3$  is a layered crystal with a trigonal unit cell with van der Waals interaction between the layers. A layer consists of  $\text{Te}^{(2)}\text{-Bi-Te}^{(1)}\text{-Bi-Te}^{(2)}$  is called as quintuple layer and Van der Waals planes lie between the quintuple layers [56]. When crystal is cleaved, it is cleaved between quintuple layers due to the weak interaction. Figure 5.1 (a) shows the unit cell of the  $\text{Bi}_2\text{Te}_3$ , (b) STM data on large scale showing clean  $\text{Bi}_2\text{Te}_3$  surface with two atomic steps on it, and (c) shows an atomic resolution with STM data and differential conductance ( $\frac{dI_t}{dV}(V)$ ) spectra that were measured on using scanning tunneling spectroscopy (STS) technique. The tip sample distance is kept constant by disabling the feedback and tunneling current is measured while the bias is swept. Differential conductance curve was numerically calculated from the  $I_t(V)$  data. Red fitting curve shows the position of where Dirac cone should be positioned. Position of Dirac cone can be determined by fitting a linear curve and find where it crosses 0 in differential conductance axis. I did not measure sharp dirac cone because of the contribution from the bulk of the crystal to the tunneling current. All the measurements were performed at 5K and using gold coated ATEC-NCAu with a spring constant  $k \approx 50$  N/m

## 5.2. STM and STS study on the electronic properties of $\text{Bi}_2\text{Te}_3$

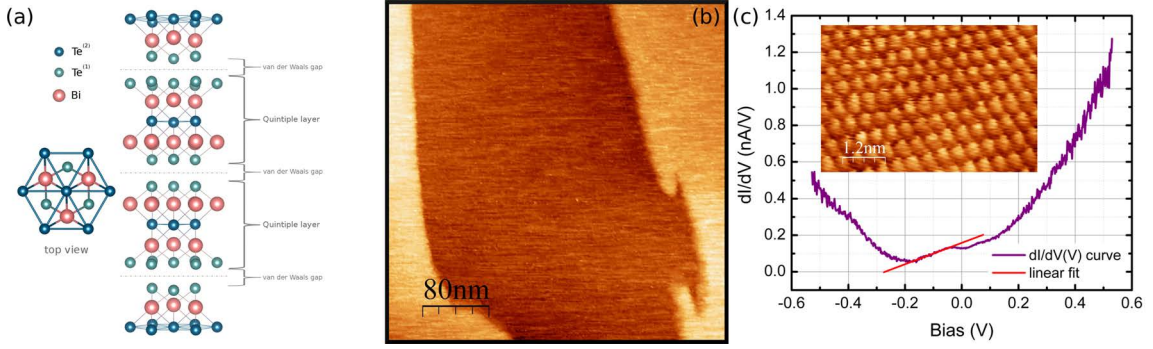


**Figure 5.1:** (a) unit cell of  $\text{Bi}_2\text{Te}_3$  showing quintuples and van der Waals gap. (b) Large scale STM image taken at 5K. (c) STS showing the Dirac cone together with STM topography (inset).  $dI/dV$  was numerically calculated from  $I(V)$  curve. Fitted curve on  $dI/dV(V)$  shows the Dirac cone. Tunneling parameters:  $I_t = 80\text{pA}$ ;  $V_s = 300\text{mV}$ .

## 5.2 STM and STS study on the electronic properties of $\text{Bi}_2\text{Te}_3$

First, I characterized the surface by means of STM and STS. The STM image in figure 5.1 (b) shows the large scale topography that was acquired in constant current mode at 5K with a gold-coated cantilever tip. A typical Scanning Tunneling Spectroscopy (STS) spectrum taken at close tip-sample distances is presented in Figure 5.1(c). The inset shows an atomically resolved topography image, acquired in constant current mode STM performed. Close to Fermi energy, the  $dI/dV$  spectrum reveals a linear dependence on bias voltage and the linear part of the curve crosses the voltage axis at about  $V_s = -0.3\text{V}$  bias voltage. Depending on the crystal growth conditions and doping, values between  $-0.1\text{V}$  to  $-0.4\text{V}$  have been reported [57, 58, 49]. The similar linear density of states, resembling a Dirac cone, is a signature of the topologically protected surface state of pristine  $\text{Bi}_2\text{Te}_3$  [59]. It is reasonable to assume that the topologically protected electronic structure of the  $\text{Bi}_2\text{Te}_3$  surface is preserved [59].

$z(V)$  spectroscopy measurements were performed by a continuous sweep of the tip-sample voltage while keeping the current constant by the STM feedback. Thus, the STM tip retracts if there is an increase in the tunneling current thereby revealing Rydberg-like series of electronic states as shown in Figure 5.2. The total change of tip-sample distance  $z$  observed between the  $V_s = 1\text{V} - 10\text{V}$  voltage sweeps is about  $2.5\text{nm}$ , showing 6 step-like increments. The change of each  $\Delta z$  step is about  $300\text{pm}$ . The first peak ( $n=0$ ) located close to  $V_s = 5\text{V}$  is related to the local work function [44] of the surface.  $z(V)$  spectra show a sequence of field emission resonances numbered by the quantum numbers,  $n=0,1,2,3,4,5$ , which are clearly visible in the differentiated  $z(V)$  curves as shown in Figure 5.2. Recent 2PPE experiments on bismuth rich surfaces reported IPS [47–49, 60, 50], and apart from Rydberg-like series, a peak localized at  $2.5\text{eV}$  energy, which is present in our STS data as well. In local probe measurements its presence is location dependent and thus it might be related to the subsurface defect or interlayer/interface states [61, 22]. The IPS of the tip is showed in Figure 5.4. The

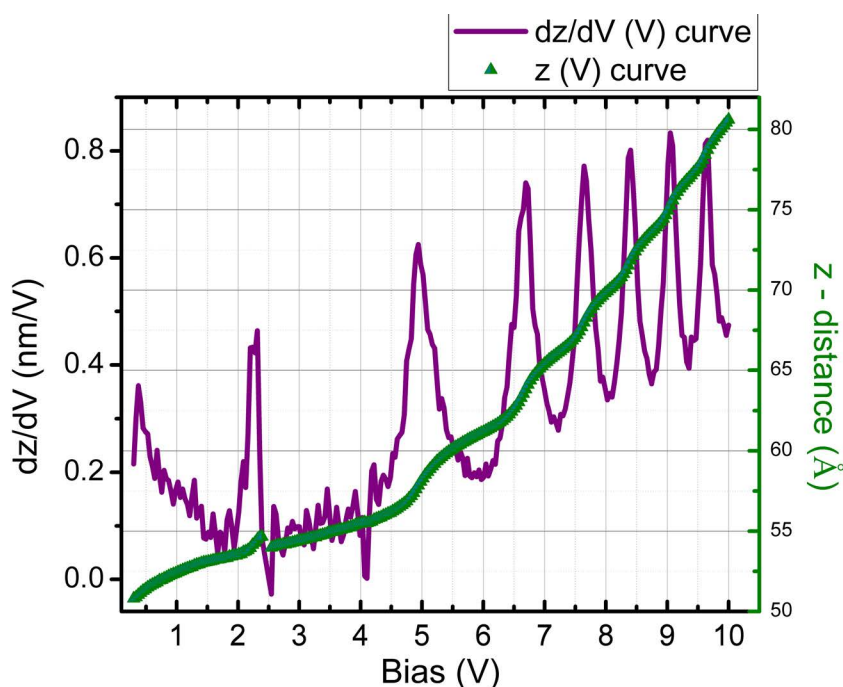


**Figure 5.2:**  $z(V)$  curve (green) showing series of image potential states measured between the STM tip and  $\text{Bi}_2\text{Te}_3$  surface. The feature appeared close to 2V may originate from surface/subsurface or interlayer states. Steps present above 5V are the image potential states of the crystal that are measured above the surface. Numerically derived  $z(V)$  curve is plotted on  $z(V)$  curve. Peak positions on  $dz/dV(V)$  curve corresponds to the energy position of IPS

peaks are more broadened compared to the IPS of the sample. It needs to be mentioned that, since the STM measurements are performed with a tip mounted on a cantilever, the static deflection of the sensor was monitored. Forces in the range of  $pN$  were detected.

### 5.3 STM study on the IPS on $\text{Bi}_2\text{Te}_3$ with an oscillating tip

It has been shown in the previous chapters that pendulum geometry AFM is sensitive to different types of non-contact energy transfer, namely phonon excitation, Joule ohmic dissipation or van der Waals dissipation originating from charge fluctuations between surface and the probing tip. Here we bring together the results from Scanning Tunneling Spectroscopy (STS) and measurements of energy dissipation experienced by a sharp AFM tip oscillating with lateral amplitude  $A=500$  pm over atomically clean surface cooled down to  $T=5K$  temperature. At selected tip sample distances and bias voltages conductance maxima are observed in tunneling current signal. We attribute those maxima to the single electron field resonances localized between the probing tip



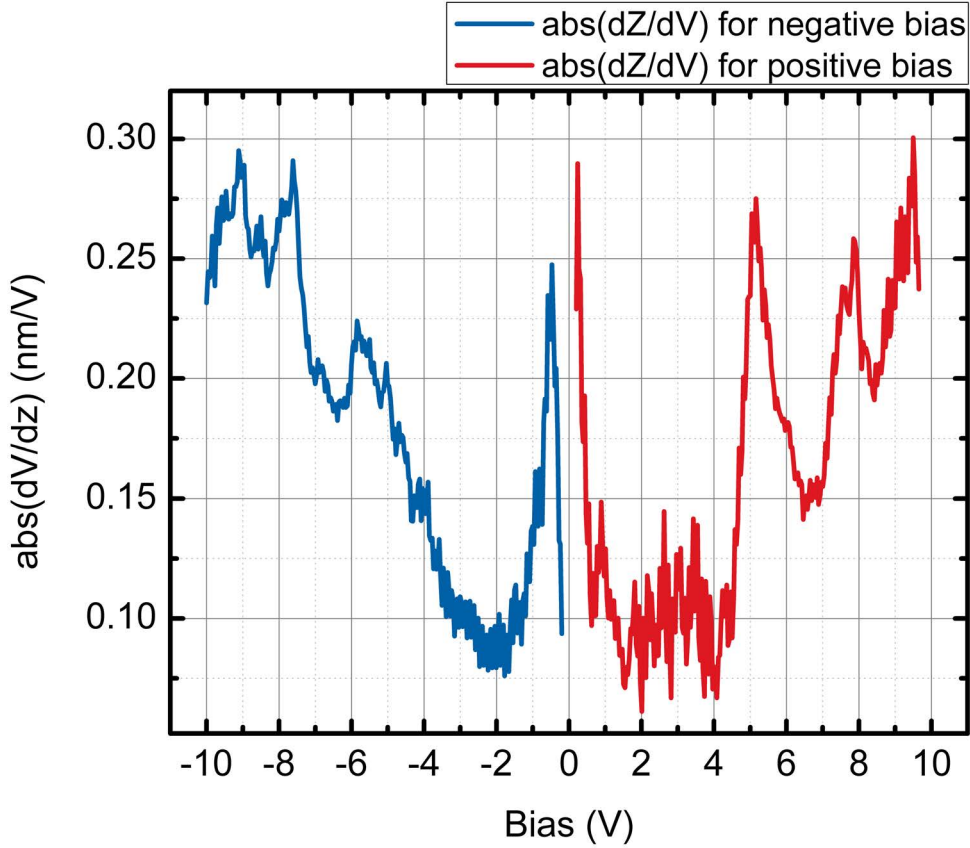


**Figure 5.3:**  $dz/dV$  (V) curve showing the IPS measured for both positive and negative sample bias. While IPS of the sample are probed at positive sample bias, IPS of the tip are probed if sample bias is negative.

and sample. The existence of such Rydberg series, known as IPS on the surface is first confirmed by means of STS. Simultaneous STM/AFM measurements with oscillating STM tip showed that every resonance tunneling into the primarily unoccupied IPS is accompanied by huge peak in energy dissipation of the cantilever oscillation. Furthermore, we show that AFM dissipation signal is sensitive to Rydberg series of IPS even at distances of 12nm above the surface - far away from tunneling regime. We attribute dissipation peaks to charging and discharging the IPS as the oscillating tip modulates the bias voltage locally in a very similar manner as it was already shown in the case of quantum dots, with discrete energy spectrum. The observed phenomenon may be regarded as the completely non-invasive force version of the image potential resonance tunneling. The method, is non-invasive and insensitive to the deformation of the measured structures. Furthermore, measurements in magnetic fields demonstrates that the topologically protected surface state is crucial for observation of dissipation peaks due to suppression of electronic, Joule type of dissipation which usually is the main dissipation channel on ordinary metallic surfaces.

While STM is a known, standard tool for electronic structure characterization

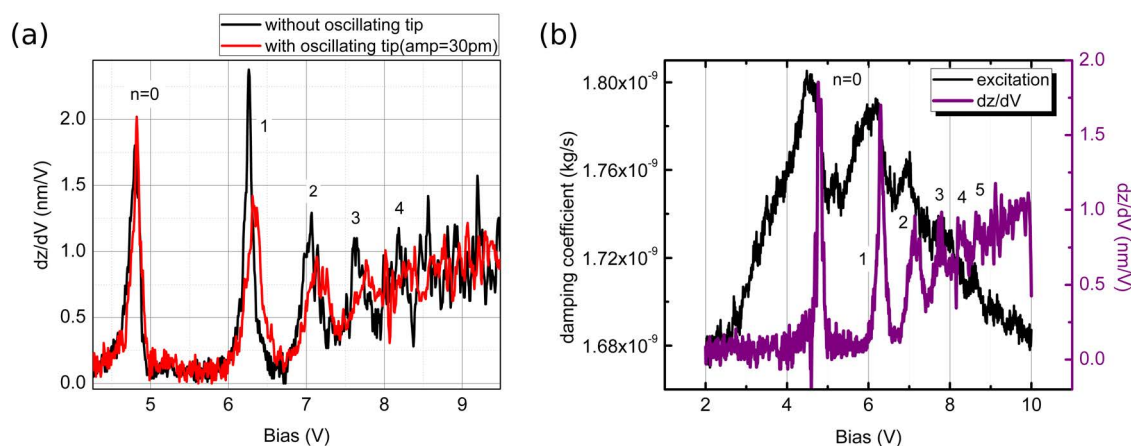


**Figure 5.4:**  $dz/dV$  measurements performed at the same surface spot with static (black) and oscillating (red) STM tip. The amplitude of lateral oscillation was equal to 30pm and the number  $n$  numerates the subsequent image potential states. As compared to static situation, the oscillating tip substantially broadens the IPS localized at bias voltages  $V_b \gtrsim 5V$ , while  $n=0$  image potential state localized at  $V_b = 4.8V$  is unchanged in dynamic measurements. b) simultaneous STM- $dz=dV$  (violet) and AFM-dissipation (black) measurements performed by oscillating tip. The field emission resonances visible in  $dz/dV$  spectra is accompanied by series of AFM nanoscale dissipation features.

[17, 18, 62], AFM measures the mechanical properties of surfaces [63, 64]. We performed combined STM/AFM spectroscopy measurements, namely  $z(V)$  dependence with oscillating STM tip in order to understand the relation between those states and energy dissipation. Energy dissipation of the cantilever was monitored, while simultaneously measuring the tunneling current between the tip and the  $\text{Bi}_2\text{Te}_3$  surface. The amplitude of lateral oscillations during combined STM/AFM spectroscopy measurements by pAFM was set to  $\sim 30\text{pm}$ . Due to the geometry of the tip, this results in amplitude variations normal to the surface of 2–3pm. This is two orders of magnitude smaller than the change of tip-sample distance  $\Delta z$  observed in  $z(V)$  curves. In Figure 5.4(a)  $dz/dV$  data show the IPS related resonances for static (black) and oscillating (red) STM tip.

The tip oscillation substantially changes the IPS spectra as compared to the static situation. IPS localized at bias voltages  $V_b > 5V$  are broadened by a factor of 2, while  $n=0$  IPS localized at  $V_b = 4.8V$  is almost unchanged in dynamic measurements. In both cases the width of the IPS proves that IPS on  $\text{Bi}_2\text{Te}_3$  surface are relatively long lived, with the lifetime of fs, in agreement with other studies. Moreover, oscillating tip spectra report on broadening of IPS, as compared to static situation. The tip oscillation smears out the IPS with  $n > 4$ , presumably due to reduced sensitivity at far distances and intermixing the states with high  $n$  number by the tip induced oscillating tunneling barrier. The tip oscillations allow to measure the dissipated energy on  $\text{Bi}_2\text{Te}_3$  surface and simultaneous STM and AFM measurements are shown in Figure 5.5 (b), where series of IPS is accompanied by sudden changes in dissipation signal. Here, again four IPS are visible. The dissipation signal rises for each quantum number. The drop of the

dissipation towards the maximum of the  $dz/dV$  curves is related to the  $z$  retraction of the  $z(V)$  spectroscopy. Although the frictional response of the AFM is known to depend on tip-sample distance and bias voltage that is applied between the tip and the sample [4, 54], the simultaneous increase of the dissipation signal and the correspondence to the series of IPS provides strong evidence that both phenomena are linked together, and the field emission resonances affect the mechanical nano-dissipation on Bi<sub>2</sub>Te<sub>3</sub> surface.

### 5.4 pAFM study on the energy dissipation mechanisms on Bi<sub>2</sub>Te<sub>3</sub>

After the topographic and spectroscopic characterization of the Bi<sub>2</sub>Te<sub>3</sub> surface, we measured the mechanical energy dissipation between oscillating pendulum-AFM tip and the sample as a function of applied tip-sample bias voltage and distance. Apart from provoking such conventional forms of energy transfer as phonon and Joule ohmic dissipation [65, 4], the external perturbation caused by an oscillating tip might push a finite quantum system towards a transition or a level crossing with subsequent relaxation of the system, that eventually resulting in the enhancement of energy loss [33, 66, 5]. On Bi<sub>2</sub>Te<sub>3</sub> surface, we claim that the energy losses occur when the oscillating tip couples to the charge fluctuations of IPS to electron tunneling. In the AFM mode, the tip is retracted away from the STM operation distance and the feedback is switched from STM to AFM operation. The tip is oscillated with 300 – 400pm lateral oscillation amplitude and the oscillations perpendicular to the sample are in the order of 30pm. Before measuring dissipation, the tip-sample distance and oscillation amplitude are controlled in order to exclude modulation currents due to the cantilever oscillation. After retraction, the sample bias was swept between 10V to -10V while the tip is grounded and dissipation and frequency shift spectra are recorded. The pendulum AFM voltage dependent measurements show parabolic dependence of the frequency shift ( $\Delta f$ ) and non-monotonic dissipation, as shown in Figure 5.5(a). At 5nm tip-sample separation, we observe the first peak in dissipation data located at  $V = \pm 7.4V$  and a second peak at  $V = \pm 8.5V$ . Both are symmetric with respect to contact potential difference (CPD) (see Supplementary Information section S3). This is in analogy to AFM measurements of weakly coupled quantum dots [67] or molecules in break junctions [68], where the voltage drop is divided across two capacitances (tip-molecule capacitance and molecule-sample capacitance). If the capacitances are comparable, symmetric case is observed. The  $\Delta f$  signal acquired simultaneously with dissipation signal shows deviations from the simple parabolic dependence which coincides with the position of the enhanced dissipation, meaning after each dissipation peak, cantilever tip-sample capacitive coupling changes and the tip is subject to slightly different force fields.

The distance dependence of energy dissipation is shown in Figure 5.5 (b). The data were obtained by approaching the tip towards the Bi<sub>2</sub>Te<sub>3</sub> sample with a constant voltage of  $V_s = 9V$ . Two main features are present in the dissipation versus distance

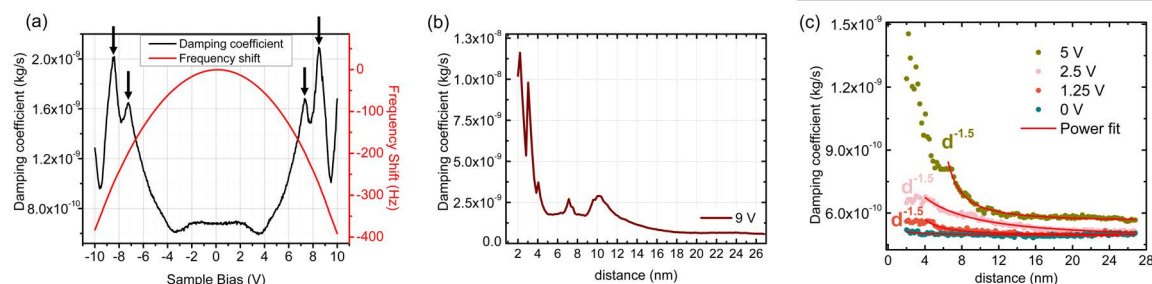


**Figure 5.5:** Tip-sample voltage dependent dissipation (black) taken at constant tip-sample distance  $d=5\text{nm}$  shows series of dissipation enhanced features marked by arrows positioned symmetrically with respect to bias voltage  $U_b = 0\text{V}$  and located roughly at  $U_b = -7.4\text{V}$  and  $U_b = -8.5\text{V}$ : Simultaneously with dissipation the frequency shift signal (red) was acquired. The lateral oscillation amplitude was equal to  $A=300\text{pm}$  oscillation amplitude ( $f_0=269\text{kHz}$ ,  $k=58\text{ N/m}$ .)

spectra: Firstly, a series of dissipation peaks at  $z = 2, 6, 10\text{nm}$  distances are observed. Secondly, we notice an overall rise of dissipation plateau after tip approaches to the first dissipation peak. At distances larger than  $z > 10\text{nm}$  the minimum value of damping coefficient is equal to  $\Gamma = 7.0 \cdot 10^{-10}\text{kg/s}$  and then levels off to be about  $\Gamma = 2 \cdot 10^{-9}\text{kg/s}$  at closer tip-sample distance. This rise of dissipation plateau after the first dissipation peak suggests the opening of a specific dissipation channel at distances closer than  $z = 9\text{nm}$  and tip-sample voltage  $V_s = 9\text{V}$ . Distance - dependent dissipation spectra measured at sample bias  $V_s \leq 5\text{V}$  are shown in Figure 5.6 (c). The spectra show  $d^{-3/2}$  power law in agreement with the theory of non-contact dissipation on thin metallic film on an insulator [6, 1].

The dissipation map in Figure 5.6 shows the distance and voltage dependence of the damping coefficient  $\Gamma(V, z)$  of the cantilever. Red arrows mark the positions of the dissipation peaks on the map. The maxima are observed at non-zero biases even at close distances, which indicates that dissipation is not force but voltage controlled. It has to be noted that the van der Waals force present at lower biases cannot cause the discussed dissipation features. Similar to the case of charging of quantum dots [33, 66], the amount of dissipated energy is also in the order of tens of meV per cycle indicating a single electron tunneling process. The position of dissipation peaks shifts linearly towards higher bias voltages with increasing tip-sample distance due to the decrease of capacitive coupling between tip and sample. This is shown in detail in Figure 5.6, and the measurement reported on lever arm  $\alpha = 3\text{nm/V}$ . Thus, at far distances, the voltages of dissipation features are shifted compared to the voltages observed by STM. This can be understood by taking into account that AFM data are influenced by the voltage drop across the vacuum gap, which is divided by the two effective capacitances  $C_{tip}$  and  $C_{sub}$  (see Figure 5.6). At very close distances below 4 nm, we observe a nonlinearity in tip-sample capacitive coupling. This suggests that the tip radius  $R$  is approximately equal to 4nm [9]. The extrapolation of the first dissipation maximum to the  $d \leq 1\text{nm}$ , a working distance of STM, results in comparable energy scale seen by STS.

## 5.5 Energy dissipation on Bi<sub>2</sub>Te<sub>3</sub> under external magnetic field

To further examine the effect of magnetic field on the dissipation and corroborate on the effect of weak anti-localization [39, 69] we performed the dissipation measurements under external magnetic fields ranging from  $B = 0 - 0.8\text{T}$  oriented perpendicularly to the sample surface (see Figure 5.7). The tip was positioned at a 5 nm distance above the surface. As the magnetic field rises, dissipation maxima become less pronounced, and the overall dissipation background raises as marked by green arrows in Figure 5.7. The spectrum obtained for  $B = 0.8\text{T}$  resembles the common Joule dissipation parabolic shape obtained on ordinary metal surfaces [4]. Moreover, there is a rise of the overall dissipation background even for compensated CPD voltage ( $V_{CPD} = 0V$ ) as shown in Figure 5.7. Thus, it concludes that Joule dissipation, connected to bulk connectivity, rises for a magnetic field  $B > 0.2\text{T}$ , where the spin-momentum locking appears to be destroyed, and back-scattering becomes prominent. According to Kohler's rule  $R(B)/R(0) \approx 1 + (\mu B)^2$  [39, 70] the metallic sample resistivity in the weak magnetic field limit exhibits a  $B^2$  dependence, where  $\mu$  is the mobility of the film. Since the dissipated power is proportional to the magnetoresistance of the sample, the dissipation curve should show a parabolic dependence on  $B$ . The parabolic fit of the data for  $B > 0.2\text{T}$  is shown as a solid red line. Accordingly, it shows that AFM dissipation is sensitive to the effect of weak anti-localization, the unique property of the topological matter and the suppression of Joule type of dissipation on topologically protected surfaces is crucial for observation of dissipation due to the presence of image potential states.

## 5.6 Discussion

To corroborate onto the origin of observed energy dissipation we first estimate the damping coefficient following theoretical predictions given by Volokitin et.al. [6] and formula (19.73) therein:

$$\Gamma = \frac{(4\pi\epsilon_0)^2 w (V^2 + V_0^2) R^{0.5}}{2^{9/2} \pi \sigma d_f d^{3/2}} \quad (5.1)$$

The theoretical model considers a metallic film on top of an insulating/semiconducting bulk substrate. Such a model accounts for the topologically protected electronic structure of the sample and the measured dissipation versus distance (see Figure 5.5) indeed follows  $\Gamma \propto d^{-3/2}$  dependence. A more detailed analysis with this model seems not adequate because of the lack of knowledge of the parameters for the case of TI.

In Figure 5.5 the dissipation maxima shifts with voltage and distance, due to voltage division between  $C_{tip}$  and  $C_{sub}$ . The symmetry of the curves is in analogy to nc-AFM measurements of quantum dots [67] and molecules on thick insulators [71]. The symmetric appearance is also common in break junction experiments, where resonant tunneling is observed at both polarities [68]. At the voltages, where dissipation maxima occur, we do observe small irregularities in the  $\Delta f$  signal which fit well two capacitor

model with different values for  $C_{tip} = 0.17aF$  and  $C_{sub} = 0.8aF$  at  $d = 5nm$  tip-sample distance. The ratio  $C_{tip}/C_{sub} = 0.2$  gives the position of IPS above the Bi<sub>2</sub>Te<sub>3</sub> surface equal to  $z = 0.4nm$ , which is a realistic estimate. Moreover, experiments with different tip material show that the positions of dissipation peaks and related  $\Delta f$  are symmetric with respect to CPD, as expected for a two-capacitor model (Figure 5.7 and 5.8).

Our low-temperature ( $T = 5K$ ) AFM dissipation spectroscopy experiments showed multiple mechanical dissipation mechanisms over a topological insulator surface. The dissipation spectroscopy performed at tip-sample distances as large as several nm is sensitive to single electron tunneling into IPS. We attribute the observed dissipation peaks to charge fluctuation (van der Waals friction) in the system present when the IPS are occupied via single/few electron tunneling. The observation of IPS related dissipation features requires the suppression of Joule type of losses that is very small or absent on topologically protected surfaces due to lack of electron back-scattering. Joule and van der Waals type of energy losses are in the same order of magnitude on Bi<sub>2</sub>Te<sub>3</sub> surface. When an electron tunnels to the IPS, van der Waals dissipation increases due to increased charge fluctuations, while Joule dissipation decreases due to the screening effect. On the other hand, at larger magnetic fields ( $B > 0.2T$ ), we observed an increase in Joule dissipation due to the increase in electron back-scattering. As a result, dissipation peaks become less pronounced. The electronic characterization provided by the AFM mechanical dissipation peaks reported here may be used as an efficient and completely noninvasive tool for topological surface analysis, of considerable importance for nanotechnology. Finally, we demonstrated that pendulum AFM can address quantum effects in energy dissipation.

### 5.7 Summary

To summarize, IPS were measured on topological insulator surface using STM for the first time. This measurement opened up a possibility to perform dissipation spectroscopy with the presence of IPS on topological insulator surface. Low-temperature ( $T = 5K$ ) AFM dissipation spectroscopy experiments reported on multiple mechanical dissipation peaks over a topologically protected surface state on Bi<sub>2</sub>Te<sub>3</sub>. They are attributed to the field emission resonances through image potential states present in the tip-sample gap. Magnetic field dependent measurements showed that observation of dissipation features requires absence of Joule type of losses or Joule dissipation may shadow the features measured in dissipation spectroscopy. In this sample Joule dissipation is very low or absent due to topologically protected surface state, hence, the lack of electron back-scattering. The electronic characterization is linked with the mechanical dissipation peaks and the method can be used as an efficient and completely noninvasive tool for surface analysis, of considerable importance for nanotechnology. Dissipation measurements were linked to the IPS thanks to the combined STM and AFM study. The dissipation spectroscopy was performed at distances as large as several nm and is sensitive to single electron tunneling into image potential states, orders of magnitude below the standard I/V converter measurement limit. It is demonstrated that pendulum AFM can address quantum effects in energy dissipation.

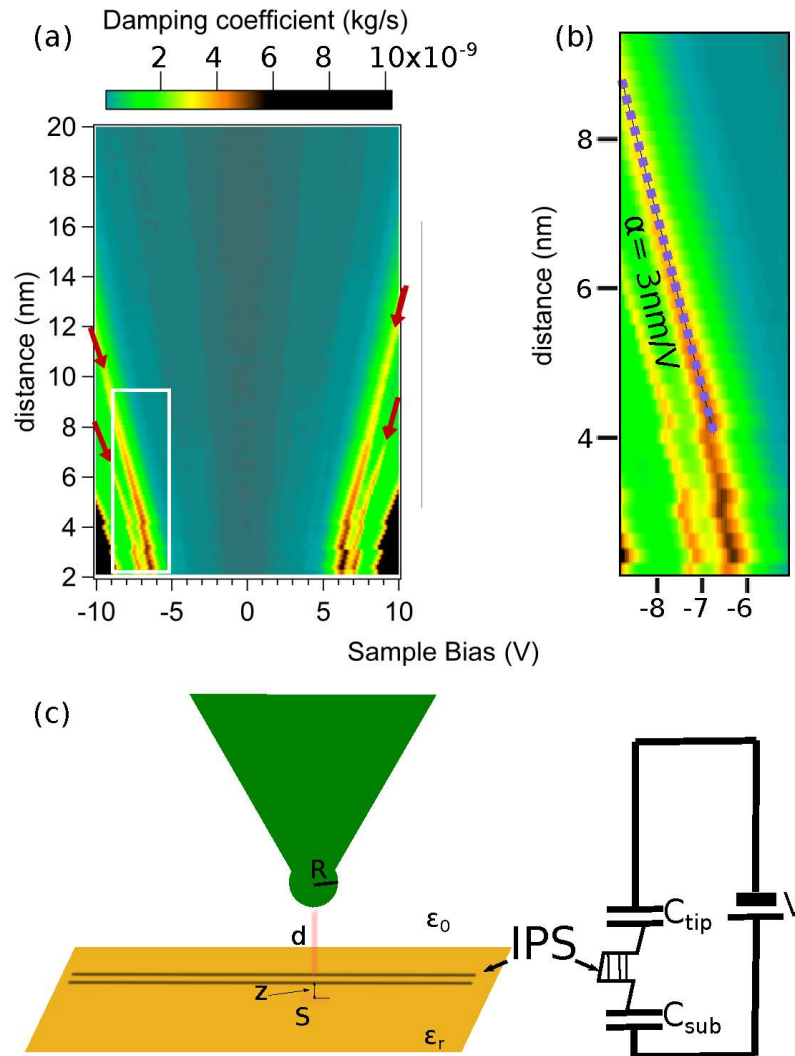


**Figure 5.6:** Energy dissipation map on  $\text{Bi}_2\text{Te}_3$  plotted versus distance and tip-sample voltage. Darker contrast represents four large dissipation features marked by red arrows. The white rectangle marks the region shown in b, b) shows the detailed zoom of the dissipation map for bias voltage between  $-9\text{V} < V_s < -5\text{V}$ . The schematics of the tip-sample geometry and the equivalent electrical circuit is shown in c, where  $R$ ,  $d$ ,  $z$  and  $S$  stands for tip radius, tip distance to the IPS, the distance of IPS to the surface and tip projected active surface area, respectively.

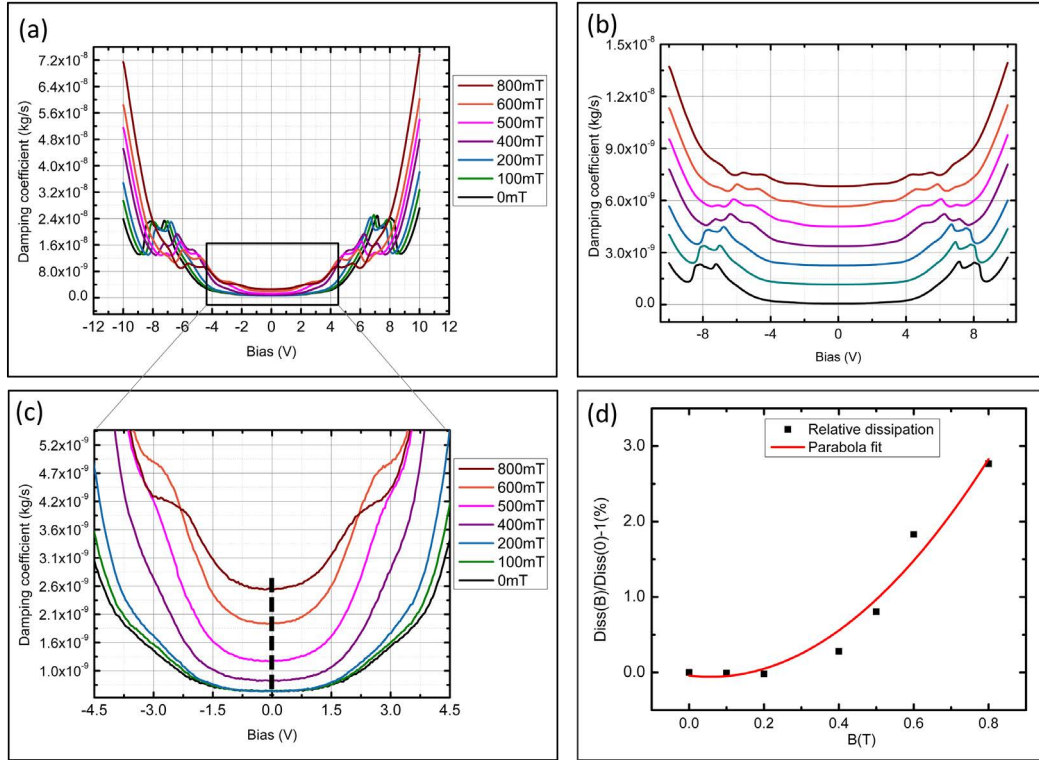


**Figure 5.7:** On (a) dissipation versus bias for different external magnetic field is shown. The tip is at a constant distance  $z=5\text{nm}$  from the surface. Constant vertical shift is applied to curves for visibility. Black curve with well pronounced two peaks is for  $B = 0\text{T}$  and there are two peaks visible on the curve. As the magnetic field rises overall Joule type of dissipation increases and dissipation features gets suppressed. This effect is best visible in proximity of the dissipation peaks as marked by arrows. On (b) relative energy dissipation change versus magnetic field measured by p-AFM dissipation spectroscopy onto a topologically protected surface state on  $\text{Bi}_2\text{Te}_3$ . The strong rise of dissipated power above  $B=0.3\text{T}$  is likely related to the breaking of topologically protected surface state by the  $B$  field.



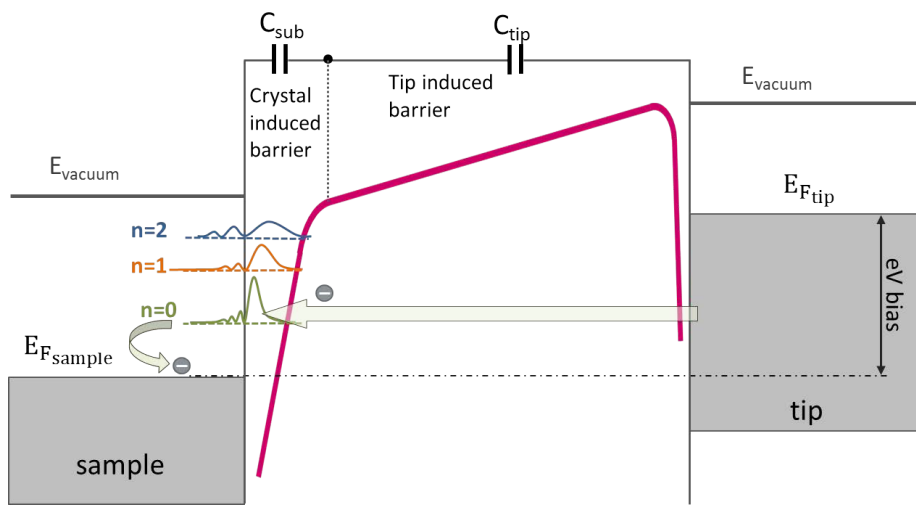


**Figure 5.8:** Single electron tunneling between IPS of  $\text{Bi}_2\text{Te}_3$  sample and an oscillating AFM tip. With positive bias voltage applied to the sample, the conditions for single/few electron resonant tunneling is created between tip and sample through the IPS at the gap. The tunneling process increases the charge fluctuations in the system and thus enhances AFM dissipation. The electric field applied between tip and sample is in the order of  $E \sim 10^9 \text{V m}^{-1}$ , and the tip-IPS and IPS-sample capacitances are marked  $C_{\text{tip}}$  and  $C_{\text{sub}}$  respectively.



## 2DEG system - $\text{Sr}_2\text{TiO}_3$

### 6.1 Strontium titanite (STO)

AMONG the all 2D layered compounds the  $\text{Sr}_2\text{TiO}_3$  surface might become the exotic one in relevance to the present study. It does not belong to the family of intercalated compounds. However, the presence of 2-DEG on the surface and surface vacancies let me treat the system also as 2D- material. Strontium titanate stands out among other oxides as a material with a broad spectrum of physical phenomena and functional properties. Throughout the last decades, the interest in  $\text{Sr}_2\text{TiO}_3$  has increased due to its popularity as a versatile substrate for oxide electronics research and engineering [72, 73]. Extreme electron mobility and superconducting properties [74–76], quantum paraelectricity in bulk [77], itinerant, impurity, and vacancy based magnetism [78, 79, 73] of  $\text{Sr}_2\text{TiO}_3$  have been subjects of fundamental studies. In particular, charge trapping by oxygen vacancies ( $V_o$ ) [80] and vacancy related magnetism [81–84] are pertinent to this chapter. Pristine  $\text{Sr}_2\text{TiO}_3$  develops oxygen vacancies when grown or annealed under oxygen-poor conditions [85], bombarded with noble gas ions [86], or under intense laser or ultraviolet irradiation [87]. When in numbers,  $V_o$  can lead to the formation of two-dimensional electron gas (2DEG) on the surface of bare  $\text{Sr}_2\text{TiO}_3$  [88–91]. Moreover, oxygen vacancies were shown to be inherently magnetic both in bulk  $\text{Sr}_2\text{TiO}_3$  [92, 83, 93] and at its surface [94–99, 76, 100, 84]. They were shown to exhibit either local uncorrelated magnetic moments [92, 101] or stable long-range magnetic order, when present in sufficient concentration [102, 97, 83, 103, 76, 100, 104]. Here we measure the dissipation experienced by a sharp AFM tip oscillating at a range of lateral amplitudes ( $100 \sim pm$  to  $5 \sim nm$ ) over an oxygen deficient  $\text{Sr}_2\text{TiO}_3(100)$  single crystal surface cooled down to low temperatures of  $T = 5K$ . At selected tip-surface distances and bias voltages, dissipation peaks are observed in the cantilever oscillation. We attribute these peaks to charge and spin state transitions in individual or possibly collective groups of oxygen vacancies, which act as natural quantum dots at the oxygen-deficient surfaces of STO, as suggested by recent first-principles calculations [84]. We further discuss possible pathways for electrons which could give rise to these transitions under the action of the time-periodic electrostatic or van der Waals poten-

tial exerted by the AFM tip. The dissipation peaks appear at large crystal reduction (therefore with many surface vacancies), and long tip-sample distances (even above 10 nm), disappearing above  $T = 80 - 90\text{K}$ . While these elements point to a collective mechanism involving many vacancies, we find that the crude single vacancy model already provides a helpful understanding. Here we measure the dissipation experienced by a sharp AFM tip oscillating at a range of lateral amplitudes ( $100 \sim \text{pm}$  to  $5 \sim \text{pm}$ ) over oxygen deficient STO (100) single crystal surface cooled down to low temperatures of  $T = 5\text{K}$ . At selected tip-surface distances and bias voltages, dissipation peaks are observed in the cantilever oscillation. We attribute these peaks to charge and spin state transitions in individual or possibly collective groups of oxygen vacancies, which act as natural quantum dots at the oxygen-deficient surfaces of STO, as suggested by recent first-principles calculations [84]. We further discuss possible pathways for electrons which could give rise to these transitions under the action of the time-periodic electrostatic or van der Waals potential exerted by the AFM tip. The dissipation peaks appear at large crystal reduction (therefore with many surface vacancies), and long tip-sample distances (even above 10 nm), disappearing above  $T = 80 - 90\text{K}$ . While these elements point to a collective mechanism involving many vacancies, we find that the crude single vacancy model already provides a helpful understanding.

## 6.2 STM Results

Surface morphology and chemical composition of STO are known to change significantly under high-temperature annealing. We thus start our study by examining the topography of  $\text{Sr}_2\text{TiO}_3$  with a scanning tunneling microscope (STM) between cycles of annealing at subsequently increasing temperatures. While rough and irregularly-shaped at low annealing temperatures,  $\text{Sr}_2\text{TiO}_3$  surfaces develop a well-defined terrace and island structure after prolonged annealing at about  $800^\circ\text{C}$  forming a range of reconstruction patterns [ $2 \times 2$ ,  $2 \times 1$  and dominant  $c4 \times 2$ ] yet retaining a relatively high surface roughness [105]. At about  $900^\circ\text{C}$  well-ordered step-terraces develop and acquire smaller reconstruction unit cells of  $2 \times 2$  and arising from oxygen vacancies  $\sqrt{5} \times \sqrt{5}$ , a behaviour which persists at higher annealing temperatures [105]. Representative constant current topographies after annealing at  $T = 850^\circ\text{C}$  and  $1050^\circ\text{C}$  are shown in Fig. 6.1. (a), (b) and (c) respectively, exhibiting, as mentioned, well-formed terraces and roughness at the atomic scale after annealing to  $T = 850^\circ\text{C}$  and atomically flat terraces with clear  $\sqrt{5} \times \sqrt{5}$  reconstruction after  $1050^\circ$  [105]. The atomic resolution STM image [Fig. 6.1.(c)] of the  $1050^\circ\text{C}$ -annealed surface with  $V_{bias} = 1 \sim \text{eV}$  shows several tetragonal reconstruction domains of three different orientations [106]. It exhibits a variety of structural peculiarities, which appear as either points or extended areas/lines of increased or decreased apparent height. Bright features can be attributed to adatoms on top of the reconstructed ad-layer or oxygen hydroxyl groups resulting from rest gases in the vacuum chamber, as it is known [107] that interstitial Ti atoms can cause a substantial increase in local surface reactivity and thus facilitate O-H group adsorption. Dark features could, on the other hand, indicate missing ad-islands in the  $\sqrt{5} \times \sqrt{5}$  reconstruction [108, 82] or, considering that annealing was carried out at oxygen-poor

conditions, more likely represent oxygen vacancies at or near the surface [109, 105]. In agreement with that, the density of empty states 1eV above the Fermi level, which the STM probes, is high at all sites where a surface O atom is present.

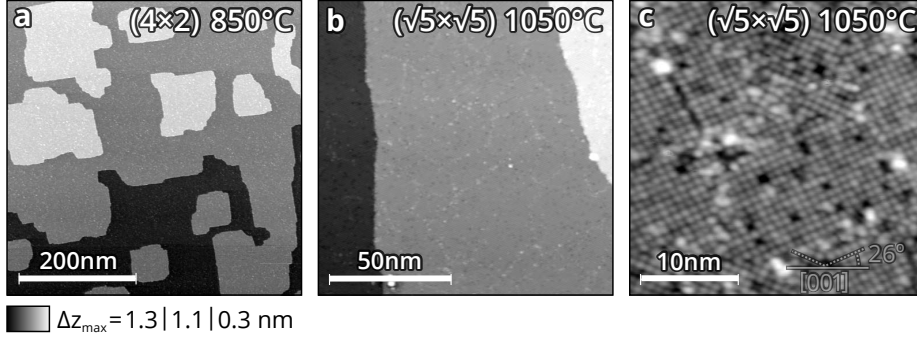


**Figure 6.1:** Overview of the  $c$   $4 \times 2$  reconstructed  $STO(100)$  surface after long term annealing at  $T=850^\circ C$  and  $\sqrt{5} \times \sqrt{5}$ -R 26,6 reconstructed  $STO(100)$  obtained after annealing to  $T=1050^\circ C$  (b,c) [105]. Images are constant current topographies with tunneling parameters  $U_{tip}=2V$ ,  $I=30pA$  (a) and  $U_{tip}=-1V$ ,  $I=10pA$  (b,c). Dark features visible after high temperature annealing (c) are related to oxygen vacancies [109, 105]. The length of the scale bar is 200nm, 50nm and 10nm for (a), (b), (c) images, respectively.

The figure below shows the corresponding STM images as measured by pendulum AFM, also showing the group of oxygen vacancies.

First, we use the scanning tunneling spectroscopy (STS) mode of our AFM to measure at closer tunneling tip-surface distances the  $dI/dV$  spectra above the  $\sqrt{5} \times \sqrt{5}$  reconstructed areas and above the apparent dark spots in STM images. The main difference between the spectra of reduced and non-reduced STO is an additional defect state in the gap  $O_A$  lying at about  $1.2eV$  below the Fermi level, absent for samples annealed at moderate temperatures. Published data [105] attribute a similar STS peak to reduced STO and surface oxygen vacancies, suggesting that the dark STM spots mark vacancies formed in the process of high-temperature annealing. Another feature of the differential conductance spectra of O-vacancy is a weaker peak at about  $0.3eV$  below the Fermi level ( $O_B$ ) in the Figure below. It can be attributed to a shallower in-gap state of the O-vacancy, which, as shown in the recent theoretical study[84] can be gradually emptied by changing the local chemical potential of the surface under the scanning probe tip.

After the topographic characterization of the surface between the annealing cycles, we measure the non-contact frictional dissipation coefficient  $\Gamma$  as a function of the applied tip-sample bias voltage. Measurements are taken with a stiff gold-coated tip oscillating in pendulum geometry at a moderate planar amplitude of  $1nm$  while kept at a constant tip-sample distance of  $15nm$ . Dissipation spectra for samples annealed at  $T = 850^\circ C$  and  $950^\circ C$  are shown in Figure below. Both spectra were taken on flat terraces, far from the step edges. The sample annealed at lower temperature reveals a spectrum which displays a parabolic curve characteristic of Joule non-contact

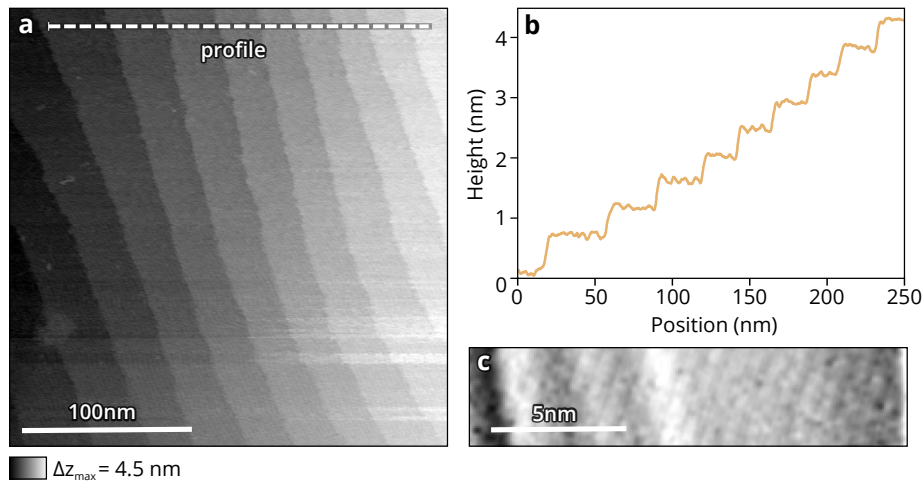


**Figure 6.2:** Constant current STM images of STO surface long-term annealed at  $T = 950^\circ\text{C}$  taken with a metallic tip in pendulum geometry. The tunneling parameters were  $U_{tip} = -1.5\text{V}$ ,  $I = 100\text{pA}$  and  $U_{tip} = -0.55\text{V}$ ,  $I = 30\text{pA}$  for (a) and (c), respectively. The length of the scale bar is equal to  $100\text{nm}$  and  $5\text{nm}$  on (a) and (c), respectively. Height profile (b) shows that the surface is composed of atomically flat terraces of average width about  $25\text{nm}$ . Dark features visible on (c) are presumed to be oxygen vacancies. Note that already after annealing to  $950^\circ\text{C}$  samples are morphologically close to that shown by tuning fork.

friction [65]. Similarity with Nb metal above  $T_C$  [4] indicates some ohmic electron conduction in the STO surface. The dissipation spectrum of the  $950^\circ\text{C}$  annealed sample, however, exhibits, in addition, two distinct dissipation peaks at  $V = V_{CP} \pm 3.25\text{V}$  located symmetrically around the contact potential voltage  $V_{CP} = -0.7\text{V}$  and a broader, less pronounced dissipation peak around  $4.2\text{V}$  as shown in the figure below.

### 6.3 Local and non-local dissipation

Key clues that clarify the tip-induced O-vacancy transition mechanism are provided by the dependence of the dissipation behavior on the tip-sample distance  $z$ . For distances spanning a range from near-contact regime to  $15\text{nm}$ , we measure the bias ( $V$ ) dependence of the AFM frictional dissipation coefficient  $\Gamma$ , thus obtaining a full  $\Gamma(V, d)$  map. We use two different tips in pendulum geometry: (i) a stiffer gold-coated cantilever tip with a moderately low stiffness of  $50\text{N/m}$  operated at a nominal amplitude of  $A = 1\text{nm}$  and (ii) an ultra-sensitive probe with very low stiffness of ( $0.1\text{N/m}$ ) which implies larger oscillation amplitudes of up to  $5\text{nm}$ . Unlike the stiff cantilever, the soft sensor is not gold-coated, which results in a very high value of  $Q$  but requires significant doping of the silicon tips for attaining reasonable conducting properties.

The stiff tip dissipation map taken above a reconstructed section of the  $\text{Sr}_2\text{TiO}_3$  surface is shown in Figure 6.5 (a). It shows features found in other similar experi-

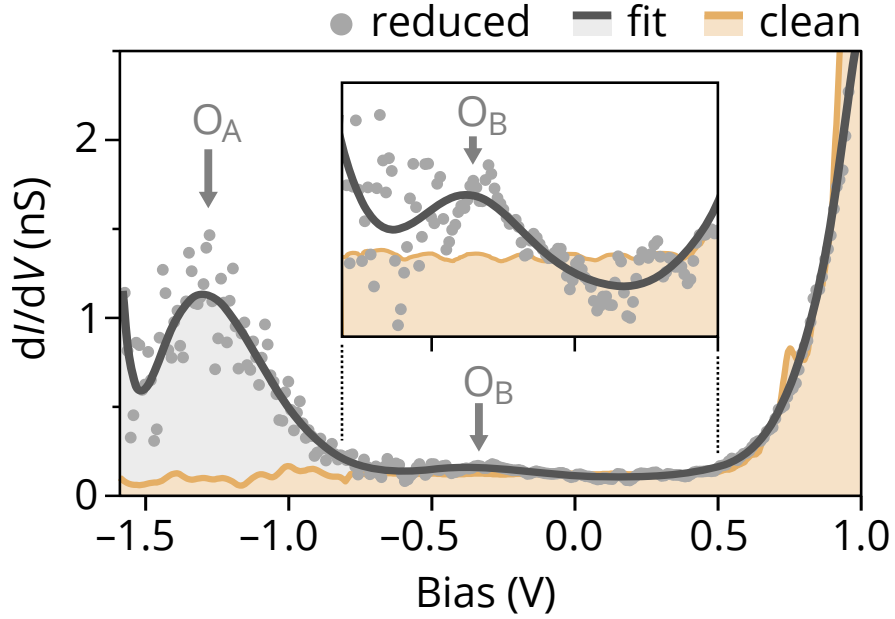


**Figure 6.3:** The  $dI/dV$  spectrum of the reduced surface is characterised by the presence of a broad peak localized at about  $1.2\text{eV}$  below the Fermi level  $O_A$ , a signature of an oxygen deficient system [105]. A smaller peak  $O_B$  just below the Fermi level (see inset) can also be attributed to oxygen impurity levels. For comparison, the spectrum for non-reduced sample is shown in beige (light brown).

ments [4]. For each tip-sample distance, the friction coefficient exhibits a parabolic behavior, which is a cross-section of the map in Figure 6.4 (a) at  $d = 15\text{nm}$  and a hallmark of Joule-loss non-contact friction [65, 4]. The map is near-symmetric with respect to the contact potential difference (CPD) voltage marked in the plot. The outer hull of the dissipation map is defined by the critical bias voltage for excitation of electrons over the band gap of the STO signaling a sharp increase in dissipation (about  $\pm 2.5\text{V}$ ) at close range. The sharp dissipation peaks at the sub-bandgap voltages marked with arrows both reach  $\Gamma = 5 \cdot 10^{-10}\text{kg/s}$ , maintaining roughly the same intensity independently of the tip-sample distance. The peaks are observed at non-zero (with respect to CPD) biases even at close range and shift towards higher bias voltages with increasing tip-sample distance, which indicates that the effect is voltage rather than force controlled, similar to the case of quantum dots [33] and in analogy to quantum dots the amount of dissipated energy given by different sensors is also in the order of  $10\text{-}20\text{ meV/cycle}$ . To further investigate the dissipation mechanism, we repeat the dissipation measurements with an ultra-sensitive doped-silicon sensor. Very low stiffness ( $k = 0.1\text{N/m}$ ) of the sensor implies larger horizontal oscillation amplitudes of up to  $5\text{ nm}$  and the absence of metal coating might imply different interaction behavior. The non-contact friction dependence map  $\Gamma(V, d)$  taken with a soft tip is shown in Figure 6.5 (b). Here again bright features correspond to the high dissipation maxima up to  $\Gamma = 2 \cdot 10^{-10}\text{kg/s}$ . However, instead of just two dissipation peaks, the soft non-local sensor sports a whole family of dissipation maxima. We noticed a sub-

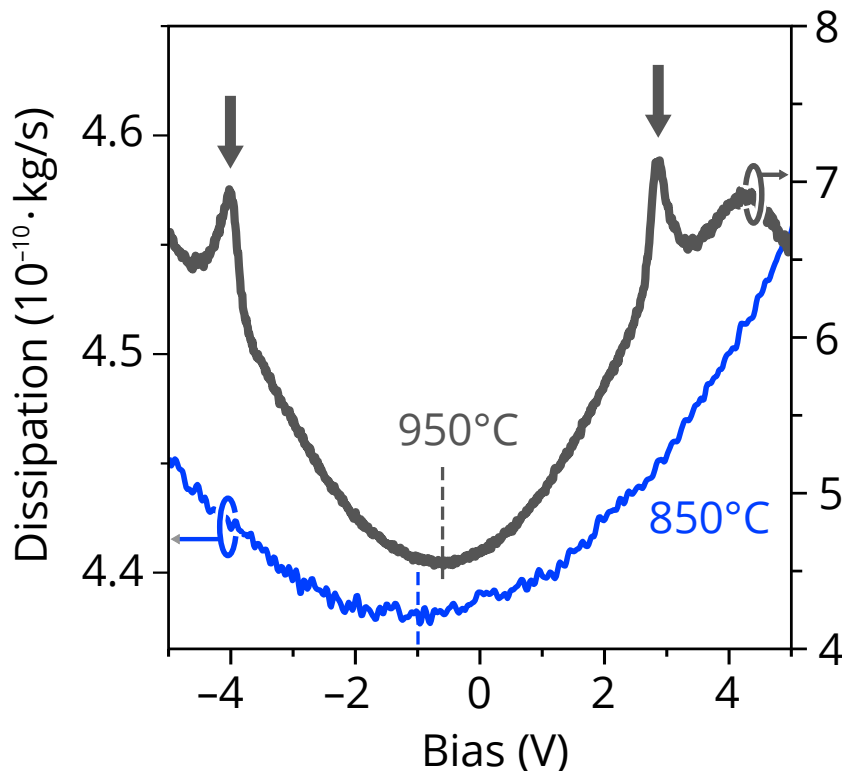


**Figure 6.4:** Bias voltage dependence of friction coefficient  $\Gamma$  between the metallic tip oscillating with amplitude  $A = 1 \text{ nm}$  and  $\text{Sr}_2\text{TiO}_3(100)$  sample annealed at two different temperatures of  $850^\circ\text{C}$  (black) and  $950^\circ\text{C}$  (blue). Higher annealing temperatures (characterised by  $\sqrt{5} \times \sqrt{5}$  reconstruction) lead to larger dissipation and pronounced dissipation peaks marked by arrows. Additional grey axis on the left and pale-blue axis on the right give corresponding per-cycle energy dissipation values  $P[\text{eV}/\text{cycle}]$ .

stantial change of CPD value ( $\Delta\text{CPD} = 0.1\text{V}$ ) indicated by the elbow shape of the arrow in the transition while switching from one to the next dissipation maxima trace. It is consistent with the idea of the oscillating tip, causing a persistent accumulation of charge below it and further corroborates the guess that the charging dissipation scenario is responsible for the dissipation peaks. These again prove the electronic nature of energy dissipation in analogy to quantum dots [33, 110].

## 6.4 Discussion

The dissipation peak phenomenology fits a model of charge and spin state transitions in oxygen vacancies present at reduced STO surfaces, as follows. The distant pendulum tip projects a potential shadow on the underlying  $\text{Sr}_2\text{TiO}_3(001)$  surface deforming the local electronic chemical potential (either directly or indirectly by distorting the surface atom positions). This perturbation is larger for a charged tip, but even at zero voltage, the van der Waals polarization interaction shifts the chemical potential by modifying



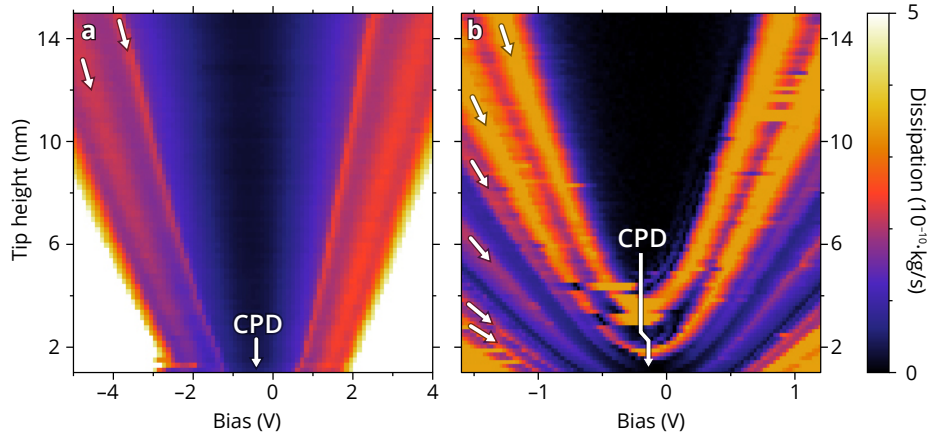


**Figure 6.5:** Local and non-local bias voltage  $V$  and tip-sample distance  $d$  resolved dissipation maps  $\Gamma(V, d)$ . The dissipation maps were taken with two different AFM tips suspended in pendulum geometry: (a) the stiff gold-coated cantilever tip with a moderately low stiffness of  $50\text{N/m}$  driven at a moderate nominal amplitude of  $1\text{nm}$  and (b) an ultra-sensitive probe with very low stiffness of  $(0.1\text{N/m})$  driven at oscillation amplitudes of up to  $5\text{nm}$ .

the electron self-energy. If one or more oxygen vacancies happen to lie in the potential shadow of the tip (see Figure below for a sketch) the vacancies closer to the tip's position experience a different electron chemical potential than those at the periphery. At certain values of the imposed potential (the strength/depth of which is dependent on the tip-sample distance and mutual bias), the topmost filled impurity level of one of the O-vacancy can become aligned with an empty electron reservoir thus provoking one electron to leave the vacancy, causing a transition [84]. Electrons can be exchanged between a neutral vacancy and a charged one, or a vacancy and the conduction band of the surrounding STO surface as well as the 2DEG known to exist on the doped interfaces of STO [90, 75]. Oxygen vacancies on STO surfaces are known to exist as both isolated entities or as cluster defects. The latter can exhibit multiple impurity levels and reside in a number of charge states [84]. Alignment of one or several impurity levels of such an extended vacancy with either a single-vacancy impurity level or the STO electron bath can lead to one or several consecutive electron transitions, taking place by resonant tunneling or generally by electron transfer. An oscillating AFM tip at a fixed bias can cause, when it reaches the right distance, a sufficient deformation of the local chemical potential to provoke one of these transitions, which is reversed as the tip oscillates back. Every single electron transfer channel leading to a transition can manifest itself as AFM tip dissipation peaking precisely when the bias voltage and distance first reach the values required to activate the transfer. The approximately symmetric pattern for positive and negative tip voltage suggests that this mechanism is reversible.

In the dissipation measurements carried out with the stiffer gold-coated tip, the area swept is much smaller, and the two observed dissipation peaks can originate from the single and double discharging of a standalone vacancy with electrons being transferred

to either other vacancies/vacancy clusters or to the STO conduction band. We estimate the average distance between the dark defects on our sample from STM images to be  $3.7 \text{ nm}$   $1.6 \sim \text{nm}$ . Thus a stiff tip swinging with an amplitude of  $1 \sim \text{nm}$  is unlikely to impact more than one vacancy, even considering that the characteristic dimensions of the perturbation caused by the tip suspended at several nm distances shall be larger than the amplitude of its swing. The softer non-local tip swinging at an amplitude of  $5 \text{ nm}$  will, on the contrary, enclose in its potential shadow path several O-vacancies or a vacancy cluster resulting in more electron transition channels and consequently more dissipation peaks. The fact that in the latter case some dissipation peaks exist even in the case when the CPD is completely compensated is a likely residual effect of the van der Waals interaction, as the O-vacancy impurity level is a relatively shallow one and does not require much perturbation to be emptied. This assumption is especially important to us since vacancy charge states were shown to be stable with respect to mechanical perturbations of the system [84] thus making the influence of the tip on the observed charge and spin-state transition much more likely to be electronic than mechanical in origin. Unfortunately, we cannot specify exactly what levels we are precisely talking about. Comparison of our STS data with DFT calculations[84] suggests that for a single vacancy charging scenario, the observed dissipation might arise from the transitions between  $q=-2e$  and  $q=-1e$  charge states. Interestingly, that should also involve a spin transition, from  $S = 1/2$  of the  $q=-1e$  state, to  $S = 0$  in the  $q=-2e$  state, where the two electrons in the two Ti oppositely facing dangling bonds couple antiferromagnetically.[84].

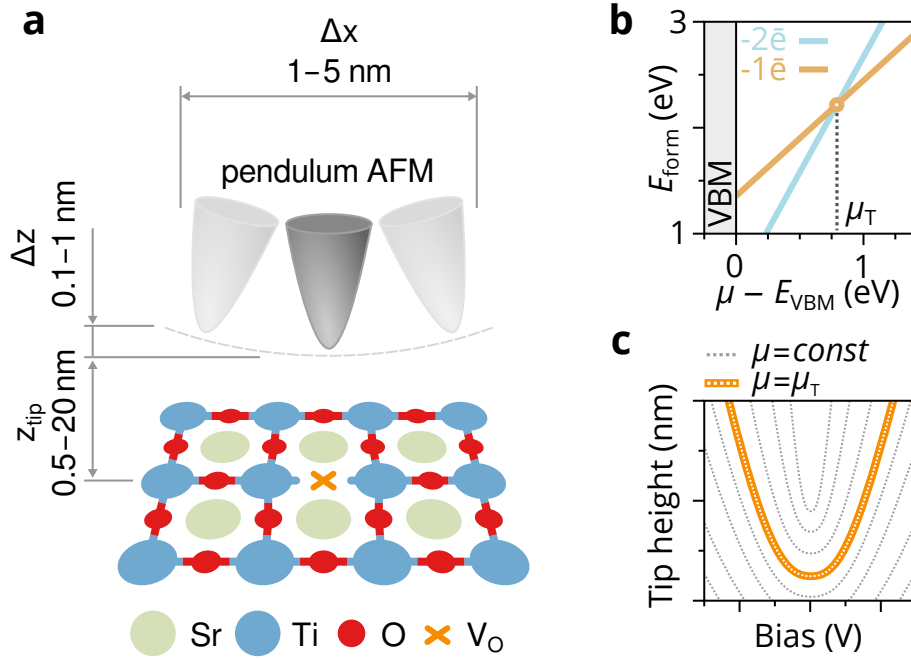


**Figure 6.6:** *Pendulum AFM as a characterization tool for oxygen vacancies on STO. (a) A sketch of the setup: pendulum AFM tip oscillating over an oxygen vacancy on the  $\text{TiO}_2$ -terminated surface of strontium titanate. The vacancy is characterised by two dangling Ti-bonds left behind by the departing oxygen atom which then trap the two electrons also left behind by the oxygen. The system acts as a quantum dot with the two additional electrons giving each Ti a local magnetic moment of  $1\sim$ . The pendulum AFM tip suspended above the surface at a range of heights starting from 0.5nm and swinging with a lateral amplitude of 1 – 5nm and vertical amplitude of less than 1nm can overshadow one or several vacancies (depending on the lateral amplitude). On (b) Formation energy diagram for different charge states of a single oxygen vacancy at the TiO-terminated  $\text{Sr}_2\text{TiO}_3(001)$  surface as a function of the chemical potential  $\mu$  imposed by the AFM tip (relative to the valence band maximum). (c) The sketch is explaining the observed dissipation parabolas. In the AFM-tip height-bias space lines of constant exerted chemical potential form slightly distorted parabolas. If the chemical potential exerted by the AFM tip coincides with the transition potential for an oxygen vacancy, periodic vacancies charge and spin state transitions present a dissipation channel for the AFM pendulum oscillation energy, resulting in a dissipation peak as seen on the dissipation maps.*



---

## Conclusion

THE main question that was asked at the beginning of my study was "How does the electronic structure effects the non-contact energy dissipation?". During my study, I tried to answer this question by performing experiments and understanding the theoretical explanations for the results. To be able to answer such a question, improvements in the experimental setup was done. The main purpose was to be able to combine two different scanning microscopy techniques namely AFM and STM. The STM cables were changed with shielded ones and optimization was done to achieve the best signal to noise ratio. While pendulum AFM was used for understanding the energy dissipation on layered materials, STM was used to understand the electronic nature of them. Using these two techniques and combining them, allow me to study: HOPG, 1T-TaS<sub>2</sub>, Bi<sub>2</sub>Te<sub>3</sub>, and SrTiO<sub>3</sub> surfaces to understand different dissipation mechanisms.

Force and dissipation spectroscopies were performed on HOPG. Experimental results indicate that Joule dissipation lacks or negligible on a clean HOPG surface. Lack of Joule dissipation is due to the weak electron-phonon coupling and thus long electron means free path where there is no defect.

After HOPG, 1T-TaS<sub>2</sub> was studied with STM and AFM. 1T-TaS<sub>2</sub> have different charge density waves (CDW) on the surface. Measurements were made at different temperatures; 5K, 77K, and room temperature. The structure of charge density waves was measured successfully with STM. Scanning tunneling spectroscopy (STS) measurements showed the increase of the bandgap when the system is cooled down to the Mott insulating phase. Low-temperature dissipation spectroscopy data indicate that the main dissipation mechanism on 1T-TaS<sub>2</sub> is the Joule dissipation mechanism due to Mott transition and strongly pinned commensurate charge density wave phase. However, at room temperature, Joule dissipation is suppressed due to the increased disorder in the system when the charge density wave is in a nearly commensurate phase. Hence, van der Waals friction was measured as the main dissipation mechanism. Origin of van der Waals friction was studied further by performing frequency shift noise measurements. The measurement strongly indicates that van der Waals

friction is due to the random motion of the weakly pinned charge density wave.

$\text{Bi}_2\text{Te}_3$ , have a topologically protected surface state and it lacks Joule dissipation. The sample was studied by means of STM/STS, pendulum AFM and combined pendulum AFM/STM. Dirac cone, a hint for the existence of a topologically protected surface state, was measured with STS. Image potential states were measured for the first time on a topological insulator surface using  $z(\text{V})$  spectroscopy. On the same system, dissipation spectroscopies were performed and dissipation peaks were measured. Pendulum AFM/STM combined measurements were performed by using STM feedback with an oscillating tip. Dissipation data during the  $z(\text{V})$  spectroscopy was collected successfully and opened up a window to understand the effect of image potential states into energy dissipation. This combined measurement showed that the dissipation is strongly related to the image potential states and the main mechanism is the charge fluctuation when tip populated the image potential states in the single electron tunneling process. Results show that Joule dissipation is negligible in  $\text{Bi}_2\text{Te}_3$  so that it is possible to probe the dissipation due to charge fluctuation. Furthermore, magnetic field measurements show that it is possible to break down the topologically protected surface state which is seen in dissipation spectroscopy as a rise of Joule type of losses.

Both  $\text{TaS}_2$  and  $\text{Bi}_2\text{Te}_3$  are layered materials but they are different from HOPG since they hold a dissipative system (CDW and IPS) that oscillating tip might perturb or interact with. To combine the electronic properties with the dissipation, STM and AFM experiments were performed simultaneously. Performing STM-AFM combined measurements were only possible after the improvement of the STM line of the system. The results show that having a metallic tip also improved the dissipation measurements.

Finally I reported on striking singlets or multiplets of dissipation peaks above  $\text{SrTiO}_3$  surface present at low temperatures ( $T=5\text{K}$ ) and after sample annealing to high temperatures ( $T > 1000^\circ\text{C}$ ) which leads to oxygen deficient sample. The observed dissipation peaks are attributed to tip-induced charge state transitions in quantum-dot-like entities formed by single oxygen vacancies (and clusters thereof) at the  $\text{SrTiO}_3$  surface. This in view of technological and fundamental research relevance of the material opens important avenues for further studies and applications.

---

## Bibliography

- [1] E. Gnecco and E. Meyer, *Fundamentals of friction and wear on the nanoscale* (Springer-Verlag, 2007).
- [2] M. Kisiel, M. Samadashvili, U. Gysin, and E. Meyer, *Non-contact Friction* (Springer International Publishing, Cham, 2015), pp. 93–110.
- [3] B. Gotsmann, C. Seidel, B. Anczykowski, and H. Fuchs, *Physical Review B* **60**, 11051 (1999), ISSN 0163-1829.
- [4] M. Kisiel, E. Gnecco, U. Gysin, L. Marot, S. Rast, and E. Meyer, *Nature Materials* **10**, 119 EP (2011).
- [5] M. Langer, M. Kisiel, R. Pawlak, F. Pellegrini, G. E. Santoro, R. Buzio, A. Gerbi, G. Balakrishnan, A. Baratoff, E. Tosatti, et al., *Nature Materials* **13**, 173 (2014).
- [6] A. I. Volokitin and B. N. Persson, *Reviews of Modern Physics* **79**, 1291 (2007).
- [7] M. Kisiel, F. Pellegrini, G. E. Santoro, M. Samadashvili, R. Pawlak, A. Benassi, U. Gysin, R. Buzio, A. Gerbi, E. Meyer, et al., *Phys. Rev. Lett.* **115**, 046101 (2015).
- [8] G. Binnig, C. F. Quate, and C. Gerber, *Phys. Rev. Lett.* **56**, 930 (1986).
- [9] D. Sarid, *Scanning Force Microscopy: With Applications to Electric, Magnetic, and Atomic Forces*, Oxford Series in Optical and Imaging Sciences (Oxford University Press, 1994), ISBN 9780195344691.
- [10] H. D. Young, R. A. Freedman, , and A. L. Ford, *University physics with modern physics* (Pearson, 2007).
- [11] D. Halbertal, M. B. Shalom, A. Uri, K. Bagani, A. Y. Meltzer, I. Marcus, Y. Myasoedov, J. Birkbeck, L. S. Levitov, A. K. Geim, et al., *Science* **358**, 1303 (2017).
- [12] R. Kubo, *Reports on Progress in Physics* **29**, 255 (1966).
- [13] U. Gysin, S. Rast, M. Kisiel, C. Werle, and E. Meyer, *Review of Scientific Instruments* **82** (2011).
- [14] R. Sandberg, K. Mølhave, A. Boisen, and W. Svendsen, *Journal of Micromechanics and Microengineering* **15**, 2249 (2005).
- [15] S. Rast, U. Gysin, and E. Meyer, *Physical Review B* **79**, 054106 (2009).

## Bibliography

---

- [16] A. Labuda, J. R. Bates, and P. H. Grütter, *Nanotechnology* **23** (2012).
- [17] G. Binnig, H. Rohrer, C. Gerber, and E. Weibel, *Applied Physics Letters* **40**, 178 (1982).
- [18] G. Binnig and H. Rohrer, *Rev. Mod. Phys.* **59**, 615 (1987).
- [19] K. S. Novoselov, A. K. Geim, S. V. Morozov, D. Jiang, Y. Zhang, S. V. Dubonos, I. V. Grigorieva, and A. A. Firsov, *Science* **306**, 666 (2004).
- [20] A. I. Volokitin, *Zeitschrift fur Naturforschung - Section A Journal of Physical Sciences* **72**, 171 (2017).
- [21] D. Yıldız and O. Gürlü, *Materials Today Communications* **8**, 72 (2016).
- [22] S. Bose, V. M. Silkin, R. Ohmann, I. Brihuega, L. Vitali, C. H. Michaelis, P. Mallet, J. Y. Veuillen, M. Alexander Schneider, E. V. Chulkov, et al., *New Journal of Physics* **12** (2010), ISSN 13672630.
- [23] L. Perfetti, P. A. Loukakos, M. Lisowski, U. Bovensiepen, H. Berger, S. Biermann, P. S. Cornaglia, A. Georges, and M. Wolf, *Physical Review Letters* **97**, 67402 (2006).
- [24] W. Wonneberger and H.-J. Breymayer, *Z. Phys. B - Condensed Matter* **43**, 31 (1991).
- [25] R. Heid, *The Physics of Correlated Insulators, Metals and Superconductors* **7**, 12 (2017).
- [26] G. Grüner, *Reviews of Modern Physics* **60**, 1129 (1988).
- [27] B. Sipos, A. F. Kusmartseva, A. Akrap, H. Berger, L. Forro, and E. Tuti, *Nature materials* **7** **12**, 960 (2008).
- [28] K. T. Law and P. A. Lee, *Proceedings of the National Academy of Sciences* **114**, 6996 (2017).
- [29] E. Tosatti and P. Fazekas, *JOURNAL DE PHYSIQUE* **37**, C4 (1976).
- [30] J. A. Wilson, F. J. Di Salvo, and S. Mahajan, *Advances in Physics* **24**, 117 (1975).
- [31] J. J. Kim, W. Yamaguchi, T. Hasegawa, and K. Kitazawa, *Physical Review Letters* **73**, 2103 (1994).
- [32] L. Ma, C. Ye, Y. Yu, X. F. Lu, X. Niu, S. Kim, D. Feng, D. Tománek, Y. W. Son, X. H. Chen, et al., *Nature Communications* **7**, 1 (2016).
- [33] L. Cockins, Y. Miyahara, S. D. Bennett, A. A. Clerk, S. Studenikin, P. Poole, A. Sachrajda, and P. Grutter, *Proceedings of the National Academy of Sciences* **107**, 9496 (2010).
- [34] G. Liu, S. Rumyantsev, M. A. Bloodgood, T. T. Salguero, and A. A. Balandin, *Nano Letters* **18**, 3630 (2018).
- [35] Y. L. Chen, J. G. Analytis, J.-H. Chu, Z. K. Liu, S.-K. Mo, X. L. Qi, H. J. Zhang, D. H. Lu, X. Dai, Z. Fang, et al., *Science* **325**, 178 (2009).



- 
- [36] M. Z. Hasan and C. L. Kane, *Rev. Mod. Phys.* **82**, 3045 (2010).
- [37] J. Seo, P. Roushan, H. Beidenkopf, Y. S. Hor, R. J. Cava, and A. Yazdani, *Nature* **466**, 343 EP (2010).
- [38] T. Zhang, P. Cheng, X. Chen, J.-F. Jia, X. Ma, K. He, L. Wang, H. Zhang, X. Dai, Z. Fang, et al., *Phys. Rev. Lett.* **103**, 266803 (2009).
- [39] H.-T. He, G. Wang, T. Zhang, I.-K. Sou, G. K. L. Wong, J.-N. Wang, H.-Z. Lu, S.-Q. Shen, and F.-C. Zhang, *Phys. Rev. Lett.* **106**, 166805 (2011).
- [40] D. Straub and F. J. Himpsel, *Phys. Rev. B* **33**, 2256 (1986).
- [41] V. Dose, *Physica Scripta* **36**, 669 (1987).
- [42] P. Echenique and M. Uranga, *Surface Science* **247**, 125 (1991), ISSN 0039-6028.
- [43] W. Berthold, U. Höfer, P. Feulner, E. V. Chulkov, V. M. Silkin, and P. M. Echenique, *Phys. Rev. Lett.* **88**, 056805 (2002).
- [44] P. Wahl, M. A. Schneider, L. Diekhöner, R. Vogelgesang, and K. Kern, *Phys. Rev. Lett.* **91**, 106802 (2003).
- [45] K. Schouteden and C. Van Haesendonck, *Phys. Rev. Lett.* **103**, 266805 (2009).
- [46] D. Niesner and T. Fauster, *Journal of Physics: Condensed Matter* **26**, 393001 (2014).
- [47] J. A. Sobota, S. Yang, J. G. Analytis, Y. L. Chen, I. R. Fisher, P. S. Kirchmann, and Z.-X. Shen, *Phys. Rev. Lett.* **108**, 117403 (2012).
- [48] J. A. Sobota, S.-L. Yang, A. F. Kemper, J. J. Lee, F. T. Schmitt, W. Li, R. G. Moore, J. G. Analytis, I. R. Fisher, P. S. Kirchmann, et al., *Phys. Rev. Lett.* **111**, 136802 (2013).
- [49] D. Niesner, T. Fauster, S. V. Eremeev, T. V. Menshchikova, Y. M. Koroteev, A. P. Protogenov, E. V. Chulkov, O. E. Tereshchenko, K. A. Kokh, O. Alekperov, et al., *Phys. Rev. B* **86**, 205403 (2012).
- [50] D. Niesner, S. Otto, T. Fauster, E. Chulkov, S. Eremeev, O. Tereshchenko, and K. Kokh, *Journal of Electron Spectroscopy and Related Phenomena* **195**, 258 (2014), ISSN 0368-2048.
- [51] E. V. Chulkov, I. Sarría, M. V. Silkin, J. M. Pitarke, and P. M. Echenique, *Physical Review Letters* (1998).
- [52] K. H. Gundlach, *Solid-State Electronics* **9**, 949 (1966).
- [53] U. Höfer, I. L. Shumay, C. Reuß, U. Thomann, W. Wallauer, and T. Fauster, *Science* **277**, 1480 (1997), ISSN 00368075.
- [54] B. C. Stipe, H. J. Mamin, T. D. Stowe, T. W. Kenny, and D. Rugar, *Phys. Rev. Lett.* **87**, 096801 (2001).

## Bibliography

---

- [55] W.-B. Su, C.-L. Lin, W.-Y. Chan, S.-M. Lu, and C.-S. Chang, *Nanotechnology* **27**, 175705 (2016).
- [56] M. Hajlaoui, E. Papalazarou, J. Mauchain, G. Lantz, N. Moisan, D. Boschetto, Z. Jiang, I. Miotkowski, Y. P. Chen, A. Taleb-Ibrahimi, et al., *Nano Letters* **12**, 3532 (2012).
- [57] M. Neupane, S.-Y. Xu, L. A. Wray, A. Petersen, R. Shankar, N. Alidoust, C. Liu, A. Fedorov, H. Ji, J. M. Allred, et al., *Phys. Rev. B* **85**, 235406 (2012).
- [58] K. Miyamoto, A. Kimura, T. Okuda, H. Miyahara, K. Kuroda, H. Namatame, M. Taniguchi, S. V. Eremeev, T. V. Menshchikova, E. V. Chulkov, et al., *Phys. Rev. Lett.* **109**, 166802 (2012).
- [59] K. Schouteden, Z. Li, T. Chen, F. Song, B. Partoens, C. Van Haesendonck, and K. Park, *Scientific Reports* **6**, 20278 EP (2016), article.
- [60] D. Niesner, S. Otto, V. Hermann, T. Fauster, T. V. Menshchikova, S. V. Eremeev, Z. S. Aliev, I. R. Amiraslanov, M. B. Babanly, P. M. Echenique, et al., *Phys. Rev. B* **89**, 081404 (2014).
- [61] M. Pivetta, F. Patthey, M. Stengel, A. Baldereschi, and W. D. Schneider, *Physical Review B - Condensed Matter and Materials Physics* **72**, 1 (2005), ISSN 10980121.
- [62] M. F. Crommie, C. P. Lutz, and D. M. Eigler, *Science* **262**, 218 (1993), ISSN 0036-8075.
- [63] ed. Enrico Gnecco and E. Meyer, *Fundamentals of Friction and Wear on the Nanoscale* (Springer, 2015).
- [64] ed. Seizo Morita, F. J. Giessibl, E. Meyer, and R. Wiesendanger, *Noncontact Atomic Force Microscopy* (Springer, 2015).
- [65] A. I. Volokitin, B. N. J. Persson, and H. Ueba, *Physical Review B* **73**, 165423 (2006).
- [66] M. Kisiel, O. O. Brovko, D. Yildiz, R. Pawlak, U. Gysin, E. Tosatti, and E. Meyer, *Nature Communications* **9**, 2946 (2018), ISSN 2041-1723.
- [67] R. Stomp, Y. Miyahara, S. Schaer, Q. Sun, H. Guo, P. Grutter, S. Studenikin, P. Poole, and A. Sachrajda, *Phys. Rev. Lett.* **94**, 056802 (2005).
- [68] M. Paulsson, F. Zahid, and D. S., *Resistance of a Molecule*, Oxford Series in Optical and Imaging Sciences (CRC Press, 2002), ISBN 9780195344691.
- [69] P. Sessi, F. Reis, T. Bathon, K. A. Kokh, O. E. Tereshchenko, and M. Bode, *Nature Communications* **5**, 5349 EP (2014), article.
- [70] J. L. Olsen, *Electron transport in metals* (Interscience, 1962).
- [71] S. Fatayer, N. Moll, S. Collazos, D. Pérez, E. Guitián, D. Peña, L. Gross, and G. Meyer, *Physical Review Letters* **121**, 1 (2018).
- [72] J. B. Goodenough, *Reports on Progress in Physics* **67**, 1915 (2004).

- [73] M. S. J. Marshall, A. E. Becerra-Toledo, L. D. Marks, and M. R. Castell, in *Springer Series in Surface Sciences*, edited by J. Jupille and T. Geoff (Springer International Publishing, Switzerland, 2015), vol. 58, pp. 327–349, ISBN 978-3-319-14367-5.
- [74] H. Ohta, S. Kim, Y. Mune, T. Mizoguchi, K. Nomura, S. Ohta, T. Nomura, Y. Nakanishi, Y. Ikuhara, M. Hirano, et al., *Nature Materials* **6**, 129 (2007).
- [75] A. F. Santander-Syro, F. Fortuna, C. Bareille, T. C. Rödel, G. Landolt, N. C. Plumb, J. H. Dil, and M. Radović, *Nature materials* **13**, 1085 (2014).
- [76] T. Taniuchi, Y. Motoyui, K. Morozumi, T. C. Rödel, F. Fortuna, A. F. Santander-Syro, and S. Shin, *Nature Communications* **7**, 11781 (2016).
- [77] K. A. Müller, W. Berlinger, and E. Tosatti, *Zeitschrift für Physik B Condensed Matter* **84**, 277 (1991).
- [78] M. Salluzzo, S. Gariglio, D. Stornaiuolo, V. Sessi, S. Rusponi, C. Piamonteze, G. M. De Luca, M. Minola, D. Marré, A. Gadaleta, et al., *Physical Review Letters* **111**, 087204 (2013).
- [79] Z. Q. Liu, W. M. Lü, S. L. Lim, X. P. Qiu, N. N. Bao, M. Motapohtula, J. B. Yi, M. Yang, S. Dhar, T. Venkatesan, et al., *Physical Review B* **87**, 220405 (2013).
- [80] N. Shanthi and D. D. Sarma, *Physical Review B* **57**, 2153 (1998).
- [81] Y.-H. Lin, Y. Chen, and A. M. Goldman, *Physical Review B* **82**, 172507 (2010).
- [82] Y. Lin, A. E. Becerra-Toledo, F. Silly, K. R. Poeppelmeier, M. R. Castell, and L. D. Marks, *Surface Science* **605**, L51 (2011).
- [83] W. D. Rice, P. Ambwani, M. Bombeck, J. D. Thompson, G. Haugstad, C. Leighton, and S. A. Crooker, *Nature Materials* **13**, 481 (2014).
- [84] O. O. Brovko and E. Tosatti, *Physical Review Materials* **1**, 044405 (2017).
- [85] M. Janousch, G. I. Meijer, U. Staub, B. Delley, S. F. Karg, and B. P. Andreasson, *Advanced Materials* **19**, 2232 (2007).
- [86] J.-W. Chang, J. S. Lee, T. H. Lee, J. Kim, and Y.-j. Doh, *Applied Physics Express* **8**, 055701 (2015).
- [87] S. S. Rao, Y. F. Lee, J. T. Prater, A. I. Smirnov, and J. Narayan, *Applied Physics Letters* **105**, 042403 (2014).
- [88] W. Meevasana, P. D. C. King, R. H. He, S.-K. Mo, M. Hashimoto, A. Tamai, P. Songriritthigul, F. Baumberger, and Z.-X. Shen, *Nature Materials* **10**, 114 (2011).
- [89] N. C. Plumb, M. Salluzzo, E. Razzoli, M. Månsson, M. Falub, J. Krempasky, C. E. Matt, J. Chang, M. Schulte, J. Braun, et al., *Physical Review Letters* **113**, 086801 (2014).
- [90] A. F. Santander-Syro, O. Copie, T. Kondo, F. Fortuna, S. Pailhès, R. Weht, X. G. Qiu, F. Bertran, A. Nicolaou, A. Taleb-Ibrahimi, et al., *Nature* **469**, 189 (2011).

## Bibliography

---

- [91] R. Di Capua, M. Radovic, G. M. De Luca, I. Maggio-Aprile, F. Miletto Granozio, N. C. Plumb, Z. Ristic, U. Scotti di Uccio, R. Vaglio, and M. Salluzzo, *Physical Review B* **86**, 155425 (2012).
- [92] C. Lin and A. A. Demkov, *Physical Review Letters* **111**, 217601 (2013).
- [93] Y. Zhang, J. Wang, M. Sahoo, T. Shimada, and T. Kitamura, *Phys. Chem. Chem. Phys.* **17**, 27136 (2015).
- [94] D. D. Cuong, B. Lee, K. M. Choi, H.-S. Ahn, S. Han, and J. Lee, *Physical Review Letters* **98**, 115503 (2007).
- [95] V. E. Alexandrov, E. A. Kotomin, J. Maier, and R. A. Evarestov, *The European Physical Journal B* **72**, 53 (2009).
- [96] M. Choi, F. Oba, Y. Kumagai, and I. Tanaka, *Advanced Materials* **25**, 86 (2013).
- [97] N. Pavlenko and T. Kopp, *Journal of Superconductivity and Novel Magnetism* **26**, 1175 (2013).
- [98] A. Lopez-Bezanilla, P. Ganesh, and P. B. Littlewood, *Physical Review B* **92**, 115112 (2015).
- [99] Y.-L. Li, D.-N. Zhang, S.-B. Qu, M. Yang, and Y.-P. Feng, *Surface Science* **641**, 37 (2015).
- [100] M. Altmeyer, H. O. Jeschke, O. Hijano-Cubelos, C. Martins, F. Lechermann, K. Koepernik, A. F. Santander-Syro, M. J. Rozenberg, R. Valentí, and M. Gabay, *Physical Review Letters* **116**, 157203 (2016).
- [101] A. C. Garcia-Castro, M. G. Vergniory, E. Bousquet, and A. H. Romero, *Physical Review B* **93**, 045405 (2016).
- [102] X.-X. Liao, H.-Q. Wang, and J.-C. Zheng, *Journal of the American Ceramic Society* **96**, 538 (2012).
- [103] W. D. Rice, P. Ambwani, J. D. Thompson, C. Leighton, and S. A. Crooker, *Journal of Vacuum Science & Technology B: Microelectronics and Nanometer Structures* **32**, 04E102 (2014).
- [104] H. Trabelsi, M. Bejar, E. Dhahri, M. Sajieddine, M. A. Valente, and A. Zaoui, *Journal of Alloys and Compounds* **680**, 560 (2016).
- [105] H. Tanaka, T. Matsumoto, T. Kawai, and S. Kawai, *Japanese Journal of Applied Physics* **32**, 1405 (1993).
- [106] V. V. Lemanov, S. A. Gridnev, and E. V. Ukhin, *Physics of the Solid State* **44**, 1156 (2002).
- [107] S. Wendt, P. T. Sprunger, E. Lira, G. K. H. Madsen, Z. Li, J. O. Hansen, J. Matthiesen, A. Blekinge-Rasmussen, E. Laegsgaard, B. Hammer, et al., *Science* **320**, 1755 (2008).

- [108] S. Shiraki, M. Nantoh, S. Katano, and M. Kawai, *Applied Physics Letters* **96**, 231901 (2010).
- [109] M. Setvín, M. Wagner, M. Schmid, G. S. Parkinson, and U. Diebold, *Chem. Soc. Rev.* **46**, 1772 (2017).
- [110] L. Cockins, Y. Miyahara, S. D. Bennett, A. A. Clerk, and P. Grutter, *Nano Letters* **12**, 709 (2012).



---

## List of Figures

1.1	Schematic representation of three main non-contact dissipation mechanisms . . . . .	10
2.1	Experimental set up . . . . .	14
2.2	Forces acting on the advanced tip of the cantilever suspended in pendulum geometry. . . . .	15
2.3	Schematics for ATEC cantilever geometry . . . . .	17
2.4	A schematics of an AFM experiment . . . . .	19
2.5	Calibration of cantilever using amplitude-dependent phase noise . . . . .	20
2.6	Schematic drawing to describe the tunneling barrier . . . . .	21
2.7	Power noise spectrum density of the current signal . . . . .	22
2.8	A schematic of an STM measurements . . . . .	22
2.9	STM data on poly-crystalline Au surface with Au(111) facet . . . . .	23
2.10	TaS <sub>2</sub> surface scanned by using tapping and STM mode . . . . .	24
2.11	Schematic drawing of STM, AFM and simultaneous STM/AFM measurement modes . . . . .	25
2.12	Comparison of metallic and non-metallic tips . . . . .	27
3.1	Highly Oriented Pyrolytic Graphite . . . . .	30
3.2	Force-distance curves on HOPG . . . . .	31
3.3	Force and dissipation maps . . . . .	32
4.1	1T-TaS <sub>2</sub> crystal has van der Waals interaction between the layers (see text for details). . . . .	34
4.2	A model drawing for 1D CDW . . . . .	35
4.3	Phase diagram of 1T-TaS <sub>2</sub> . . . . .	36
4.4	STM of 1T-TaS <sub>2</sub> . . . . .	37
4.5	Damping coefficient and force-distance spectra on 1T-TaS <sub>2</sub> . . . . .	38
4.6	Force and dissipation map at 5K . . . . .	39
4.7	Force and dissipation maps at RT . . . . .	40

## List of Figures

---

4.8	Force and dissipation map at RT . . . . .	41
4.9	Power noise spectrum density of $\Delta f$ . . . . .	42
5.1	Structural and electronic properties of $\text{Bi}_2\text{Te}_3$ . . . . .	47
5.2	$z(V)$ spectroscopy and image potential states on $\text{Bi}_2\text{Te}_3$ . . . . .	48
5.3	Comparison of image potential states of the sample and the tip . . . . .	49
5.4	$z(V)$ spectroscopy with an oscillating tip . . . . .	50
5.5	Voltage-dependent dissipation spectroscopy on $\text{Bi}_2\text{Te}_3$ . . . . .	52
5.6	Energy dissipation map on $\text{Bi}_2\text{Te}_3$ plotted versus distance and tip-sample voltage. . . . .	55
5.7	Magnetic field dependent dissipation spectroscopy . . . . .	56
5.8	A model for the dissipation process . . . . .	57
6.1	STM topography of the STO surface. . . . .	61
6.2	STM topography of the STO surface. . . . .	62
6.3	Electronic characterisation of oxygen vacancies at STO surface . . . . .	63
6.4	Dissipation peak formation upon high temperature annealing of reduced STO . . . . .	64
6.5	Local and non-local bias voltage $V$ and tip-sample distance $d$ resolved dissipation maps $\Gamma(V, d)$ . . . . .	65
6.6	Pendulum AFM as a characterization tool for oxygen vacancies on STO . . . . .	67



---

## Acknowledgements

When I started my PhD study, I knew that it would be a unique experience but didn't expect it to be filled with unexpected events. I had the impression that this page would be filled with the most inspiring sentences. Now at the end of my PhD, I know that continuity is more important than the inspiration to finish the PhD work. For me, another important thing was communication. The work itself doesn't have much of a value if it doesn't appeal to a scientific community and it sure doesn't evolve only with one person. The work in this PhD thesis is no different; it is the work that we took hopefully a little bit further and in the meantime, many people have contributed to it.

I would like to start by thanking Prof. Martino Poggio, for evaluating my PhD work. I'd like to thank Prof. Richard Warburton for kindly accepting to be the chairman during my defense.

I'd like to thank Prof. Ernst Meyer for giving me the opportunity to join his group as a PhD student. It brought many more opportunities to me. Ernst, I am truly thankful to you for keeping your door open and having the time whenever I needed to talk. You have made everything easier for me when I stumbled! Even after the dystopian events that have happened in Turkey, I felt lucky being here.

I particularly want to thank Dr. Marcin Kisiel for his supervision with "The Pendulum" system and all the time he has spared for helping me. Marcin, I know it has not been easy, thanks for being patient with me.

It would be impossible for me to handle the very much necessary paperwork properly without many amazing people in the house. I thank especially Barbara Kammerman and Germaine Weaver for calmly helping me since my first arrival at Basel. Germaine, I will miss our short talks about cats.

I'd like to thank Prof. Christian Shoenenberger and his team in SNI. It wouldn't be possible for me to come to Basel without the PhD scholarship SNI provides. My special thanks to Claudia Wirth, who was always smiling when I visited her office after going to a conference. I thank to Dr. Michael Calame and Dr. Andreas Baumgartner for organizing Nano in the Snow series at such nice places on top of the Swiss mountains.

## Acknowledgements

---

It was the signature of SNI and source of motivation. Andreas, unfortunately, we have met only in the last year of my PhD. I enjoyed the long discussions we had after poster sessions.

I'd like to thank my SNI fellows, especially Deepika, Yusuke, Daniel, and Jan, who were easy to talk. Deepika it was fun teaming up with you at the events! Yusuke, thanks for introducing the Japanese culture to me. Daniel, it was nice having someone who plans to continue in science for discussing the concerns related to the future. Jan, you were a great ski instructor, thank you for teaching me the basics and bringing me up on the hill believing that I could go down. I thank Alexander Shwarb from the neighboring office on the third floor, I'll remember our physics discussions after archery training. Gülbostan, thank you for your friendship. I hope you find the place that feels like home.

In Basel, I had the chance to meet with inspirational people. I would like to thank Prof. Christoph Bruder. I had the chance to follow his lecture on superconductivity and he answered all my questions when I visited the theory floor in Basel. I also like to thank Prof. Stefan Antush for allowing me to join the cosmology seminar series and answering my questions about the basics of cosmology. I thank Prof. Christoph Gerber for his motivational talks and tips for the real world. I thank Prof. Alexis Baratoff for making the most important points clear when we were discussing what was measured in the next room. My special thanks to Prof. Erio Tosatti in Trieste, Italy. I consider myself lucky that I could discuss with him on many occasions during my PhD.

Besides that I'd like to thank all Nanolino members; I've learned a lot in this very international work environment. I had the chance to look at Turkey from afar and it took me some time understating the similarities and differences with European culture. I hope I could give you satisfying answers regarding Turkey in the meantime. The pendulum system was always a bit off topic to everyone, thank you all for staying when it was my turn to present in the group meeting.

I thank Dr. Thilo Glatzel for his support and providing me the opportunity to transfer my knowledge to younger researchers. My special thanks to Dr. Urs Gysin and Yves Pellmont. Urs, I appreciate you taking care of the pendulum system when we were away. Yves, you always fixed the microscope and made it better. The measurements in this thesis wouldn't be there without your help.

Tobias, I remember our nice trips to conferences, Nottingham wouldn't be as much fun without you. Sara, I really enjoyed sharing the suites and getting the big rooms at conferences as a result of the confusion on my name. I think we don't need a plan B at the moment. I think now that it may be a good retirement plan. Marwa, thanks for being such a nice office mate. I will miss our spontaneous tea times in the office. Wishing you and Mira all the best. Roland, you have made my days in Switzerland so much easier from day one, especially by explaining the procedures that I had no idea existed. I enjoyed our discussion on daily life in Switzerland and different cultures. Lukas, thanks for always telling me your honest opinion on anything. That made me feel welcomed here and also saved me a lot of time from unnecessary work.

I would like to thank my former colleagues than from Nanobees research group, where I entered the world of SPM. They are friends now! Umut and Cem, thank you

## **Acknowledgements**

---

for never letting me feel alone. Altug, Tunc and Berk, I am looking forward to joining your Nanobees in Europe meetings. Oguzhan, I can't thank you enough but let me try once more. Thank you for introducing me to STM and always supporting me since we have met in 2008. You are an amazing mentor, I couldn't come this far without your guidance.

Last but not least, I'd like to thank my family. Mom and brother, thanks for always believing in me and for your love.



---

## List of publications & communications

### Peer-reviewed journal publications

1. **Yildiz, D.**; Kisiel, M.; Gysin, U.; Gürlü, O. and Meyer, E. Joule meets van der Waals: Mechanical dissipation via image potential states on a topological insulator surface. *submitted* (2018).
2. Kisiel, M.; Brovko, O. O., **Yildiz, D.**; Pawlak, R.; Gysin, U; Tosatti, E. and Meyer, E. Mechanical Dissipation from Charge and Spin Transitions in Oxygen-deficient SrTiO<sub>3</sub> Surfaces. *Nature Communications* **9**, 2946 (2018). DOI: [10.1038/s41467-018-05392-1](https://doi.org/10.1038/s41467-018-05392-1)
3. **Yildiz, D.**; Gürlü, O. Apparent Corrugation Variations on Moiré Patterns on Highly Oriented Pyrolytic Graphite, *Materials Today Communications* **8**, 72-78 (2016). DOI: [10.1016/j.mtcomm.2016.06.002](https://doi.org/10.1016/j.mtcomm.2016.06.002)

### Presentations

#### Seminar talks

1. Energy Dissipation with Pendulum AFM/STM. **Yildiz, D.**; Kisiel, M. and Meyer, E. *TU Delft*, 2018-06-04, Delft, the Netherlands.
2. Energy dissipation peaks on Bi<sub>2</sub>Te<sub>3</sub> studied with pendulum AFM and STM. **Yildiz, D.**; Kisiel, M. and Meyer, E. *Osaka University*, 2017-05-24, Osaka, Japan.
3. *Image States and Energy Dissipation in Bi<sub>2</sub>Te<sub>3</sub> Surface.* **Yildiz, D.**; Kisiel, M. and Meyer, E. *University of Tokyo*, 2017-05-23, Tokyo, Japan.
4. *Non-Contact Friction with Pendulum AFM.* **Yildiz, D.**; Kisiel, M. and Meyer, E. *University of Twente*, 2017-04-07, Enschede, the Netherlands.

### Contributed talks

5. *Electrostatic Friction on  $\text{Bi}_2\text{Te}_3$  (0001)*. **Yildiz, D.**; Kisiel, M.; Gysin, U.; Gürlü O. and Meyer, E. *DPG Spring Meeting of the Condensed Matter Section (SKM) together with the EPS, 2018-03-16, Berlin, Germany.*
6. *Electrostatic Friction on  $\text{Bi}_2\text{Te}_3$  (0001)*. **Yildiz, D.**; Kisiel, M.; Gysin, U.; Gürlü O. and Meyer, E. *Nanoscience in the Snow, 2018-03-18, Mürren, Switzerland.*
7. *Electronic and frictional properties of  $\text{Bi}_2\text{Te}_3$  (0001) surface*. **Yildiz, D.**; Kisiel, M. and Meyer, E. *13th International Nanoscience and Nanotechnology Conference, 2017-10-22, Antalya, Turkey.*
8. *Image states and energy dissipation on  $\text{Bi}_2\text{Te}_3$  surface*. **Yildiz, D.**; Kisiel, M. and Meyer, E. *Trends in Nanotribology 2017, 2017-06-30, Trieste, Italy.*
9. *Image states and energy dissipation on  $\text{Bi}_2\text{Te}_3$  surface*. **Yildiz, D.**; Kisiel, M. and Meyer, E. *The 19th International Scanning Probe Microscopy Conference, 2017-05-16, Kyoto, Japan.*
10. *Van der Waals Friction on Layered Structures*. **Yildiz, D.**; Kisiel, M. and Meyer, E. *Swiss Nanoscience Institute Annual Meeting, 2016-09-16, Lenzerheide, Switzerland.*
11. *Energy Dissipation Mechanism in Layered Structures*. **Yildiz, D.**; Kisiel, M. and Meyer, E. *10th International Nanoscience Student Conference (INASCON), 2016-08-04, Istanbul, Turkey.*
12. *Energy Dissipation Mechanism on Layered Structures due to Tip Sample Interaction by Pendulum AFM*. **Yildiz, D.**; Kisiel, M. and Meyer, E. *12th Nanoscience and Nanotechnology Conference (Nanotr12), 2016-06-03, Istanbul, Turkey.*
13. *Scanning Probe Microscopy (SPM) study of moire patterns on rotated graphene layer on Highly Oriented Pyrolytic Graphite (HOPG)*. **Yildiz, D.**; Sen, S; Kisiel, M; Gülseren, O; Meyer, E. and Gürlü, O. *DPG Spring Meeting of the Condensed Matter Section, 2015-03-19, Berlin, Germany.*
14. *Morphological and Electronic Study of Moirè Patterns due to Dislocated Graphene on HOPG*. **Yildiz, D.**; Sen, S; Gülseren, O. and Gürlü, O. *DPG Spring Meeting of the Condensed Matter Section, 2013-03-15, Regensburg, Germany.*

### Posters

1. *Van der Waals dissipation measured on 1T-TaS<sub>2</sub> surface*. **Yildiz, D.**; Kisiel, M.; Gysin, U. and Meyer, E. *SNI Annual meeting 2018, 2018-09-03, Lenzerheide, Switzerland.*

2. Image states and energy dissipation on Bi<sub>2</sub>Te<sub>3</sub> (0001) surface. **Yildiz, D.**; Kisiel, M.; Gysin, U.; Gürlü, O. and Meyer, E. *SPSTM-7 and LTSPM-1 International Conference*, 2018–07–29, Nijmegen, the Netherlands.
3. Magnetic Field Dependence of Energy Dissipation on a Topological Insulator Surface Studied by Pendulum AFM. **Yildiz, D.**; Kisiel, M.; Gysin, U. and Meyer, E. *DPG Spring Meeting of the Condensed Matter Section (SKM) together with the EPS*, 2018–03–15, Berlin, Germany.
4. Energy dissipation peaks on Bi<sub>2</sub>Te<sub>3</sub> studied with pendulum AFM and STM,. **Yildiz, D.**; Kisiel, M. and Meyer, E. *SNI Annual meeting 2017*, 2017–09–07, Lenzerheide, Switzerland.
5. Electrostatic, phononic and van der Waals friction on layered materials. **Yildiz, D.**; Kisiel, M. and Meyer, E. *DPG Spring Meeting*, 2017–03–22, Berlin, Germany.
6. Electronic and van der Waals friction on layered structures. **Yildiz, D.**; Kisiel, M. and Meyer, E. *Nanoscience in the Snow*, 2017–01–26, Zermatt, Switzerland.
7. Energy Dissipation Mechanism On Layered Structures. **Yildiz, D.**; Kisiel, M. and Meyer, E. *International Non-contact Atomic Force Microscopy (NC-AFM)*, 2016–07–28, Nottingham, UK.
8. Energy Dissipation Mechanism On Layered Structures. **Yildiz, D.**; Kisiel, M. and Meyer, E. *The Second European Workshop on Understanding and Controlling Nano and Mesoscale Friction*, 2016–07–5, Riga, Latvia.
9. Energy Dissipation in Layered Structures. **Yildiz, D.**; Kisiel, M. and Meyer, E. *Swiss NanoConvention*, 2016–06–30, Basel, Switzerland.
10. Energy dissipation on layered crystals measured by pendulum AFM. **Yildiz, D.**; Kisiel, M. and Meyer, E. *International Scanning Probe Microscopy Conference (ISPM)*, 2016–06–15, Grindelwald, Switzerland.
11. Energy Dissipation on Layered Crystals Measured by Pendulum AFM. **Yildiz, D.**; Kisiel, M. and Meyer, E. *611. WE-Heraeus-Seminar: Mechanisms of Tribology*, 2016–03–30, Bad Honnef, Germany.
12. Energy Dissipation Mechanism On Layered Structures. **Yildiz, D.**; Kisiel, M. and Meyer, E. *DPG and Spring Meeting*, 2016–03–09, Regensburg, Germany.
13. Energy Dissipation on Layered Structures. **Yildiz, D.**; Kisiel, M. and Meyer, E. *DPG and Spring Meeting*, 2016–03–09, Zinal, Switzerland.
14. Energy Dissipation on Layered Structures due to Tip Sample Interaction by Pendulum AFM. **Yildiz, D.**; Kisiel, M. and Meyer, E. *Swiss Working Group for Surface and Interface Science*, 2016–01–22, Fribourg, Switzerland.

## List of publications & communications

---

15. Investigation Of Morphological And Electronic Properties Of Moiré Patterns By Scanning Probe Microscopy. **Yildiz, D.**; Kisiel, M.; Gürlü, O. and Meyer, E. *The International Conference on Understanding and Controlling Nano and Mesoscale Friction*, 2015–06–23, Istanbul, Turkey.
16. Investigation Of Morphological And Electronic Properties Of Moiré Patterns By Scanning Probe Microscopy. **Yildiz, D.**; Kisiel, M.; Gürlü, O. and Meyer, E. *Swiss NanoConvention*, 2015–05–27, Neuchâtel, Switzerland.
17. Intricacies Of Moiré Patterns At The Atomic Level: A Scanning Probe Microscopy Perspective. **Yildiz, D.**; Kisiel, M.; Gürlü, O. and Meyer, E. *Ecotrib2015*, 2015–03–4, Lugano, Switzerland.
18. Scanning Probe Microscopy Study of Swift Heavy Ion Irradiated Graphitic Surfaces. **Yildiz, D.**; Peksu, E.; Grygiel, G.; van der Beek, K. and Gürlü, O. *Condensed matter in Paris CMD-25*, 2014–08–25, Paris, France.
19. Investigation of electronic and morphological properties of graphene/HOPG system and the unexpected corrugation variation observed on moiré patterns. **Yildiz, D.**; Sen, S.; Gülseren, O. and Gürlü, O. *Condensed matter in Paris CMD-25*, 2014–08–25, Paris, France.
20. Scanning Probe Microscopy Study of Swift Heavy Ion Irradiated Graphitic Surfaces. **Yildiz, D.**; Peksu, E.; Grygiel, G.; van der Beek, K. and Gürlü, O. *NanoTR-10*, 2014–06–20, Istanbul, Turkey.
21. Electronic properties of super-periodic structures due to dislocated graphene on HOPG. **Yildiz, D.**; Sen, S.; Gülseren, O. and Gürlü, O. *29th European Conference on Surface Science (ECOSS-29)*, 2012–09–05, Edinburgh, Scotland.
22. Morphological And Electronic Properties of Moire Patterns on Graphene and Graphitic Layers On HOPG. **Yildiz, D.**; Ersoy, T. and Gürlü, O. *NanoTr-VI*, 2010–06–16, Izmir, Turkey.
23. Grafin/HOPG sisteminde Nano boyutlu Moire yapıları. **Yildiz, D.**; Erdogan, E. and Gürlü, O. *Nanoscience and Nanotechnology workshop*, 2009–02–12, Istanbul, Turkey.



---

## Curriculum Vitae

Name: Dilek Yildiz

Date of birth: 22 January 1988

Place of birth: Orhaneli, Turkey

### Education

- 2014 – 2018 PhD in Experimental Physics, University of Basel, Switzerland
- 2012 – 2014 Master in Physics, Istanbul Technical University, Turkey
- 2006 – 2012 Bachelor in Physics, Istanbul Technical University, Turkey
- 2002 – 2006 Science and Mathematics, Vefa High school, Istanbul, Turkey
- 1994 – 2002 Primary and Secondary school, Orhaneli, Bursa, Turkey

### Teaching and Outreach Activities

- 2014 – 2018 Teaching assistant for practical works:
  - “Fortgeschrittenenpraktikum – Hall Effect and Doping Measurements in Germanium Crystal”
  - “Fortgeschrittenenpraktikum – Scanning Tunneling Microscopy”

### Awards and Scholarships

- 2014 - 2018 PhD scholarship (Swiss Nanoscience Institute),

## Curriculum Vitae

---

- 2014 Graduation thesis support project (2014) (ITU),
- 2011 Best Poster Prize, Nanoscience and Nanotechnology Conference (NanoTR-7), Istanbul, Turkey
- 2010 - 2011 B.Sc. research project (TÜBİTAK BİDEB-2209 program),
- 2006 - 2012 Educational scholarship (Department of Scholarships for Higher Education),
- 2006 - 2009 Scholarship for university education (Vefa Foundation),
- 2002 - 2009 Scholarship for high school education (Vefa Foundation),